Two-dimensional Materials For Use In Advanced Energy Storage

Sivakkumaran Sukumaran

A thesis presented for the degree of
Master of Science by Research in Condensed Matter Physics

Department of Physics
University of Durham
Supervised by Dr. Michael Hunt
September 2020

Abstract

The high energy density, rapid charging and discharging and high degree of cyclability make supercapacitors a promising form of electrochemical energy storage. The storage of energy through the assembly of charge at electrode surfaces in these devices make the use of nanostructured materials particularly attractive. In this work a simple, scalable and green approach – liquid phase high shear exfoliation – is used to produce aqueous suspensions of two dimensional materials in the form of platelets a few layers (< 10) thick and with lateral dimensions of order a few hundred nanometres to a few micrometres.

Suspensions of few layer graphene (FLG) are used to produce free-standing, binder-free supercapacitor electrodes which are characterised by scanning electron microscopy (SEM), Raman spectroscopy, cyclic voltammetry (CV) and galvanostatic charging/discharging. Increasing the shear rate during exfoliation of graphene is found to produce FLG platelets with a smaller size and hence increasing number of edge defects. With increasing defect density the specific capacitance of FLG electrodes is found to increase and the effective series resistance decrease, both of which can be attributed to increased electronic doping of the FLG with increasing edge defect density.

The FLG suspensions produced in this study were characterised by Raman-spectroscopy based metrics which suffer from a lack of generality and are indirect. Hence, an initial approach towards the automated characterisation of platelets of two-dimensional materials is developed and applied to MoS_2, successfully demonstrating the feasibility and promise of direct imaging-based characterisation techniques.

Declaration

I declare that all work, including experimental, to complete this thesis was carried out at the Department of Physics, Durham University, United Kingdom and has not been submitted to fulfill another degree or qualification elsewhere. All of the research carried out to complete this thesis was done so by myself unless explicitly stated otherwise.

Acknowledgements

I want to thank my supervisor Dr. Michael R. C. Hunt for his continuous support throughout my academic year at Durham University, without his patience, guidance and the invaluable experience he has taught me I would not have been able to complete this degree.

I would also like to thank Mr Leon Bowen for his assistance with SEM.

I am also grateful for the technical support provided by the IT and Software Engineering staff in the Department of Physics.

Lastly, I would like to thank my parents and family who made this possible.

Contents

1 Introduction **1**

1.1 **Energy storage devices** 1

1.2 **Supercapacitors** 5

1.2.1 Electrical double-layer capacitors (EDLCs) 6

1.2.2 Pseudocapacitors 10

1.3 **Supercapacitor vs Batteries** 11

1.4 **2D Materials: Introduction to Graphene and MoS_2** . . 13

1.4.1 Graphene: Structure and Properties 14

1.4.2 MoS_2: Structure and Properties 16

1.5 **Synthesis of Graphene and MoS_2** 18

1.5.1 Mechanical exfoliation 19

1.5.2 Reduction of Graphene Oxide 21

1.5.3 Chemical Vapour Deposition (CVD) 21

1.5.4 Self-assembly 23

1.5.5 Liquid phase exfoliation 24

1.6 **A brief review of graphene and MoS_2 based electrodes in supercapacitors** 30

2 Experimental Techniques **34**

2.1 **UV-Vis Spectroscopy** 34

2.2 **Raman Spectroscopy** 36

2.3 **Scanning Electron Microscopy** 39

2.4 **Electrochemical Analysis** 43

2.4.1 **Cyclic Voltammetry** 45

2.4.2 **Galvanostatic Charge Discharge** 47

3 Experimental Procedure **49**

3.1 **Liquid Phase Exfoliation** 49

3.2 **UV-Vis spectrometer** 51

3.3 **Vacuum filtration of Graphene and MoS_2 samples** . . . 52

3.4 **FEI Helios Nanolab 600 DualBeam FIB/SEM** 53
3.5 **Zeiss EVO SEM** 53
3.6 **ASEQ RM1 Raman Spectrometer** 54
3.7 **Potentiostat/galvanostat** 56

4 Free-Standing Binder-Free FLG Supercapacitor Electrodes 58
4.1 Introduction 58
4.2 Characterisation of FLG Supercapacitor Electrodes 58
4.2.1 UV-vis spectroscopy 58
4.2.2 Raman Spectroscopy 60
4.2.3 SEM 65
4.2.4 Electrochemical Characterisation 66
4.3 Conclusions 76

5 Shear exfoliated few-layer MoS_2 platelets 77
5.1 Characterisation of few-layer MoS_2 platelets 77
5.1.1 Introduction 77
5.1.2 UV-Vis spectroscopy 77
5.1.3 SEM 80
5.2 Conclusions 86

6 Summary and Further work 88
6.1 Summary 88
6.2 Further work 89

List of Figures

1.1 Schematic of the structure of, and processes involved for charge storage in, an EDLC [29]. 6
1.2 Visualisation of the electric double layer theorised by the Stern-Grahame model [30]. 9
1.3 Schematic of the structure of, and processes occurring in, a pseudocapacitor [29]. 10
1.4 Schematic of the honeycomb lattice of graphene and the associated Brillouin Zone, a_1 and a_2 are lattice vectors [50]. 14
1.5 Representation of the different orientations and phases of MoS_2, with letters indicating stacking sequence [63]. 17
1.6 Schematic of the various synthesis techniques employed to produce 2D materials. Each production method has been evaluated by Raccichini et al. in terms of graphene quality (G), cost aspect (C, low value corresponds to high cost), scalability (S), purity (P) and yield (Y) [78]. 19
1.7 Mechanical exfoliation of MoS_2 [79]. 20
1.8 CVD process for graphene, where (a) is a schematic of a typical CVD system and (b) indicates grain size control through the parameters of temperature (T) and pressure (P) [83]. 22
1.9 Vapour transport growth process for MoS_2 [87]. 22
1.10 Schematic of anodic and cathodic electrochemical exfoliation mechanisms used to produce few-layer graphene [98]. 25
1.11 Schematic of the electrochemical exfoliation mechanism used to produce monolayer and few-layer MoS_2 [99] 26
1.12 Schematic of the sonication exfoliation process used to produce layers of graphene/MoS_2 [107]. 27
1.13 Illustration of the high shear mixing exfoliation to produce layers of graphene/MoS_2. Shearing occurs in the second panel and the platelets resulting from this process are shown in the third panel [110]. 28

2.1 Illustration of the different processes that occur during the interaction of electromagnetic radiation and matter [130]. . . . 35
2.2 Absorbance spectrum from a suspension containing graphene oxide and graphene [133]. 36
2.3 A typical Raman Spectrum obtained from monolayer graphene [142]. 38
2.4 Illustration of the various excitations and the associated frequency produced, whereby v_e is the frequency of the absorbed photon and v_s is the frequency of the scattered photon [143]. . 39
2.5 A schematic showing the basic structure of a Scanning Electron Microscope [145]. 41
2.6 An illustration of the interaction of an incident electron beam with a sample in the SEM [147]. 42
2.7 The 'Universal Curve' of inelastic mean free path of electrons in a solid as a function of kinetic energy [149]. 43
2.8 Schematic of a three electrode electrochemical cell configuration [151]. 44
2.9 Schematic of a two electrode electrochemical cell [152]. 45
2.10 An example of a Cyclic Voltammogram and the importance of scan rate [154]. 46
2.11 An example of a GCD curve [155]. 48

3.1 Silverson Laboratory Mixer Model L5M-A. 50
3.2 (a) The UV-Vis spectrometer used to determine concentration and number of layers of the exfoliated two-dimensional platelets of MoS_2 and graphene; (b) the cuvette housing, with the reference cell holder being furthest to the back. 51
3.3 Vacuum filtration apparatus. 52
3.4 The FEI Helios Nanolab 600 DualBeam system [158]. 53
3.5 Chamber of the FEI Helios Nanolab 600 DualBeam FIB/SEM [158]. 54
3.6 Zeiss EVO SEM. 55
3.7 The ASEQ RM1 Raman spectrometer 55
3.8 Main board of potentiostat/galvanostat, with annotations indicating the ports used to connect electrodes, USB connection to the PC and LEDs to indicate the different operation modes [159]. 56
3.9 The split terminal electrochemical test cell used for CV and GCD measurements. 57

4.1 UV-Vis spectra obtained from suspensions of FLG produced at differing shear rates. 59
4.2 Raman spectra of the graphene electrodes produced from FLG exfoliated at shear rates of 3000, 5000, 7000 and 9000 RPM. The D, G, D' and $2D$ modes are labelled. 61
4.3 Average number of graphene layers in the FLG platelets as a function of shear speed used in their production, derived from Raman spectra using the thickness metric proposed by Paton *et al.* [108]. 62
4.4 Screenshot of a typical Lorentian fit to the D, G and D' bands of a FLG electrode sample produced at a shear speed of 9000 RPM. The upper panel shows the fit, the lower the non-normalised fit residuals. 63
4.5 The ratio I_D/I_G plotted against shear speed. 64
4.6 Example SEM images of FLG electrode samples at various shear rates. The scan area is 10 μm $\times$ 10 μm in all images. . . 66
4.7 CV curves for the electrode produced from FLG shear exfoliated at 3000 RPM at 5 and 10 mV s^{-1} scan rates. 68
4.8 CV curves for the electrode produced from FLG shear exfoliated at 3000 RPM at 25 and 50 mV s^{-1} scan rates. 68
4.9 CV curves for the electrode produced from FLG shear exfoliated at 5000 RPM at 5 and 10 mV s^{-1} scan rates. 69
4.10 CV curves for the electrode produced from FLG shear exfoliated at 5000 RPM at 25 and 50 mV s^{-1} scan rates. 69
4.11 CV curves for the electrode produced from the second FLG sample shear exfoliated at 7000 RPM at 5 and 10 mV s^{-1} scan rates. 70
4.12 CV curves for the electrode produced from the second FLG sample shear exfoliated at 7000 RPM at 20 and 50 mV s^{-1} scan rates. 70
4.13 CV curves for the electrode produced from FLG shear exfoliated at 9000 RPM at 20 and 50 mV s^{-1} scan rates. 71
4.14 Variation of specific capacitance with the shear rate at which FLG electrodes were produced, measured at a sweep rate of 50 mV s^{-1}. 72
4.15 GCD curves (5th and final cycles) for a FLG electrode produced from material shear exfoliated at 5000 RPM. 73

4.16 Variation of specific capacitance with cycle number measured on the discharge half cycle of FLG electrodes produced at 5000 RPM. The cell was subjected to charging/discharging at 1 mA. The data are normalised to the specific capacitance measured at the first cycle, C^0_{sp}. 74

5.1 UV-Vis spectra of MoS_2 exfoliated at several shear speeds. . . 78
5.2 MoS_2 exciton peak wavelengths versus shear speed. 79
5.3 An example of image analysis using ImageJ. 81
5.4 Distribution of platelet areas for few-layer MoS_2 samples shear exfoliated at 3000, 4000 and 5000 RPM. 82
5.5 Distribution of platelet areas for few-layer MoS_2 samples shear exfoliated at 6000, 7000 and 8000 RPM. 82
5.6 Average platelet areas for few-layer MoS_2 as a function of shear speed. The line is a guide to the eye. 83
5.7 Circularity of MoS_2 platelets produced at shear speeds of 3000, 4000 and 5000 RPM. 84
5.8 Circularity of MoS_2 platelets produced at shear speeds of 6000, 7000 and 8000 RPM. 84
5.9 Average platelet circularity for few-layer MoS_2 as a function of shear speed. 85
5.10 Feret diameter of MoS_2 platelets produced at Shear Rates 3000, 4000 and 5000 RPM. 85
5.11 Feret diameter of MoS_2 platelets produced at Shear Rates 6000, 7000 and 8000 RPM. 86

List of Tables

1.1 Comparison of advantages and disadvantages of supercapacitors with respect to batteries [41]. 12
1.2 Comparison of performance parameters between a supercapacitor and a typical Lithium-Ion battery [42]. 13

4.1 Concentration of the FLG samples produced through shear exfoliation. 60
4.2 Measured mass of the FLG electrodes produced. Masses are accurate to ±1 mg. 67
4.3 Specific Capacitance in F g^{-1} of each electrode sample produced at various shear rates. Cyclic voltammagrams for low scan rates were not measured for the 9000 RPM sample. . . . 72
4.4 Specific Capacitance calculated from GCD of each electrode sample produced at various shear rates. 73
4.5 Coloumbic efficiency and ESR of electrode samples produced at various shear rates. 75

5.1 Concentration of MoS_2 suspensions as a function of shear speed. 79
5.2 A and B exciton peaks of the various samples produced at different shear speeds. 79

Chapter 1

Introduction

1.1 Energy storage devices

With global concerns regarding climate change and the rising need for renewable energy, research has been heavily invested into energy storage devices that not only effectively store energy but are able to transfer it to numerous electronic devices and technologies [1, 2]. The motivation behind this is that current energy storage devices, such as batteries, have a number of limitations in collecting and supplying energy to match the consumption needs of current technology. For instance, electric cars and mobile devices ideally require fast charge and discharge rates, with batteries performing poorly and degrading rapidly under such conditions [3]. These issues will have to be resolved as advances in technology are made, to ensure sustainability, reducing our environmental impact and in turn our existential crisis. One viable device that can potentially achieve high power output, fast charging and good cyclability, and in doing so supplement batteries, is the supercapacitor [4], which is the main focus of the work presented in this thesis.

There are, however, a range of energy storage technologies in existence, each having their own specific set of advantages and disadvantages, which we shall consider in turn. Flywheel energy storage (FES) [5] utilises a flywheel, a suspended wheel made of composite material, rotated at high speed by an electrical motor. The electrical energy is stored as kinetic energy and when energy is required, the flywheel is slowed down to convert this energy back into electrical energy. FES can supply instant power, such as in microgrids, they also boast a long life-span, usually 20 years with little need for maintenance, high conversion energy and power density [6]. However due to friction,

limitations to the FES are imposed such as reduced efficiency and power loss – ranging from 3% to 20% per hour [7]. Current FES technology is working towards the incorporation of either magnetic or electromagnetic bearings and in some cases a vacuum environment to circumvent these limitations. An example of this being the passive magnetic bearing flywheel engineered by NASA [8]. However, adequate infrastructure must be in place to ensure security of the device in the case of a failure, therefore the implementation of magnetic/electromagnetic bearings is still a topic of current research. FES technology can be considered to be 'environmentally friendly' as there are no greenhouse emissions or harmful chemicals involved in the application of the device. The merits of FES technology partly fulfil the aim of finding an energy storage device that is both sustainable and able to supplement batteries. However, their cost and the difficulty to scale, as a result of inherent design limitations and safety risks, means that FES can only be considered for niche applications at present.

Hydrogen fuel cells have also received significant attention for their viability as an energy storage device [9]. The fuel cell operates as a medium for the oxidation of hydrogen, producing electricity, heat and water. The hydrogen is either sourced from the electrolysis of water or reformation of hydrocarbons. For the oxidation to take place, a fuel cell is designed to incorporate an anode and cathode separated by an electrolyte membrane. Hydrogen and oxygen are supplied to the anode and cathode respectively, and to hasten the process a catalyst, situated at the anode, splits the hydrogen into the respective constituents: electrons and protons. The protons traverse through the electrolyte membrane to reach the cathode, whereas, the electron has to pass through an electric circuit to reach the cathode, producing an electric current and heat. Upon reaching the cathode, the electron, proton and oxygen combine to make water. Fuel cells can operate indefinitely, as long as a constant source of fuel is supplied, it is also a clean technology as no harmful chemicals or greenhouse gases are produced. Hydrogen fuel cells have been employed in applications ranging from electronic and automotive to grid scale fixed storage [10]. In addition, the device is scalable through stacking multiple fuel cells together to provide power from a few watts to megawatts. As such, hydrogen fuel cells offer many advantages over batteries, such as instant recharging, long lifetime and higher energy conversion efficiency [11]. The advantages are further accentuated by the abundance of hydrogen, which ensures energy security for the future. Nonetheless, there are complications to consider in the implementation of the device in a range of applications, for instance, the complexity of the device compared to batteries. The design of a conventional fuel cell needs to include fuel and oxidant delivery and water

removal systems. This effects the size of the fuel cell and may limit the potential for miniaturisation, a requirement for portable devices [11]. Alongside this, the production of hydrogen is costly, with the predominant source being from the reformation of hydrocarbons - which produces the greenhouse gas carbon dioxide as a byproduct. The majority of hydrogen currently produced is utilised for other purposes such as fertilisers and uses in the petrochemical industry [12]. Therefore, prior to the widespread utilisation of hydrogen fuel cells an adequate hydrogen infrastructure must be in place to ensure a safe distribution of sufficient fuel to meet expected global demand [13].

Superconducting magnetic energy storage (SMES) stores electrical energy through the use of magnetic fields [14]. SMES is composed of two parts: a cryogenically cooled superconducting coil and a power conditioning system. When current passes through the coil it generates a magnetic field and, due to the absence of resistive loss associated with the flow of current, the electrical energy within the coil indefinitely. The requirement for the cryogenic cooling needed for current superconducting materials means that the primary application for SMES is for grid-based applications, to provide power during critical loads and outages to assisting with load leveling [15]. A benefit of utilising SMES is that due to the mechanism of energy storage, no chemical process are involved, making the device environmentally friendly. SMES are also compact, unlike other large-scale energy storage devices, which may expand the device to other applications such as electric utilities. They also have a long-life span (20 years), therefore are a viable choice for long-term sustainable energy storage [16]. However, specialised equipment is needed to ensure the SMES operates at maximum efficiency, of which, needs careful monitoring to ensure internal and external factors – AC currents and temperature leakage respectively – do not effect the performance. Furthermore, the device produces large magnetic fields which require their own safety zones to prevent hazards. The main drawback is the difficulty of commercialisation of SMES, due to their small energy density compared with other energy storage devices [17] and great expense. In order for SMES to be competitive these issues will need to be addressed.

Pumped hydroelectric storage (PHES) is a large-scale energy storage technology that utilises a pump and turbine to generate electricity from the descent of water from an upper reservoir into a lower reservoir [18]. The water is usually transported to the upper reservoir, for storage, through pumps but connections to natural water masses can also be made. As the pump requires electricity to operate, the process of transportation is performed when demand for electricity is low (either at night or during the weekend) and the transfer of water from upper to lower reservoir occurs when the demand for

electricity is high. As the PHES relies on water passing through the turbines to generate electricity, the scale of the PHES is large which increases the overall efficiency. Therefore, PHES is commonly used for grid-storage applications to stabilise the grid during high demand, load balance and act as an energy reserve in case of grid failure [19]. PHES is also cheap compared with other grid-based devices, due to large capacity coupled with low maintenance and operation cost, and notably the reliability of the energy storage to supply during peak times. As with the other energy storage devices discussed above there are drawbacks to consider, for instance, the topography of the location for the PHES to be situated on must offer suitable elevation for the respective reservoirs. Furthermore, the construction of PHES can take years, even decades, with a considerable amount of upfront capital [20]. Yet, it is the environmental impact that is the main cause for concern. PHES requires a large reservoir to be built, which is achieved through damming rivers, this has a profound affect on the local ecology, affecting not only aquatic wildlife but creating a dry environment which alters the local ecosystem. There have also been cases where the water quality has degraded due to the increase in water temperature and the accumulation of sediment at the bottom of the reservoir [19].

Compressed air energy storage (CAES), is a technology that utilises the compression of air to store energy. The basic concept of CAES is as follows: electrical energy is stored as compressed air, the compressed air is then released through an air turbine to generate electricity when required [21]. There are three key components to the CAES system – compressor, storage container and air turbine. The compressor acts to inject air into the container. The container used is either man-made containers or existing geographical formations such as salt mines, caverns and porous rock formations, e.g. aquifers [22]. The air turbine establishes a connection between the CAES and the grid. CAES is similar to PHES outlined above, as electricity is used during periods of low demand to pressurise and store the air and then released through an air turbine during peak demand [21]. It is also second to PHES in terms of scalability, due to the volumes of pressurised air that can be stored. As such, the applications are much the same, namely grid-level storage. CAES boasts the longest time frame in energy storage as compressed air can be stored for up to a year with minimal losses [22]. Depending on the type of storage used the cost of establishing a CAES is cheaper than other energy storage devices used in grid-level applications, with man-made mines being more expensive than geological formations [22]. The main limitation of the deployment of CAES, and the commercialisation of the technology, is the reliance on geographical formations to act as storage containers. Other-

wise, constructing man-made mines and storage facilities drive up the costs considerably, especially when taking into account of round trip efficiency. Furthermore, finding suitable geographical formations is difficult and with the accompanying environmental issues, such as terrestrial acidification [23], obstructs the establishment of CAES worldwide [24].

Electrochemical energy storage (EES) devices encompass technologies in which electrical energy is either stored chemically (as in the case of batteries and pseudocapactive materials) or physically (in electrochemical double layer capacitors – EDLCs). In general such devices consist of a pair of electrodes immersed in an electrolyte and separated by a suitable porous membrane which allows the passage of ions but prevents the electrodes from shorting electrically [25]. The structure, physics and chemistry of EES systems and the detail of how they store energy will be considered in Sections 1.2 and 1.3. EES consists of a well-established suite of technologies which have the advantages of scalability from portable device to grid-level storage and can be utilised without the generation of additional pollution or greenhouse gases. However, there are a number of issues that remain to be resolved, such as the relatively limited cycle lifetime of batteries and the low power densities associated with EDLCs. The emergence of a range of nanomaterials over the past two decades has opened up new avenues for the creation of electrode materials which may ultimately address these deficiencies and the use of a relatively novel class of nanomaterials – two-dimensional solids – in EDLCs forms the focus of the work presented in this thesis.

1.2 Supercapacitors

Supercapacitors, also known as ultracapacitors or electric double-layer capacitors (EDLCs), differ from conventional electrolytic capacitors in that they have a very high capacitance but at the cost of low voltage limits [4]. Unlike batteries which store energy through electrochemical reactions involving the bulk of the electrode material, a supercapacitor utilises the interaction at the electrode-electrolyte interface involving the surface of the electrode material to store energy.

Supercapacitors have a number of distinct properties that make their use preferential to that of batteries in certain situations. For instance, they are able to maintain an extended cycle lifetime, unlike electrochemical batteries which have a defined cycle life [26]. As a result maintenance and waste can be reduced due to their larger life span. Moreover, they can provide higher power densities and instantaneous charge/discharge due to their low

equivalent series resistance [27]. Finally, the performance of a supercapacitor over wide variations in temperature is outstanding: energy can be delivered, with little loss of performance at temperatures as low as -40 °C, depending upon the electrolyte used [26]. However, due to their low voltage limits, and variation of voltage with charge state it is challenging to use them as a continuous power source. Hence, the current primary applications of supercapacitors are when energy/power is needed quickly, i.e., to fill in power gaps or where rapid charge/discharge cycles are necessary. For this reason they are used for regenerative braking in all types of automobiles, short-term energy storage or burst-mode power delivery [28]. As a result, research has been heavily focused on supercapacitors as a valuable addition to current energy storage systems. Supercapacitors can be classed into two groups, *electrical double-layer capacitors* (EDLCs) and *pseudocapacitors*. This grouping reflects differences in the mechanism by which they store charge.

1.2.1 Electrical double-layer capacitors (EDLCs)

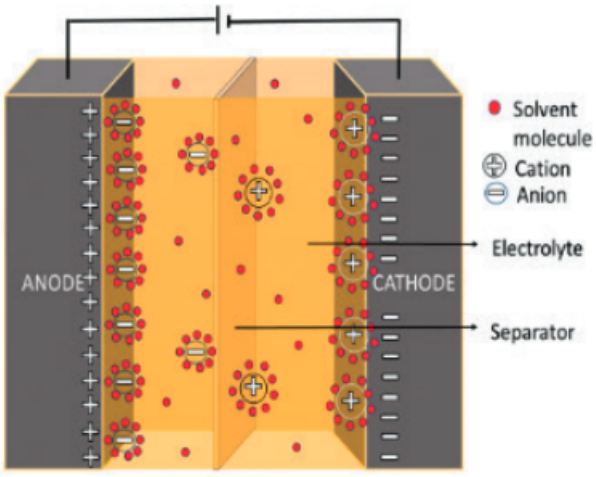

Figure 1.1: Schematic of the structure of, and processes involved for charge storage in, an EDLC [29].

A schematic of the structure of an EDLC is presented in Figure 1.1. Two electrodes are separated by an electrolyte and a porous separator, the latter to ensure that there is no short-circuit between the electrodes. Porous electrodes are typically used, as these offer a large surface area for the formation of an electrostatic double layer at electrode-electrolyte interface. The electrolyte usually consists of an equal number of positive and negative ions which have been dissolved in a suitable solvent (although ionic liquids can

also be employed). The main purpose of the electrolyte is to ionically "connect" the two electrodes and enable the storage of energy. This is achieved through the interaction between the surface of the electrode and the electrolyte over the specific area where they come into contact. When a voltage is applied across the EDLC, ions migrate to the electrode of the opposite charge to form an electric double-layer. The double layer consists of two layers of charge, one formed within the surface of the electrode and the other, with opposite polarity, created from solvated ions in the electrolyte.

There are three main theoretical treatments of the electric double layer: the Helmholtz, Gouy-Chapman and Stern (or Stern-Grahame) models [30, 31]. The Helmholtz treatment of the electric double layer is the simplest, in that the double layer is regarded as two rigid oppositely charged layers, one situated on the electrode surface and the other in the electrolyte solution, separated by a distance d. The model is regarded as an oversimplification, with one of the limitations being the assumption of a rigid layer of charge in the electrolyte. This is not observed experimentally as, due to the thermal motion of liquid molecules, a rigid layer of charge within the electrolyte cannot exist. The model also incorrectly predicts that the capacity of the electric double layer, C, is constant with cell potential. Finally, the model does not account for variations in the double layer with electrolyte concentration and temperature. Although the electric double layer found *in-situ* cannot be adequately described by the Helmholtz model it is nonetheless helpful in visualising the fundamentals of double layer formation in an EDLC.

The Gouy-Chapman model treats the double layer as one rigid layer of charge, situated on the surface of the electrode and the other, oppositely charged, layer is *diffused* in the electrolyte. The positive and negative charges are distributed throughout the electrolyte due to thermal agitation and free movement of ions, instead of forming a rigid layer. Unlike the Helmholtz model, the Gouy-Chapman model was successful in accounting for the change in properties of the double layer with respect to the change in electrolyte concentration and temperature. However, the model assumes that ions act as point charges and are close to the electrode surface, as such C is inversely proportional to d. Yet, experimental values for C are lower than expected. This discrepancy arises due to the assumption that activity is equal to molar concentration, along with ions acting as point charges, made when deriving the Boltzmann distribution. Even though the model is not entirely accurate, it has determined that the double layer is in fact a diffused double layer.

The Stern model takes the essential parts of the Helmholtz and Gouy-Chapman model and modifies them. Stern established that the first part

of the double layer, the Stern layer, is a compact layer of ions, of approximately single ion thickness, situated on the electrode surface (Helmholtz view). This meant that the remaining ions that were not confined to the electrode surface were allowed to move freely through the electrolyte. The distribution of charges are then influenced by electrostatic forces and thermal agitation, unlike the other models. This diffused layer (Guoy-Chapmann view) is referred to as the Gouy-Chapman layer. To formulate these theoretical assumptions, Stern postulated that the ions were not point charges but particles of finite size. This meant that there is a defined distance, usually a few nm, that restricts the ions from approaching the electrode. This also meant that the ions in the diffuse portion can be assumed to act as point charges as they were at a distance d from the surface, meaning that their potential and concentration were low enough to justify the statement. As a result, calculated capacities and experimental capacities are in general agreement, as the total capacity of the interface is the capacitance of the Helmholtz layer, C_{H} and the Guoy-Chapman layer, C_{G}, in series. Considering cases when electrolyte concentration is low, the double layer is essentially all diffuse therefore capacitance can be approximated to be equal to C_{G} and when concentration is high, the capacitance can be approximated to being fixed at the Helmholtz layer and therefore equal to C_{H}. The model also demonstrated the dependence of the capacitance on electrode potential and electrolyte concentration. The Stern model was further modified by Grahame to incorporate ionic species that were solvated and could penetrate the Stern layer creating three regions within the double layer [32], as shown in Figure 1.2. Therefore, as practical supercapacitors utilise electrolytes with high concentration to increase performance [33], the Stern-Grahame model can be used to theoretically treat the electric double layer.

From Figure 1.2 we can see that the Stern layer is separated into two layers called the Inner Helmholtz plane (IHP) and Outer-Helmholtz plane (OHP) [31]. The IHP is a monolayer composed of polarised solvent molecules, whereas, the OHP encompasses the solvated ions in the electrolyte solution at the distance of approach to the electrode surface. The molecules in the IHP adhere by physical adsorption on the surface of the electrode and act to separate the oppositely charged ions: one can think of them as an equivalent to a molecular dielectric. Throughout the formation of the double layer there is no transfer of charge between the electrode and electrolyte and electrostatic forces, rather than electrochemical interactions, are the source of adhesion. As a result, there are no chemical changes to the polarised molecules due to the lack of charge transfer [34]. These properties characterise EDLCs and differentiate them from other energy storage devices. During the pro-

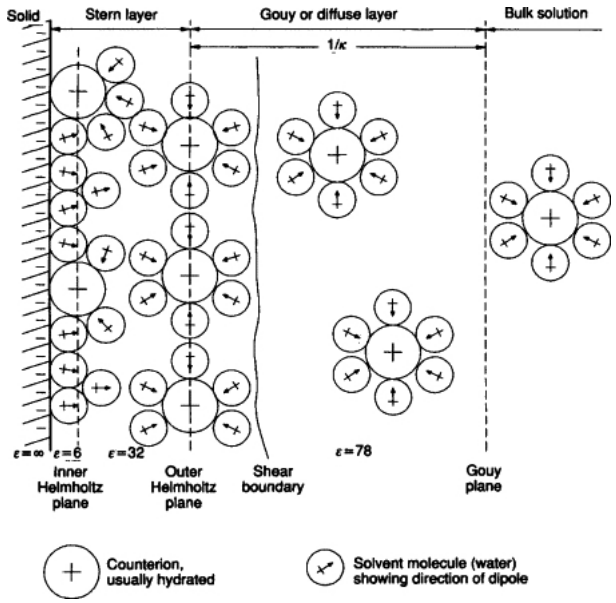

Figure 1.2: Visualisation of the electric double layer theorised by the Stern-Grahame model [30].

cess of applying a voltage across the EDLC, the amount of charge stored within the electrode is matched by the counter-charges distributed, bounded by the OHP [35]. The double-layer stores the electrical charge and forms a static electric field in the molecular layer of the solvent molecules in the IHP, the voltage drop across this field is equivalent to the magnitude of the applied voltage. One can think of the EDLC as equivalent to a conventional parallel-plate capacitor, with the main difference being that the dielectric has a thickness of a single molecule. As a result, in the simplest approximation, the standard capacitance formula for planar dielectric capacitors can be used to calculate an EDLC's capacitance [36],

$$C = \epsilon \frac{A}{d}$$

where C is capacitance, ϵ is the permittivity of the dielectric separating the electrodes, A is electrode surface area and d is the double-layer separation. From this equation, it can be seen that double-layer capacitors have a much higher capacitance value than 'traditional' capacitors due to a combination of the high surface area achieved through the choice of electrode material

used (e.g. activated carbon) and very small double-layer distance, typically of the order of a few Ångstroms (0.3-0.8 nm) [37].

Along with the high capacitance that can be achieved, EDLCs also boasts other vital characteristics that exemplify the benefits of a supercapacitor as discussed in Section 1.2, rapid charge and discharge and a potentially almost unlimited number of charge/discharge cycles. The rapid charge and discharge results from the fact that charge storage occurs at the electrode surface and hence does not require the bulk diffusive processes which occur in battery electrodes. The unlimited cyclability is due to the absence of chemical changes taking place within the electrode or electrolyte – therefore, charging and discharging the double layer can, in principle, be undertaken over an unlimited number of cycles without degradation. Some of these attributes are also shared with the other class of supercapacitors, pseudocapacitors, of which will be discussed in Section 1.2.2.

1.2.2 Pseudocapacitors

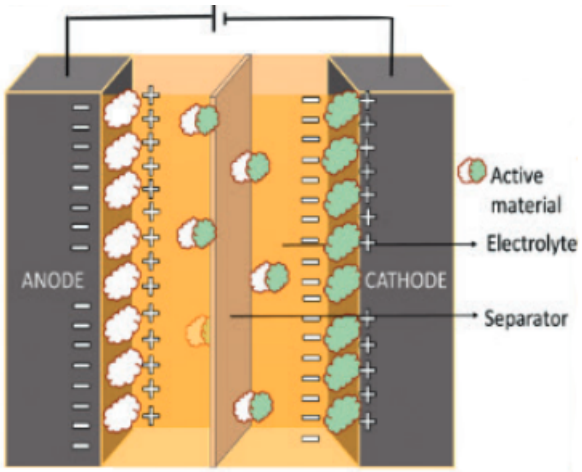

Figure 1.3: Schematic of the structure of, and processes occurring in, a pseudocapacitor [29].

Pseudocapacitors store energy electrochemically through the utilisation of Faradaic redox reactions with charge-transfer. The structure of a pseudocapacitor is similar to an EDLC in that two, often porous, electrodes are separated by an electrolyte, Figure 1.3. When a voltage is applied to the pseudocapacitor, the electrodes become oppositely charged: this initially attracts polarised ions in the electrolyte to the oppositely charged electrode and a double layer is formed, as in an EDLC. The layers comprise polarized ions

which are situated on the electrode surface. The layer is separated by the electrolyte molecules resulting in an electric field, leading to the formation of a double-layer capacitance. As ions diffuse through the layer, the atoms residing on the electrode surface adsorb the ions, allowing the transfer of electrons. The continuous flow of electrons, from one electrode to the other, passes through the generated double-layer and produces Faradaic current. This process is called a redox reaction, whereby charge is transferred via reduction-oxidation and hence differentiates pseudocapacitors from EDLCs. Pseudocapactors may be *extrinsic* or *intrinsic*. Intrinsic pseduocapacitive behaviour does not vary with crystalline properties, particle size or morphologies. Examples of electrode materials that exhibit this type of behaviour are RuO_2 and MnO_2 [38]. Extrinsic pseudocapacitive behaviour involves redox reactions which occur primarily at the surface of the material and does not involve diffusion into the bulk. Hence, such behaviour depends on particle size and is present in electrode materials that are nanostructured to increase their surface area, such as $LiCoO_2$. By increasing the surface area diffusion distance is decreased and a pseudocapacitve behaviour is established [39]. The primary features of a pseudocapacitor, rapid charge and discharge rates and high capacitance, is observed whether the behaviour is intrinsic or extrinsic [39]. The Faradaic process involved in charge storage within pseudocapacitors allows them to achieve higher specific capacitance and energy densities compared to EDLCs. However, they can also suffer from a lack of long-term stability during charge and discharge cycles, much like in batteries, due to degradation of the electrodes with cycling (originating, for example, due to expansion/contraction of the pseudocapacitive material during Faradaic reactions [34, 40]).

1.3 Supercapacitor vs Batteries

Given that supercapacitors are closest to batteries in terms of operation, structure and packaging, it is instructive to make a comparison between these two forms of energy storage device, which is presented in Table 1.1. We can see that the main advantage of supercapacitors over batteries is that in essence they have an unlimited cycle life and high power density. This is further illustrated in Table 1.2 in which the performance of a typical supercapacitor is compared with that of a current generation lithium-ion battery.

There are some significant drawbacks with current generations of supercapacitor which prevent them from supplanting batteries. These include low

Energy Storage Device	*Advantages*	*Disadvantages*
Supercapacitor	Unlimited cyclability Fast charge/discharge High power density No degradation of storage capability Broader effective operating temperature Environmentally-friendly	Low energy density Expensive to produce Not viable for long-term energy storage Gradual voltage loss
Batteries (e.g. Lithium-ion)	Large storage capacity High energy density Long term energy storage solution, low self-discharge rate	Poor cyclability Susceptible to degradation (poor retention of energy over time) Low power density Poor recyclability

Table 1.1: Comparison of advantages and disadvantages of supercapacitors with respect to batteries [41].

energy densities, high self-discharge (indicating poor long-term energy storage) and, most importantly, the production cost or cost per Watt [42]. As a result of these issues, many current approaches to the application of supercapacitors are directed towards supplementing batteries to overcome the performance limitations of the latter (e.g. poor charge/discharge cycling making the device unsuitable for applications in electric vehicles [EVs] or mobile phones). Supercapacitors can be utilised in applications where frequent charge/discharge cycles or extreme operating temperatures might be expected. For example, in public transportation supercapacitors can be used in electric powertrains to offer rapid charging during regenerative braking and deliver high current on acceleration. Batteries and supercapacitors can be used in conjunction in such an application, with the supercapacitor employed when quick discharge is needed for short-term power needs and the battery utilised to provide energy over a longer timescale when the vehicle

Performance Parameter	*Supercapacitor*	*Lithium-Ion Battery*
Charge time	1-10 seconds	600 seconds
Cycle life	1 million	500
Specific energy (Wh kg^{-1})	3-10	250
Self-discharge (%)	60	4

Table 1.2: Comparison of performance parameters between a supercapacitor and a typical Lithium-Ion battery [42].

has reached its cruising speed. The benefit of this combination is that battery stress is reduced, which consequentially improves battery life and eliminates the need for the cost and weight penalties associated with battery oversizing, which is currently the usual approach to address these problems.

To create an effective supercapacitor, materials of high quality have to be used which, along with the associated production methods, drive up costs. Furthermore, as supercapacitor performance is largely dependent on electrode structure and properties – notably surface area – electrode materials have to be engineered appropriately. Ideally, materials should be produced and assembled into electrode structures in a cost-effective manner. The scalable production of high quality nanomaterials (few-layer platelets of two-dimensional solids) and evaluation of their assembly into binder-free electrodes in a single step process is the main goal of the work presented in this thesis.

1.4 2D Materials: Introduction to Graphene and MoS_2

Both EDLCs and pseudocapacitors rely heavily on the interaction between electrochemically active ions and the electrode surface. Due to their inherent structure, 2D materials exhibit high surface area (indeed, an ideal freestanding two-dimensional solid is *all* surface), a key requirement for maximising the charge storage within a supercapacitor. In addition to this, they are often highly electrically conductive [43] which reduces internal resistances within the supercapacitor and can improve power density: during high current draw, significant voltage can be dropped across the supercapacitor if internal resistance is high, dissipating electrical energy as heat. Following the discovery of graphene [44], a large number of 2D materials have been identified [45]. In this thesis the two materials examined are those which have proved the

most promising both in terms of physical properties and cost – (few layer) graphene and MoS_2.

1.4.1 Graphene: Structure and Properties

Graphene, often regarded by academics as a 'wonder material', was first isolated in 2004 by André Geim and Konstantin Novoselov [44] having previously been thought to be unstable. It has numerous desirable properties, making the material promising for a wide range of applications ranging from field-effect transistors [46] and transparent electrodes [47] to body armour [48]. These properties include: a thermal conductivity in the order of 5000 W $m^{-1}K^{-1}$, electron mobility of up to 250,000 cm^2 V^{-1} s^{-1} at room temperature, very high specific surface area (2630 m^2 g^{-1}), a high modulus of elasticity (∼1 TPa), (much higher than many pure metals) and good electrical conductivity [49].

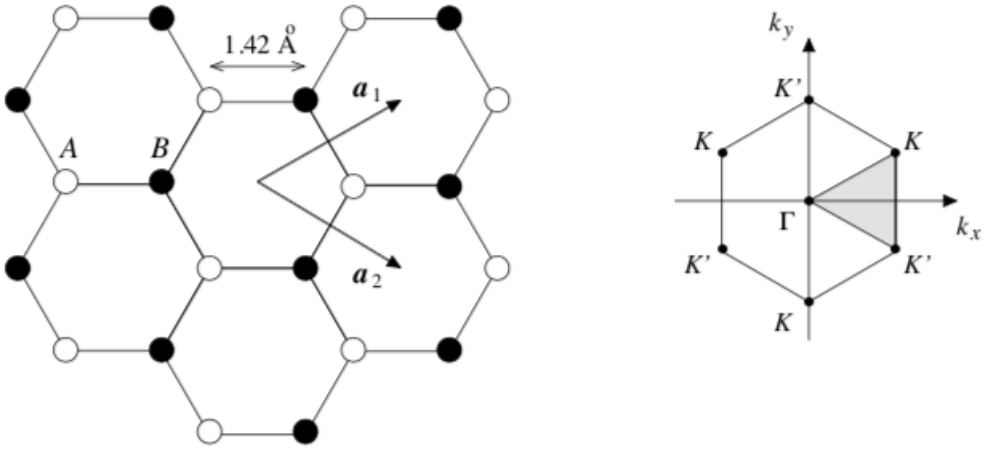

Figure 1.4: Schematic of the honeycomb lattice of graphene and the associated Brillouin Zone, a_1 and a_2 are lattice vectors [50].

Graphene consists of a single layer of carbon atoms, arranged in an open hexagonal structure and, from this inherent structure, the various extraordinary properties of graphene arise. A unit mesh (unit cell in two-dimensions) of graphene contains two carbon atoms with unit-cell vectors, a_1 and a_2, and a lattice constant of 2.46 Å. As a result of sp^2 hybridisation, delocalised π bonds are present (which originate from the single unhybridised p orbital perpendicular to the planar structure), along with the in-plane σ bonds, which result from the overlap of the hybridised orbitals. These 'double bonds' result in a short interatomic separation within the graphene structure (∼1.42 Å),

they are stronger than the sp^3 hybrid bonds found in diamond, thus giving monolayer graphene the highly desirable mechanical properties discussed above [51].

The electronic band structure of graphene can be calculated through the use of the tight-binding model. This model demonstrates the essential features of the graphene dispersion relation - the variation of electron energy wave vector k over the Brillouin Zone (BZ) [52, 53],

$$E = \pm t\sqrt{1 + 4\cos^2\frac{\sqrt{3}k_y a}{2} + 4\cos\frac{3k_x a}{2}\cos\frac{k_y a\sqrt{3a}}{2}} \tag{1.1}$$

where t is the value of the nearest neighbour hopping matrix element and a is the lattice constant. If we consider values of k for which E becomes zero, it follows that such values must satisfy the conditions,

$$\frac{3k_x a}{2} = (2n+1)\pi\ ,\ \cos\frac{\sqrt{3}k_y a}{2} = +\frac{1}{2} \qquad (n\ integral.) \tag{1.2}$$

The first condition takes k_y outside the first BZ, however the second is satisfied at the corner points of the BZ labelled K and $K^{'}$. These points are known as the 'Dirac Points'. The significance of this feature is that the energy band is symmetric about $E = 0$ at these two points. Calculations demonstrate that the density of states at the Fermi level is zero at these points [52, 53]. This is also the case when spin is taken into consideration, graphene exhibits one electron per spin per atom allowing only two electrons per unit cell, hence the band is half-filled. The half-filled band and zero density of electronic states at the Fermi level are the attributes of a semimetal or zero band gap semiconductor.

Although monolayer graphene was the primary focus of early studies, bilayer graphene (BLG), which consists of two graphene layers and few layer graphene (FLG), which consists of 3-10 graphene layers [54] have also demonstrated attractive properties with significant potential for application. For example, so-called 'twisted' bilayer graphene, in which the second layer is oriented at a small azimuthal angle to the first, has a flat band with a high density of states at the Fermi level, leading to superconductivity at 1.7 K, a relatively high temperature given the nature of the material, which indicates a very strong electron pairing strength [55]. In FLG the bandgap is tunable, unlike graphene, which is due to the overlap between the valence and conduction band. When an external electric field is applied the band gap

can be changed electrostatically for the desired application [56]. Therefore, FLG offers versatility in applications. Furthermore, there are key benefits to the utilisation of FLG as electrode material for supercapacitors, such as the large lateral flake size [57]. The material also offers a reduction in resistance and smaller diffusion channels [58] which greatly enhances the performance of such energy storage devices.

As a result of the potential offered by graphene, due to the properties discussed above, numerous methods for production of monolayer graphene, BLG and FLG sheets have been established [59]. With the latter being of importance to this study, as the scalable production method chosen to produce the materials used in this thesis, high shear exfoliation (discussed in Section 1.5.5), the primary material produced is FLG with a negligible contribution from monolayer material.

However, if graphene is to be utilised for energy storage devices there is the requirement that large-scale production must be commercially viable and the quality of the material must be maintained to an appropriate standard, furthermore it is highly desirable that the graphene sheets are prevented from restacking [60]. The various graphene synthesis techniques are discussed in Section 1.5.

1.4.2 MoS_2: Structure and Properties

In one of the first papers discussing the isolation of graphene Geim and Novoselov also examined other two-dimensional materials with a similar structure [61]. After the initial focus on graphene the academic research community recognised that it is possible to isolate a whole 'family' of two dimensional materials with a range of unique properties not shared by their bulk analogues. Some of these materials were found to be able to address a number of disadvantages of graphene for specific applications, such as the lack of a band gap which makes graphene undesirable for digital electronics [62] and it's chemical inertness which, although beneficial for some applications, means that desirable reactions such as pseudocapactive charge storage is not possible. Among the family of 2D materials those that have received the most attention, due to the abundance and relatively low cost of precursors and/or parent bulk solids, are the transition metal dichalcogenides (TMDCs), a group of layered materials which have the general chemical formula MX_2, where M is a transition metal and X = S, Se and Te. The most notable TMDC in terms of volume of previous research is MoS_2 (Molybdenum disulphide), the reason for the popularity of this material will be outlined below.

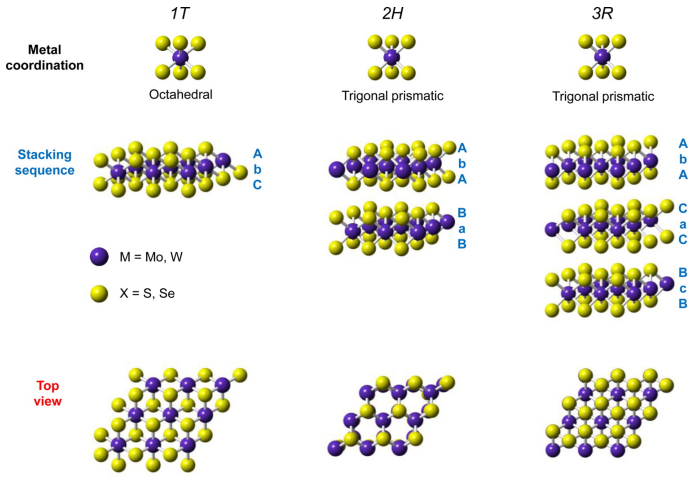

Figure 1.5: Representation of the different orientations and phases of MoS_2, with letters indicating stacking sequence [63].

The basic building block of MoS_2 consists of a layered structure in which a plane of molybdenum atoms is sandwiched by planes of sulphide ions as shown in Figure 1.5. This principal structure forms what is generally termed a monolayer of MoS_2. The thickness of each monolayer has been determined to be ∼0.65 nm [64]. To obtain bulk MoS_2, multiple monolayers are stacked upon each other and held together by weak van der Waals forces. The properties, and hence potential applications, of MoS_2 change with its structure. Bulk MoS_2 in the $2H$-phase, where H represents hexagonal symmetry [65, 66], behaves as an indirect-band gap semiconductor with a band gap of 1.2 eV and monolayer $2H$-MoS_2 exhibits a direct band gap of 1.9 eV, with the band gap increasing as a function of the decrease in the number of layers [67]. As such, the dependence of electronic properties on the number of layers, as indicated by the change in energy of the band gap with respect to the number of layers, has highlighted the extraordinary potential to utilise MoS_2 in various applications e.g. optoelectronics, hydrogen evolution reaction and as an electrode material for energy storage devices such as lithium-ion batteries [68–70].

There are three distinct phases of MoS_2, originating from the local symmetry of the monolayers and stacking sequence: $1T$, $2H$ and $3R$ [67], Figure 1.5. When labelling the phases of MoS_2, the numeral indicates the number of layers and the accompanying letter is associated with the crystallographic structure, T being trigonal, H Hexagonal and R Rhombohedral. The stacking sequence affects the electronic structure of MoS_2 and primarily the stability of the configuration [67]. The $1T$ phase of MoS_2 is metallic while the

thermodynamically stable $2H$ phase is semiconducting and a semi-conductor to conductor transformation can be achieved through intercalation of the $2H$ phase with alkali metals [71, 72]. Due to the thermodynamic stability of $2H$-MoS_2 and relative ease of production by the same high shear exfoliation methods used for graphene, the work presented in this thesis concentrates on this phase, and the term 'MoS_2' can be taken as referring to the $2H$ phase unless explicitly mentioned otherwise.

Much like graphene, MoS_2 is mechanically flexible and has a Young's modulus of 0.33 ± 0.07 TPa. $2H$-MoS_2 [64] has a lattice constant of 3.15 Å, and is stable up to 1200°C [67]. As stated above, $2H$-MoS_2 is semiconducting and is typically n-type, with a charge carrier mobility of 100 $cm^2\ V^{-1}\ s^{-1}$ [67]. Current applications of MoS_2 include: field-effect transistors, photodetectors, solar cell materials, chemical sensors and, most notably, supercapacitor electrodes [73, 74]. One of the main advantages of using MoS_2 over graphene in supercapacitor electrodes, is the fact that MoS_2 possesses a band gap where as graphene does not. This property offers flexible conductivity and the ability to 'shape' electrical currents, through the creation of a depletion region, giving the distinct property of switch control that graphene does not possess. However, the main limitations in using MoS_2 are its low power, energy density and electrical conductivity [75, 76].

An important aim of this thesis is to examine the material produced through shear exfoliation of bulk MoS_2, with its future use in energy storage devices in mind. As discussed above for the case of graphene the method of synthesis chosen – shear exfoliation – is limited in producing monolayer MoS_2 but is efficient in producing few-layer MoS_2 platelets. There are advantages in utilising few-layer MoS_2, as not only does it encompass the desired properties outlined above but also paves way for hybrid nanostructures to be engineered. For instance, graphene and MoS_2 heterostructures have been produced to broaden the applications of graphene, especially for electronic and energy storage devices where switch control is needed [77].

1.5 Synthesis of Graphene and MoS_2

A wide variety of techniques have been developed for the production of monolayer to few-layer graphene and MoS_2. These can be broadly separated into 'Top-down' techniques, in which one starts with a bulk analogue material and reduces it to monolayer or few-layer thickness and 'Bottom-up' approaches which 'build' the materials from a variety of precursors. Top-down techniques include exfoliation from the bulk by ultrasonication, mechanical shearing and

electrochemical processes and can be employed to produce high quality monolayer and particularly few-layer samples of 2D materials. Among the most notable, and potentially scalable, of the 'Bottom up' approaches to the synthesis of 2D materials is chemical vapour deposition (CVD). Each technique has both advantages and disadvantages, which are discussed in more detail below and summarized in Figure 1.6.

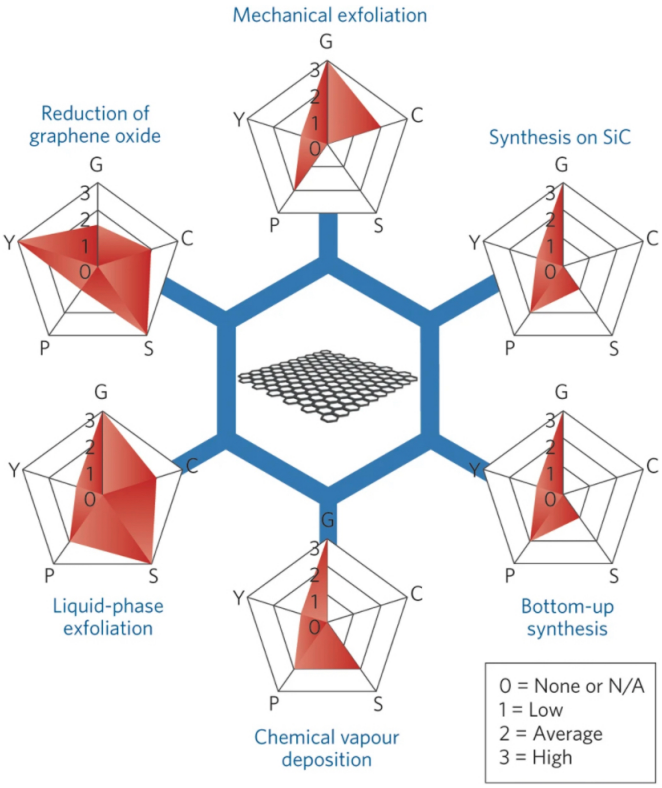

Figure 1.6: Schematic of the various synthesis techniques employed to produce 2D materials. Each production method has been evaluated by Raccichini et al. in terms of graphene quality (G), cost aspect (C, low value corresponds to high cost), scalability (S), purity (P) and yield (Y) [78].

1.5.1 Mechanical exfoliation

Mechanical exfoliation was the first technique used to isolate 2D materials [44]. As the name suggests, the technique utilises a mechanical approach, using adhesive tape (Scotch 'Magic' tape, in particular) to peel flakes off a layered material such as graphene or MoS_2 from the bulk crystal. This method is illustrated in Figure 1.7. The mechanical exfoliation step is repeated until several flakes with few, or even single, layers are present on the

tape. The flakes are then transferred onto a suitable substrate, e.g. a Si wafer, by rubbing the Scotch tape against the substrate through the use of tools, such as plastic tweezers. The number of layers on the substrate varies substantially and is determined through different characterisation methods such as Raman spectroscopy, atomic force microscopy and scanning tunnelling microscopy. Typically, the yield of monolayer and few layer material is low.

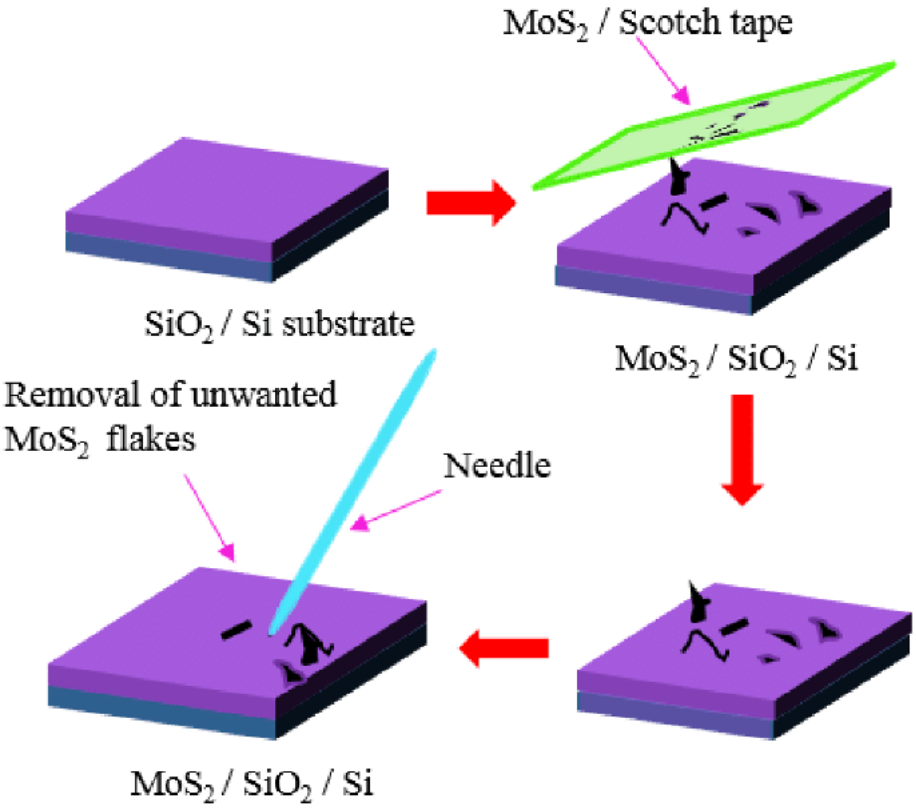

Figure 1.7: Mechanical exfoliation of MoS_2 [79].

This method produces highest quality material, with almost no defects. Moreover, the difficulty of this approach is low with minimal equipment required. However, it is rather laborious and the yield is extremely low, with a very small probability of finding a single or few-layer flake. As a result, this method is useful for small scale experiments, however, it is not possible to scale-up the process for many applications, particularly for the quantities required to produce even a single supercapacitor electrode.

1.5.2 Reduction of Graphene Oxide

The reduction of graphene oxide (GO) was one of the first potentially scalable routes for the production of graphene. The initial step in this process involves the production of graphite oxide by strongly oxidising pristine graphite. The resulting oxidised graphite has a layered structure, similar to that of the parent graphite, but oxygen atoms are introduced to the planar structure resulting in a distribution of oxidized and non-oxidized areas [80]. This functionalisation expands the interlayer spacing and makes the material hydrophillic, allowing GO to be exfoliated from the oxidised graphite in water through ultrasonication.

Once individual sheets of GO have been exfoliated the the π-electron network can be restored through reduction, increasing carrier mobility and carrier concentration [81]. This is achieved through various methods including: thermal reduction, e.g. thermal annealing; chemical reduction; and photocatalyst reduction through the use of photo-chemical reaction with a catalyst, e.g. TiO_2 [81]. Alongside the high yield that can be obtained the relative cost of the technique can be low, depending on the reduction method and associated chemical agent used, with chemical reduction being the cheapest. However, due to the chemical processing involved, defects, both intrinsic and extrinsic, are introduced into the final product, such as lattice defects and oxygen containing groups [78]. These defects impact on the materials electronic properties and hence the resulting 'graphene' is usually referred to as 'reduced graphene oxide' (rGO) to reflect its non-ideal nature. Nonetheless, reduction of graphene oxide, alongside liquid phase exfoliation, remains popular for producing graphene in substantial quantities.

1.5.3 Chemical Vapour Deposition (CVD)

CVD has become one of the most widespread techniques for the production of 2D materials, as it produces monolayer and few-layer samples with high structural quality which can then be used in many different applications. There are a number of different CVD methods, including plasma-enhanced CVD, thermal CVD and hot/cold wall CVD [82]. Although there are differences in their details the principal mechanism is the same, with the two-dimensional material being grown on a substrate through the use of one or more precursors typically in the form of a vapour or gas.

In the case of graphene, the CVD process involves the use of a hydrocarbon source, e.g. CH_4, which is then catalytically decomposed on a substrate that

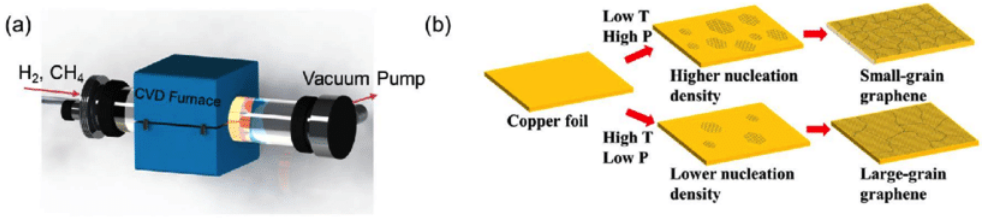

Figure 1.8: CVD process for graphene, where (a) is a schematic of a typical CVD system and (b) indicates grain size control through the parameters of temperature (T) and pressure (P) [83].

has been heated to temperatures as high as 1200°C [84], as shown in Figure 1.8. The substrates used are commonly transition metals such as nickel (Ni), platinum (Pt) and copper (Cu), with Cu being the most favoured. Cu is generally preferred as the carbon solubility is low in this metal – carbon from the decomposition of the precursor is localised to the surface and the growth process terminates when the substrate is fully covered by a graphene layer, this process is referred to as the 'self-limited surface deposition' growth mechanism [85]. When other transition metals are used graphene is formed by precipitation of carbon from the bulk [86], which is much harder to control.

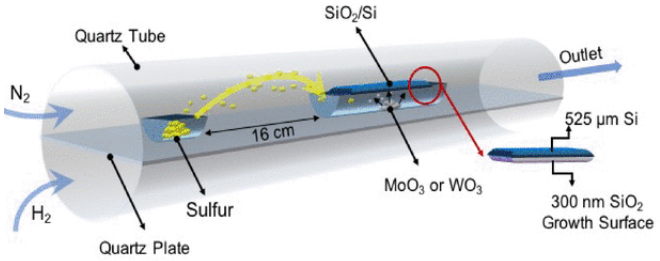

Figure 1.9: Vapour transport growth process for MoS_2 [87].

MoS_2 and other TMDCs can also be produced on a large area by vapour transport methods, which are related to CVD, as shown in Figure 1.9, in this case MoO_3 or $MoCl_5$ precursors are used. The MoO_3/$MoCl_5$ powder is vaporised, and sulphur vapour is produced by heating sulphur powder which is then carried by an inert gas flow (sometimes with the addition of H_2 to prevent oxidation) to react with the vaporised powder. This reaction produces MoS_2 which is then deposited onto a suitable substrate, e.g. SiO_2/Si. An alternative approach is to use Mo metal and S powder as precursors – the process is similar with the difference being that thin films of Mo are deposited onto a substrate, either through evaporation or sputtering and are

then exposed to sulphur vapour at high temperatures (T > 800 °C), forming very thin MoS_2 layers.

The large-area monolayer and few-layer films of 2D materials produced by CVD are of high quality. Moreover, in addition to 'conventional' precursors there is opportunity to use different feedstock materials such as food and waste [88]. However, with this particular technique there are difficulties to consider, which arise due to the complexity of the CVD process. There are numerous parameters that affect the final product, such as growth temperature, chamber pressure, precursor amount, flow rate and location and pre-treatment of substrate [89]. As such, these parameters have to be manipulated in order to yield the best material possible, minimise defects and provide an adequate growth rate. Another issue that adds to the complexity of using material produced by this approach is the frequent need to transfer the as-grown material from the growth substrate to a substrate of interest [90]. In the case of graphene transfer is complicated by chemical inertness and is known to introduce a range of defects, particularly wrinkles, into the transferred material. CVD and related methods are, moreover, expensive and also consume a large amount of energy creating a potentially significant environmental impact. However, despite these drawbacks CVD remains a popular production approach within the 2D materials field and is a viable candidate for upscaling, at least in high-value applications such as microelectronics, where materials quality is paramount [82, 91, 92].

1.5.4 Self-assembly

Self-assembly is an alternative approach to synthesising graphene/MoS_2, which uses atomic/molecular building blocks to produce said materials. The respective building blocks must have coupling sites that can be stimulated through external means, such as physical force or structure directing agents [76, 93], in order to construct structural units. The process is conducted at high temperatures, once the structural variants have been produced they are separated in order to produce the desired structure. The advantage of this technique is the atomically precise control which yields outstanding quality of graphene/MoS_2 [94]. The consequence of the precise control is the constraint in both handling and transferring the structures. Furthermore, this method is difficult to upscale as there are significant restrictions on large-scale uniformity and order [95].

1.5.5 Liquid phase exfoliation

As the name might suggest, all liquid phase exfoliation (LPE) approaches involve the exfoliation of a layered 'parent' material into monolayer or few-layer platelets (with a variety of lateral size distributions, depending upon the chosen method) suspended in a liquid, often (but incorrectly) termed the 'solvent'. The liquid may be chosen to match the surface energy of graphene/MoS_2 (e.g. N-methyl-2-pyrrolidone) or can include a suitable surfactant designed to stabilise the suspension and prevent re-stacking of the exfoliated material back into a bulk precipitate [96]. This removes the need for the use of strong oxidising or reducing agents which might create unwanted defects or functional groups on the exfoliated layers. The key difference between the various LPE approaches is the method which is employed to exfoliate the single or few layer platelets from the bulk.

Electrochemical exfoliation

Electrochemical exfoliation produces few layer graphene/MoS_2 through the use of a liquid solution (electrolyte) and an electrical potential, either anodic or cathodic, which is then applied to consume an electrode composed of graphite/MoS_2.

For graphene production, Figure 1.10, either an anodic or cathodic potential can be applied to an electrolyte solution, e.g. propylene carbonate, which drives the ionic species to intercalate into the graphite electrode and increase the inter-layer distance, subsequently exfoliating layers of graphene. In the case of an anodic potential, the intercalation of anions is utilised to increase the inter-layer distance. The positive current extracts electrons from the graphite anode, creating a layer of positive charge. This charge drives the intercalation of negative ions, e.g. sulphate anions, which increases the spacing between graphene sheets through, for example, the sulphate ions forming bubbles of SO_2 gas within the graphite electrode. As the bubbles expand exfoliation of few layer graphene sheets from the electrode occurs. On the other hand, for the cathodic potential a negative charge on the graphite electrode attracts positively charged ions from the electrolyte, e.g. Li^+, for intercalation. Much like in the process for anodic potentials, the inter-layer distance is increased between the graphene sheets which can then be exfoliated. Depending on the application, either cathodic or anodic exfoliation can be used, with cathodic exfoliation being more favourable in producing high-quality few layer graphene [97]. Anodic exfoliation yields several layers of graphene of which resemble the oxidation state of graphene oxide, however is more efficient [98].

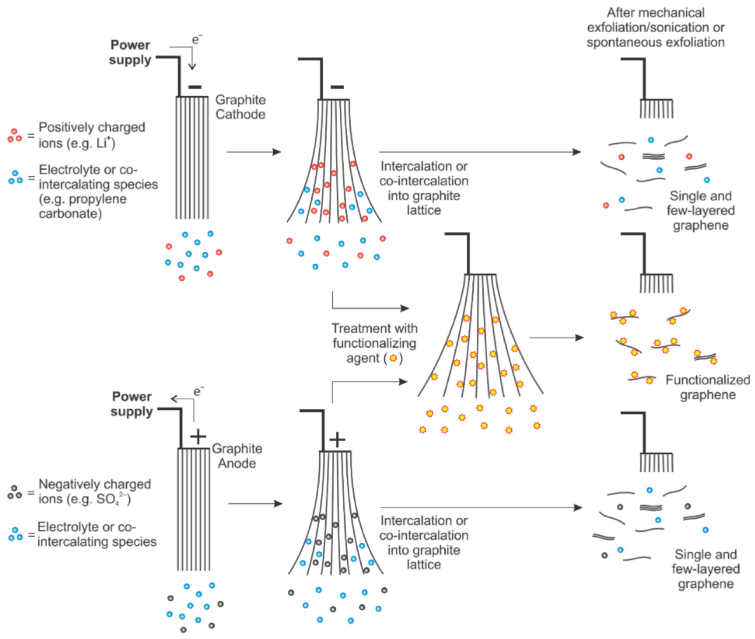

Figure 1.10: Schematic of anodic and cathodic electrochemical exfoliation mechanisms used to produce few-layer graphene [98].

For MoS_2, the process is similar to the one used to produce graphene: a MoS_2 crystal is used as the electrode and either an anodic or cathodic potential is applied to the electrolyte solution. For the case of anodic exfoliation, as shown in 1.11, the anions intercalate into the MoS_2 crystal and weaken the van der Waals interaction between the individual layers. The anions are then oxidised which releases gas, which further increases the inter-layer distance between the layers. Thus, MoS_2 flakes are then exfoliated from the crystal.

Much like other methods, electrochemical exfoliation produces low-defect few-layer graphene/MoS_2, the method is rapid and simple and is one of the more promising approaches for mass production. In addition, the total period of electrochemical exfoliation lasts over minutes/hours whilst other methods can take much longer, when considering time taken for preparation and quality control of the final product. Yet, key factors need to be considered in producing the best yield possible, the most important of which is the graphite/MoS_2 source and conditions of the intercalation-exfoliation process. For example, through intercalation with non-oxidative salts it is possible to produce flakes with lateral sizes greater than 30 μm with a thickness of 2-3 layers [100, 101]. Furthermore, the electrolyte and aqueous surfactants ensures that the process is eco-friendly, avoiding the use of dangerous and toxic chemicals. However the electrolytes used in certain cases, depending

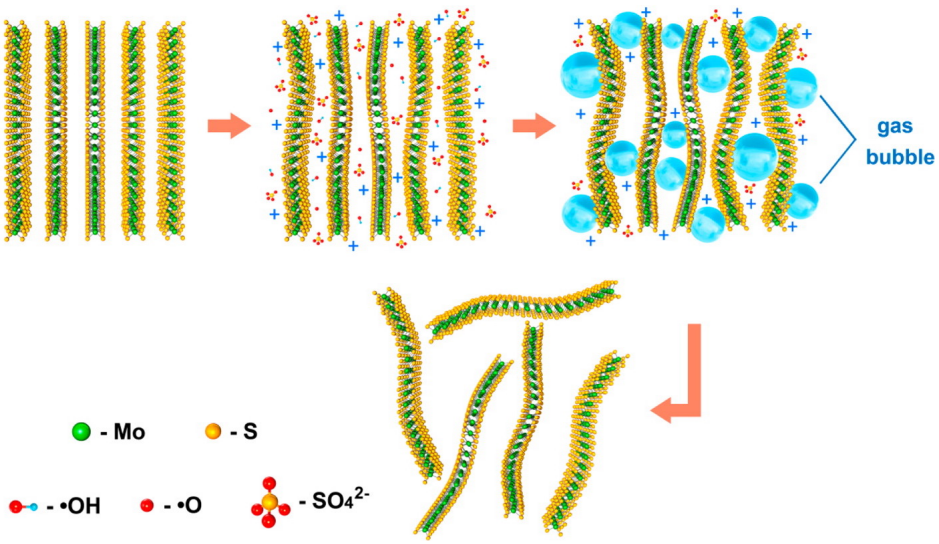

Figure 1.11: Schematic of the electrochemical exfoliation mechanism used to produce monolayer and few-layer MoS_2 [99]

on the acidity, concentration and source, can be expensive and the resulting structural changes, either through oxidisation or other forms of defects, can impact the uses of the materials in potential applications [102, 103].

Sonication

Exfoliation into a suitable liquid can also be achieved by the use of ultrasound (usually termed 'sonication') [104]. Applying ultrasound to a mixture of liquid and bulk layered material results in a cycle of high and low pressure caused by the traveling sound waves in the medium. This causes small bubbles to form during the low pressure phase. As more energy is supplied and the limit of energy absorption is reached they collapse, during the high pressure phase. This process is called 'acoustic cavitation' [105]. Repeated acoustic cavitation damages the bulk material, along with the shock waves produced by sonication, and causes fragmentation. As the material fragments, inter-particle collision further damages the bulk material. Thus, the material begins to exfoliate and, depending on the strength of the cavitation used, results in high yields of few-layer graphene/MoS_2 with varying densities of defects [106].

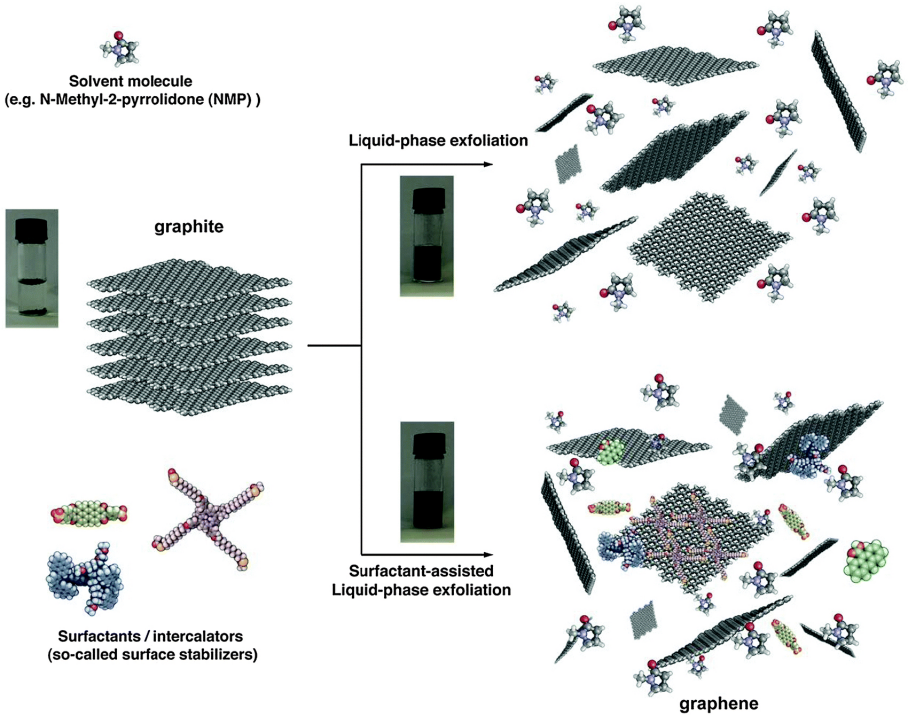

Figure 1.12: Schematic of the sonication exfoliation process used to produce layers of graphene/MoS_2 [107].

High Shear Exfoliation

High shear exfoliation utilises shear forces along with other fluid dynamic events to break down a parent layered material into monolayer and few layer platelets, a schematic of which is shown in 1.13. Bulk graphene/MoS_2 is mixed into liquid medium (in some cases including a surfactant). High shear forces are applied to this mixture through a variety of methods, with the most common method being the use of a rotating blade, which is the approach utilised in this study and discussed in greater detail in Section 3.1. The rotating blade is surrounded by a perforated housing, often called a stator. As the blade rotates, the high rotation rate causes centrifugal forces to draw in the suspension towards the bottom of the rotor which is then forced through the perforations of the stator. As the suspension passes through the stator the high-velocity gradient found in the space between the rotor and stator resulting from the high rotation rate and small rotor-stator separation exerts shear force exfoliating the parent material in the suspension. The suspension containing part-exfoliated material can re-enter the body of the mixer through the perforations and a cyclical process continually exfoliates

the material. Alongside shear force, fluid dynamic events resulting from the rapidly spinning blade, such as turbulence and collisions, further assists with the exfoliation of bulk graphene/MoS_2.

The critical shear rate for exfoliated graphene has been determined to be $\sim 10^4$ s^{-1} [108], this can be achieved through such instruments as conventional kitchen blenders, and for MoS_2 the critical shear rate is ~ 3 x 10^4 s^{-1} [109].

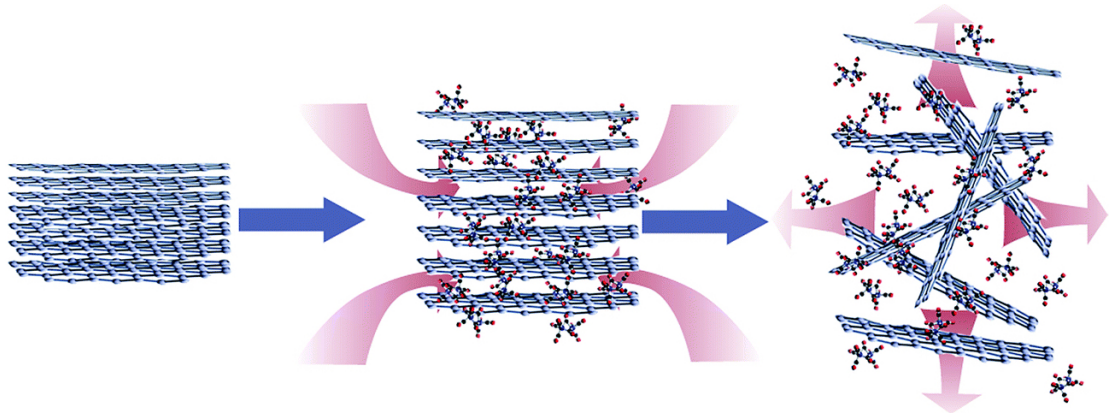

Figure 1.13: Illustration of the high shear mixing exfoliation to produce layers of graphene/MoS_2. Shearing occurs in the second panel and the platelets resulting from this process are shown in the third panel [110].

Separation/Purification

After the material has undergone exfoliation, thick, poorly exfoliated material is removed through centrifugation. The process varies among studies reported in the literature, but sediment centrifugation is most common [111]. This technique involves transferring the high shear mixed material to a container which is then spun at very high speed creating an effective acceleration of many thousands of times that of gravity, g. Thicker (and hence heavier) flakes form a sediment at the base of the tube, leaving few-layer sheets of graphene/MoS_2 in suspension.

All the LPE methods discussed above are viable in producing high quality, low defect density few-layer graphene/MoS_2 [109, 112]. These methods have the advantages of simplicity, versatility and scalability. There are, however, various parameters that need to be optimised in each method.

Sonication/shear mixing time is an important factor, usually with greater processing time equating to thinner platelets of smaller lateral size and higher concentrations [113]. However, longer processing times increase the density

of defects in the exfoliated platelets, through such mechanisms as increased collision between the suspended particles which can damage structural integrity. In addition, increasing the duration of the exfoliation process affects the overall efficiency of the method and increases energy consumption, which is not environmentally friendly. Along with sonication/shear mixing time, the ultrasound frequency/shear speed is a factor that affects the quality and quantity of material produced, as higher frequencies/speed results in thinner layers. In the case of sonication, it introduces increased energy into the suspension resulting in defects extending from the edge to the basal plane of the exfoliated material [114]. In contrast, shear exfoliation only introduces further edge defects [108]. It is also necessary to consider the liquid/surfactant used to stabilise the bulk material whilst it undergoes exfoliation, as a poor choice can lead to re-stacking of the sheets whereas appropriate liquids/surfactants stabilise the exfoliated sheets through balancing surface tension [115]. Even then, some of these liquids/surfactants exhibit high boiling point, such as N-cyclohexyl-2-pyrrolidone, creating difficulty in removing them from exfoliated material. Furthermore, due to the poor solubility of graphene/MoS_2 careful consideration must be given in deciding which liquid phase is used, as this can affect the overall quality of the subsequent layers produced.

All LPE methods suffer from the relatively low yield of monolayer graphene/MoS_2 [113] produced, although it is possible to re-use unexfoliated material to reduce this [108]. Likewise, careful consideration of the details of the centrifugation process is required in order to ensure that scale-up of these methods is viable. Given that different applications will have specific requirements regarding the platelet size and thickness of the few-layer two-dimensional material used, such optimisation is likely to be matched to final use.

Comparing the various methods for the production of few-layer graphene or MoS_2, LPE and, in particular, high shear exfoliation offers the best balance of scalability, relatively low cost and high materials quality for the production of supercapacitor materials and therefore has been chosen for the research presented in this thesis.

1.6 A brief review of graphene and MoS_2 based electrodes in supercapacitors

As discussed above, the high surface area of two-dimensional materials make them potentially very attractive for use in supercapacitor electrodes. The chemical inertness of graphene, its high conductivity, outstanding mechanical properties and its similarity to the high surface area carbons often used in EDLCs prompted a number of studies into the use of this material, the majority employing rGO or a similar chemically modified graphene material as the active element [116, 117]. In principle, as a result of the very high specific surface area of graphene, a theoretical specific capacitance of 550 F g^{-1} should be achievable [118].

Graphene can be incorporated into electrode materials in a variety of forms ranging in dimensionality: free-standing particles or dots, one-dimensional fibres, two-dimensional films and three-dimensional foams or composites [118]. As the work reported in this thesis relates to two dimensional materials, previous results related to this material form will be discussed in the remainder of this section.

There have been a number of studies undertaken of the specific capacitances (capacitance per unit mass) of supercapacitor electrodes derived from exfoliated monolayer and few layer graphenes. One of the first studies of the use of 'graphene' in supercapacitors was by Stoller and co workers [116] who found specific capacitances as high as 135 F g^{-1} with rGO based electrodes (which they termed 'chemically modified graphene') in an aqueous electrolyte, corresponding to an areal capacity of 19 μF cm^{-2} [119]. The 'chemically modified graphene' was found to contain oxygen and nitrogen with C/O and C/N ratios of 11.5 and 23.0, respectively. No information on the cycling stability of the electrodes was provided.

Si and Samulski [120] functionalised rGO with p-phenyl-SO_3 groups during the reduction process to retain the stability of the rGO dispersion used to prepare electrodes. When dried the resulting material was found to have a specific surface area of 44 m^2 g^{-1} and a specific capacitance of 14 F g^{-1}. Incorporating Pt nanoparticles to reduce the re-stacking of the exfoliated rGO increased the surface area to 862 m^2 g^{-1} and increased the reported specific capacitance to 269 F g^{-1}, although it is unclear whether this calculation included the clear redox peaks in the cyclic voltammagram, originating from the Pt nanoparticles, and hence it is difficult to draw definitive conclusions about the impact of the increased surface area.

An alternate approach to prevent re-stacking of rGO platelets was formulated by Yang and co-workers [121] through the simple procedure of ensuring that their rGO films remained hydrated. They found that hydrated rGO (which they termed 'solvated graphene' and the rGO 'chemically converted graphene') had a specific capacitance of 215 F g^{-1} in 1M H_2SO_4 which declined slowly with increasing current density. Dried rGO films were found to have a specific capacitance of ∼150 F g^{-1}, which rapidly dropped as the current density was raised. The difference in specific capacitance was ascribed to an increased surface area in the hydrated material, although by its nature no surface area measurement could be obtained. It does, however, appear that the effective series resistance in the hydrated films was lower than that observed for the dry rGO and this may explain some of the difference observed.

To avoid the incorporation of extensive oxygen containing groups Biswas and Drzal [122] used 'graphene nanosheets' produced by exfoliation of graphite through acid intercalation and thermal treatment. The resulting nanosheets were found to have an average lateral dimension of 15 μm and a thickness of 3 to 5 nm, corresponding to 9 - 15 monolayers. Hence, this material should not strictly be referred to as 'graphene' or FLG, since beyond 10 layers thick the material is electrically indistinguishable from bulk graphite [123]. These thin *graphite platelets* were deposited in layer-by-layer fashion on a solid substrate and could, in principle, be removed to produce a free-standing foil, although electrochemical measurements were performed on 20 μm thick films deposited on stainless steel plates. The specific capacitance of the films was found to be $\sim$ 36 F g^{-1} at a current of 30 A g^{-1}. The effect of defects was investigated by milling the graphite platelets, which were assembled in a sandwich structure, leading to electrodes with a specific capacitance of 80 F g^{-1} at a discharge current of 10 A g^{-1}.

A key point to note when considering the values of specific capacitance discussed above is the importance of defects in determining the capacitance of electrodes derived from graphene. The capacity of the interface between a single layer of pristine graphene and an electrolyte can be given by

$$\frac{1}{C_{electrode}} = \frac{1}{C_Q} + \frac{1}{C_H} + \frac{1}{C_{diff}} \tag{1.3}$$

where C_Q is the intrinsic (or quantum) capacitance of a single graphene layer, C_H is the capacitance of the Helmholtz layer and C_{diff} is the capacitance of the diffuse layer. In a concentrated electrolyte C_{diff} is much larger than the other terms in equation 1.3 and can be neglected [119]. The Helmholtz layer capacitance depends on the electrolyte and is found to be 28 μF cm^{-2} for 4M

H_2SO_4 [119] and 21 μF cm^{-2} for the ionic liquid 1-butyl-3-methylimidazolium hexafluorophosphate [124]. At electrode biases close to the charge neutrality point (when the Fermi level of graphene is located at the Dirac point) the number of charge carriers in graphene is expected to be zero, resulting in a quantum capacitance which is also zero. As a bias is applied to the graphene moving it away from the charge neutrality point, C_Q is expected to vary linearly with the applied voltage. Hence we would expect a strongly bias dependent capacitance, which is not observed in bulk graphene-based electrodes [116, 120, 121].

Xia et al. [124] found that even in a single layer of graphene the expected close to zero value of quantum capacitance is not observed. Instead a finite minimum value is observed. This non-ideal behaviour can be explained in terms of the presence of defects or impurities either within, or local to, the graphene layer which introduce an extrinsic carrier density, n^*. C_Q can then be expressed as:

$$C_Q = \frac{2e^2}{\hbar v_F \sqrt{\pi}} \left(|n_G| + |n^*|\right)^{1/2} \tag{1.4}$$

where n^* is the carrier density due to defects, n_G is the carrier density due to the bias applied with respect to the charge neutrality point and v_F is the Fermi velocity of graphene ($\approx c/300$).

To explore the effect of lattice disorder and functionalisation in more detail Pope and Aksay [125] reduced GO under a range of different conditions to create rGO with varying degrees of oxidation and lattice defects. A four-fold variation in double layer capacitance was observed for monolayer electrodes produced from these materials dependant on the concentration of both types of defect – the presence of functional groups or lattice defects alone was found not to be sufficient to produce such a large change. Similar behaviour was observed in 'thick film' electrodes produced from Teflon-bound material pressed onto Aluminium mesh, however it was found that the electrode with lower specific capacitance exhibited better rate performance. This result was interpreted as indicating that the increased capacitance due to defects and functionalisation comes at the cost of reduced electrode conductivity.

The dependence on capacitance on defect density is key to graphene-based supercapacitor electrode performance and is examined in this thesis by varying few-layer graphene platelet linear dimensions (and hence the density of edge defects) through varying the production (high shear exfoliation) conditions. Through limiting defects to the edges of the graphene platelets their impact on electrical conductivity, and hence rate performance, can in principle be reduced.

MoS_2 has received less attention than graphene as a supercapacitor material. Chen et al, [126] investigated the quantum capacitance of both $1T$ and $2H$ allotropes and found that C_Q of the metastable $1T$ phase was 14.9 μF cm^{-2} compared with 1.35 μF cm^{-2} for the $2H$ phase. This study also demonstrated that the MoS_2 layers re-stacked in such a way that significant ion intercalation could occur, leading to an increase in capacity with the number of layers. Such behaviour was not observed in graphene. The increase in capacity with the number of MoS_2 layers suggests that the creation of a composite electrode, consisting of MoS_2 and graphene could have a significantly larger accessible surface area than graphene alone.

Although specific capacitances of 400 to 700 F g^{-1} have been reported for bulk electrodes produced from $1T$-MoS_2 [127], this allotrope of MoS_2 is metastable and difficult to produce, hence interest remains in the performance of electrodes incorporating the $2H$ phase: Huang et al. [128] found that a layered $2H$-MoS_2 graphene composite which assembles into a three-dimensional spherical architecture exhibited a specific capacitance of 243 F g^{-1} at a discharge density of 1 A g^{-1} despite the lower capacity of this phase. In comparison, in study of spherical MoS_2 nanostructures a lower specific capacitance, 122 F g^{-1} was observed. The performance suggested by layered MoS_2-graphene electrode structure suggests that production of MoS_2-graphene composites is an attractive route for the production of high-performance supercapacitor electrodes derived from layered materials and the shear exfoliation of $2H$-MoS_2 is characterised in this thesis as a first step towards the creation of such a composite electrode.

Chapter 2

Experimental Techniques

2.1 UV-Vis Spectroscopy

UV-Vis spectroscopy is a technique that probes the electronic properties of a sample through absorption of radiation in the visible (vis) and ultraviolet (UV) regions of the electromagnetic spectrum. In addition to probing the optically-allowed transitions of gases, liquids and solids, it can be employed to determine the concentration of a specific species in a solution or suspension if its optical absorption behaviour is known [129].

Figure 2.1 indicates the various processes that are involved during the interaction between various wavelengths of electromagnetic radiation and a material (which could be gas, liquid or solid). For the purpose of this thesis, we are only concerned with absorption as a result of electronic excitation to characterise suspensions of few-layer graphene/MoS_2 produced through shear exfoliation. In brief, in these processes the energy from incident electromagnetic radiation can be absorbed by a medium when the excitation process satisfies the dipole selection rule. In the UV-vis energy range, if the energy of the incoming photons of UV or visible light is sufficient, they will cause dipole-allowed transitions between different electronic energy levels [131] of the species contained in the material in question, (if the photon energy range were much lower, in the infrared, the excitations of concern would be dipole-active vibrations of the molecule or solid).

The ratio between the intensity of light transmitted by a sample, I, to the incident intensity, I_0, is given by the Beer-Lambert Law:

$$\frac{I}{I_0} = \exp\left(-\alpha L\right) \tag{2.1}$$

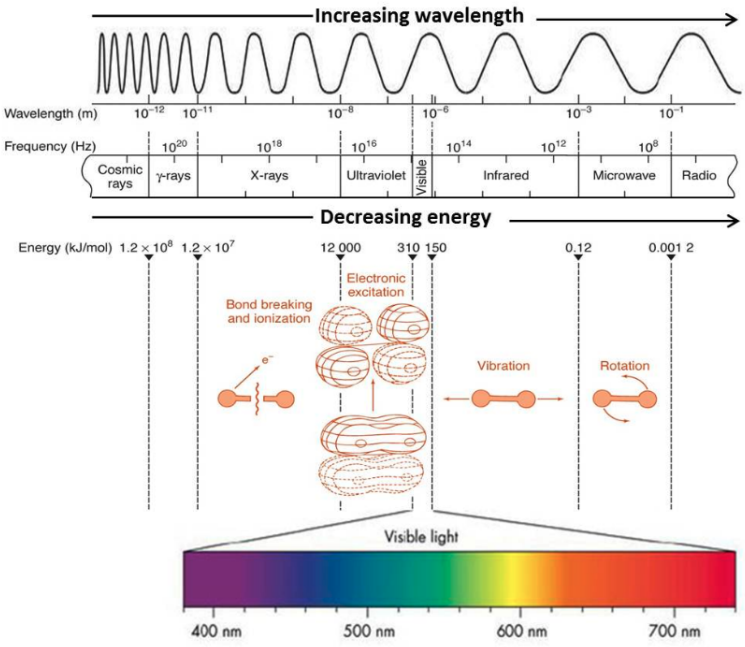

Figure 2.1: Illustration of the different processes that occur during the interaction of electromagnetic radiation and matter [130].

where L is the path length of the light through the sample and α is the *absorption coefficient*. It is often more convenient to express the results of an absorption experiment in terms of the *absorbance*, A, of a sample [132] (sometimes known as the optical density) which is defined as follows:

$$A = -\log T = -\log\left(\frac{I}{I_0}\right) = 0.434\alpha L \tag{2.2}$$

Absorbance is a convenient quantity to use when characterising solutions and suspensions due to the linear relationship between absorbance and both concentration and path length. An absorption spectrum can be constructed by plotting absorbance (A) as a function of wavelength (λ) as shown in Figure 2.2 for a suspension containing a mixture of graphene oxide and graphene [133]. The absorption peaks labelled enable the identification of graphene oxide (peak at 237 nm) and graphene (273 nm) in the suspension. The 312 nm and 361 nm peaks are associated to the conjugated polyenes CH_3-$(CH\text{-}CH)_n$-CH_3 for n = 4 and ≥ 6 respectively.

The main application of UV-vis spectroscopy within this study is to identify

whether the material of interest is present within a suspension and, if so, to determine its concentration. Concentration can be found from by rearranging equation 2.2 as follows,

$$A = \epsilon c L \tag{2.3}$$

Where A is measured absorbance at a given wavelength, ϵ is the (known) absorbtivity at that wavelength, L is the path length of the electromagnetic radiation within the sample and c is the concentration of the species of interest.

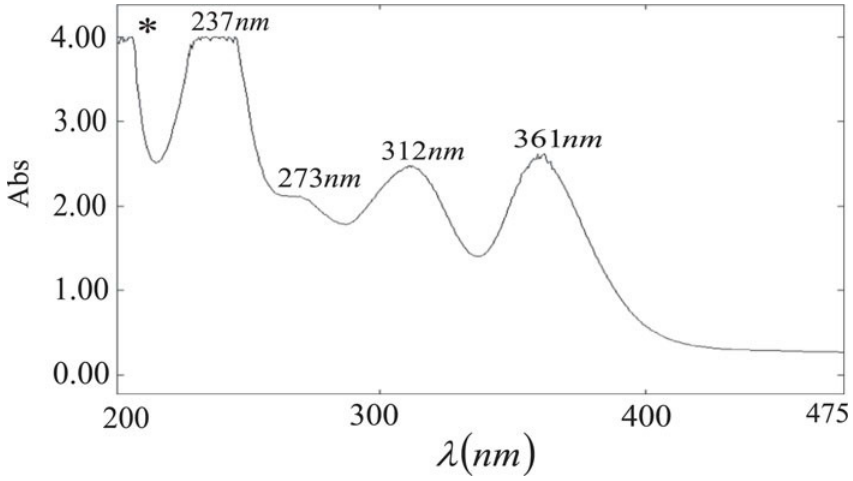

Figure 2.2: Absorbance spectrum from a suspension containing graphene oxide and graphene [133].

UV-Vis spectroscopy not only allows one to assess whether the required material is present in suspension and to determine its concentration but can also provide other additional characterisation, such as the (average) number of layers of a suspension containing few-layer two-dimensional platelets from the known shift of absorption bands with thickness [134].

2.2 Raman Spectroscopy

Raman scattering was first theorised by Smekal in 1923 and subsequently demonstrated experimentally in 1928 by C. V. Raman [135]. This process involves the scattering of incident electromagnetic radiation resulting from interaction with a time-varying polarisability induced within the sample. In

a classical picture we can consider a sample with a time-varying local polarisabiity, α given by,

$$\alpha = \alpha_0 + \Delta\alpha \cos(\Omega t) \tag{2.4}$$

where α_0 is the static polarisability and $\Delta\alpha \cos(\Omega t)$ is a time varying component oscillating at (angular) frequency Ω (originating from a molecular vibration or a phonon in a crystalline solid). When a time varying electromagnetic field $\vec{E}\cos(\omega t)$ is applied to the sample, its local polarisation varies as

$$\begin{aligned}\vec{p} &= (\alpha_0 + \Delta\alpha \cos(\Omega t))\, \vec{E}\cos(\omega t) \\ &= \alpha_0 \vec{E}\cos(\omega t) + \frac{\Delta\alpha}{2}\vec{E}\left(\cos((\omega - \Omega)\, t) + \cos((\omega + \Omega)\, t)\right).\end{aligned} \tag{2.5}$$

The time-varying local dipole moment $\vec{p}$ leads to re-radiation of electromagnetic radiation (scattering): the first term is associated with elastic (or *Rayleigh*) scattering while the second term consists of the absorption or emission of a quantum of vibrational energy by the scattered photon. In the latter case the scattered photon will have energy $\hbar\Omega$ greater (anti-Stokes scattering) or less (Stokes scattering) than its incident energy, respectively. As it is more likely that the sample is in the ground state, due to the Boltzmann distribution of phonons at thermal equilibrium, the intensity of the Stokes transition is significantly stronger than that of the anti-Strokes transition [136, 137]. By measuring the energy (the frequency or equivalently the wavelength) of the scattered photons it is then possible to determine the Raman-allowed vibrational excitations of the sample. It is this analysis of scattered radiation that forms the basis of Raman spectroscopy.

Since the development of the laser, which can provide a high intensity, highly collimated source of monochromatic light, so overcoming the low efficiency of Raman scattering (only one photon in 10^7 is typically scattered in non-resonant processes) the technique has become a staple in determining the properties of a variety of materials as it is rapid, non-destructive and non-invasive [138, 139]. Moreover, in many cases little sample preparation is required and measurements can be made under a range of conditions of temperature and pressure. In a typical Raman spectroscopy experiment monochromatic, collimated light is directed at the sample of interest and the resulting scattered light is collected either in transmission or reflection and used to plot the excitation of the sample in terms of the *Raman shift*,

$$\Delta\nu = \left(\frac{1}{\lambda_i} - \frac{1}{\lambda_f}\right) \tag{2.6}$$

where $\Delta\nu$ is the Raman shift (typically expressed in units of cm^{-1}), λ_i is the incident wavelength and λ_f the wavelength of the scattered light.

The Raman shift is used rather than the absolute wavelength of the scattered light so that the same excitation will (in the absence of dispersion) have the same energy irrespective of the energy of the incident light. A typical Raman spectrum from a monolayer of graphene is presented in Figure 4.2, two characteristic peaks of defect-free graphene, known as the G and the $2D$ bands, are clearly visible. The presence, position and width of the various Raman active bands can provide useful information on the number of layers, strain, doping and defects of a 2D material [140, 141].

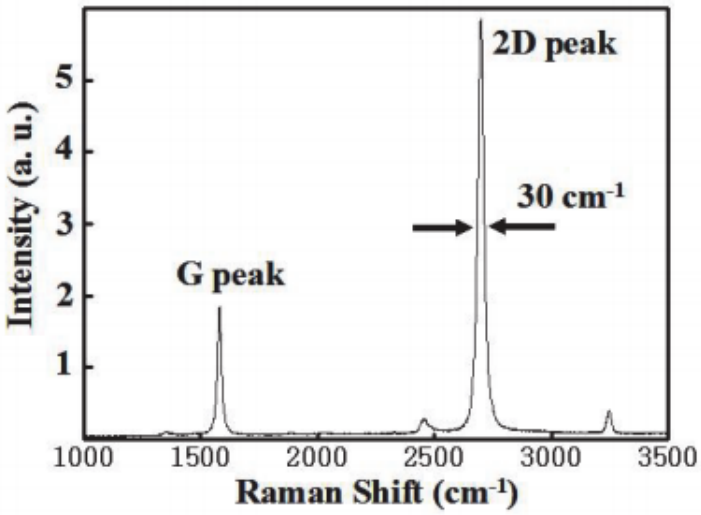

Figure 2.3: A typical Raman Spectrum obtained from monolayer graphene [142].

A more complete description of Raman scattering is provided by a quantum mechanical treatment. In general terms, the process can be considered to involve the absorption and emission of a photon, with a finite probability that the sample is left in a vibrationally (de-)excited final state. Although this picture is simplistic – the process is single-step and coherent – it enables us to understand the differences between resonant and non-resonant processes. Figure 2.4 illustrates the various frequencies produced via non-resonant Raman scattering. Absorption of a photon promotes the system into a 'virtual state', which can be thought of in terms of promoting an electron to a state which is sufficiently short-lived that the fact that its energy is not a solution of the Schrödinger equation does not preclude the excitation as, due to the Heisenberg principle, the uncertainty in its energy is so large. The short-lived nature of this virtual state explains why the probability for Stokes or anti-Stokes scattering is so small in Raman scattering. In a resonant

process, the excitation is to a real excited state of the molecule and hence such a transition can be long-lived, significantly increasing the probability of Stokes/anti-Stokes scattering and therefore substantially increasing the Raman signal. One of the reasons that Raman scattering is such a powerful tool for investigating graphene is that the unique band structure of graphene results in resonant Raman scattering for a number of vibrations over a wide photon energy range.

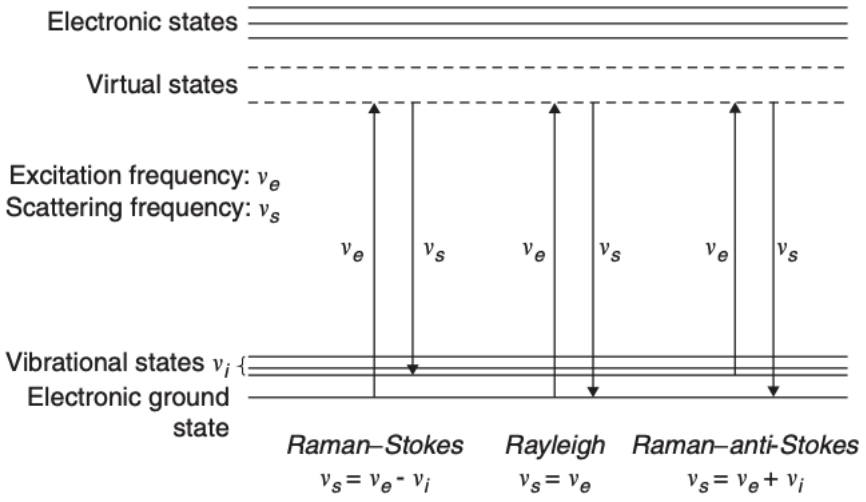

Figure 2.4: Illustration of the various excitations and the associated frequency produced, whereby v_e is the frequency of the absorbed photon and v_s is the frequency of the scattered photon [143].

2.3 Scanning Electron Microscopy

Scanning Electron Microscopy (SEM) is an advanced tool used to provide information on the topography, composition, grain orientation, and crystal structure of a sample. A schematic of a typical SEM instrument is shown in Figure 2.5. In a SEM experiment the sample to be characterised is probed by a beam of highly energetic electrons focused onto a spot on the surface of the sample (typically of the order of 1 nm in diameter). This spot is then scanned across the surface in a raster pattern and a variety of signals, discussed below, are used to build up an image of the surface.

To create the electron beam, electrons are emitted from an electron gun containing an appropriate source, either thermionically from a tungsten filament

or by tunnelling from a field emission source. The latter is generally favoured in modern microscopes since it produces a smaller energy spread in the electron beam (around 0.3 eV compared with 1-2 eV for a thermionic source) which is important for minimising chromatic aberrations, has a longer lifetime and a higher beam current. An anode is used to accelerate the electrons towards the column which contains a series of electromagnetic lenses which focus the beam. Two principal types of lens are used in the column: condenser and objective lenses. Two or more condenser lenses and an aperture define the electron beam size by converging the beam of electrons (before the electron beam cone opens). As the electrons travel towards the sample they are then met by the objective lens(es) which demagnify the beam and focus it onto the sample. The optical column must be under high vacuum, to avoid attenuation of the beam by collision with residual gases and is maintained at a typical pressure of 10^{-8} mbar [144]. Once the beam has been focused, deflection (or scanning) coils are used to create a magnetic field to continuously vary the deflection of the beam allowing a rectangular area of the sample to be scanned.

The power of the SEM as an imaging technique originates from the small wavelength of the electron beam (typically accelerated through a potential of 1 - 30 keV) which is provided by the de Broglie relation [146],

$$\lambda = \frac{h}{p} = \frac{h}{m_0 v} = \frac{h}{\sqrt{2m_0 eU}} \frac{1}{\sqrt{1 + \frac{eU}{2m_0 c^2}}} \tag{2.7}$$

Where λ is the electron wavelength, h is the Planck constant, m_0 is the rest mass of an electron, e the electron charge, U is the electric potential through which the electrons are accelerated and c the speed of light.

When the electron beam impinges upon the sample a number of interactions are possible leading to signals which can be used to characterise and image the sample. These signals include Auger electrons, secondary electrons (SE), backscattered electrons (BSE), X-rays and cathodoluminescence. As shown in Figure 2.6, in addition to providing information on differing aspects of the sample, the signals have differing penetration depth and spatial resolution. The research presented in this thesis relies on the SE and BSE signals for sample characterisation and in consequence only the mechanism by which these two signals are produced will be discussed in detail.

Secondary electrons are produced by inelastic electron-sample interactions, in which the beam interacts with the atoms in the sample, transferring en-

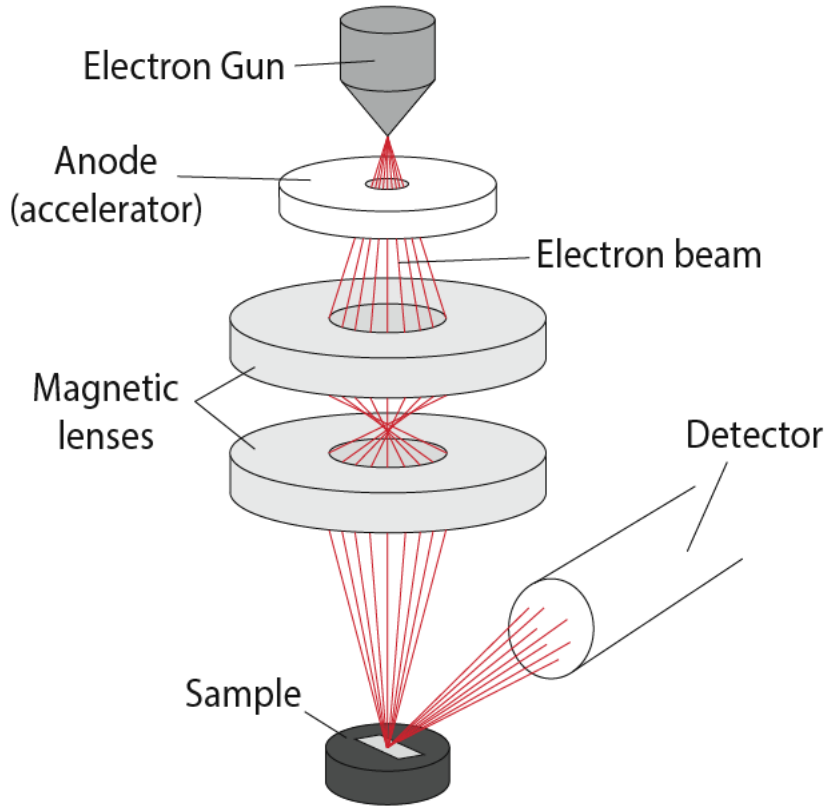

Figure 2.5: A schematic showing the basic structure of a Scanning Electron Microscope [145].

ergy which leads to the emission of weakly bound electrons. The resulting secondary electrons typically have an energy less than 50 eV [144]. The low energy of the SEs result in a short mean free path, as can be seen in Figure 2.7, with the result that only those emitted close to the surface of the sample can reach the detector. Due to this, the interaction volume from which SEs originate (Figure 2.6) is small and SEs can resolve features as small as $\sim$ 10 nm. The potential for high resolution and the high yield of secondary electrons (the number emitted per incident electron is usually greater than 1) mean that SEs are frequently used as the primary imaging signal in SEM.

SEs can be detected using an Everhart-Thornley detector, which is composed of scintillators housed in a Faraday cage. The SEs are attracted to the positively biased cage and accelerated into the scintillators which emit light upon

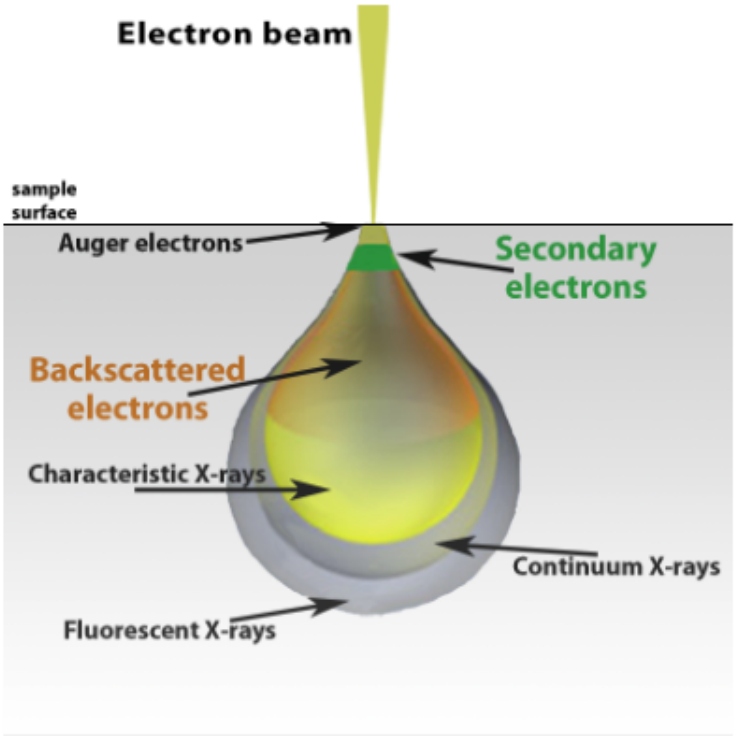

Figure 2.6: An illustration of the interaction of an incident electron beam with a sample in the SEM [147].

the impact of an electron. The light then passes through a photomultiplier for amplification and an image is produced. The detector is placed towards the side of the SEM chamber, with varying inclination, the purpose of this is to increase the efficiency of SE detection. Topographic information in the SE signal originates from a combination of surface asperities preventing the electrons from reaching the detector (which is usually placed at an angle to the surface) and the influence of the local curvature of the sample on the shape of the interaction volume, with sharp, prominent features emitting more electrons.

Backscattered electrons (BSEs) originate from the incident electron beam and are the result of single or multiple scattering, with the scattered electron directed at angles greater than 90° to the incident beam direction. The BSEs typically have energies of 60-80% of the original beam (although any electron escaping the sample with greater than 50 eV is typically considered a BSE) [144, 148] and as a result can originate from deeper within the sample than SEs, as can be deduced from the 'universal curve' of electron mean

free paths in solids, Figure 2.7. Hence, the BSE signal is associated with a larger interaction volume and offers a lower resolution (by up to two orders of magnitude) than the SE signal.

BSEs are detected through the use of a solid-state detector or scintillator/semi-conductor based detector placed concentrically about the incident electron beam. The BSE yield is dependent on the atomic number of the scatterer, with heavier elements producing a stronger signal and, as a result, can yield useful information about the elemental composition of the sample, as well as providing information about the structure of the sample beneath the immediate surface.

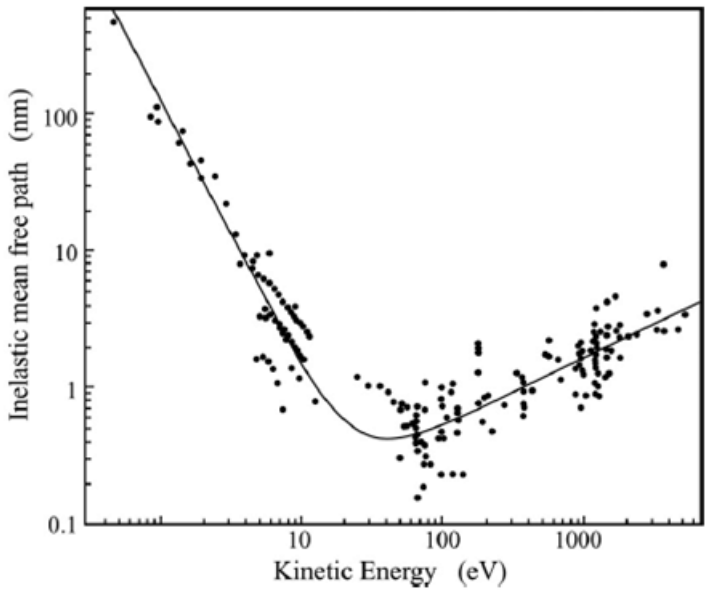

Figure 2.7: The 'Universal Curve' of inelastic mean free path of electrons in a solid as a function of kinetic energy [149].

2.4 Electrochemical Analysis

For characterising battery and supercapacitor materials two types of cell construction can be employed – three electrode or two electrode [150]. The first configuration, as the name suggests, utilises three electrodes termed the working, reference and counter electrodes, as shown in Figure 2.8. These electrodes are immersed in a volume of a suitable electrolyte and the relative potential between the working and counter electrode is controlled by a potentiostat. The reference electrode, such as the silver chloride electrode

(A_g/A_gCl) have a fixed potential and provide a reference against which the potential of the working electrode (which consists of the material to be characterised) can be measured. Finally, the counter electrode serves to complete the circuit and balance the processes taking place in the working electrode. When performing a voltammetric measurement, such as cyclic voltammetry (CV), the potentiostat measures the current passing between the working and counter electrodes as a function of the applied bias, whereas in galvanostatic mode a constant current flow between those two electrodes is maintained and the potential required recorded.

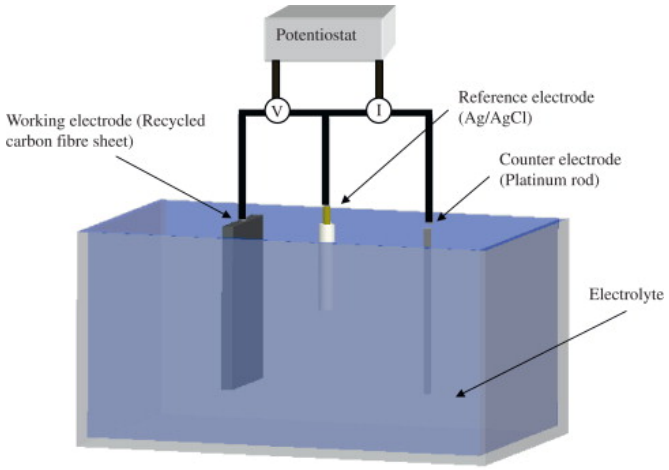

Figure 2.8: Schematic of a three electrode electrochemical cell configuration [151].

On the other hand, Figure 2.9 illustrates a typical two electrode cell configuration. This particular configuration replicates a conventional supercapacitor or battery cell and it can be argued that it provides a more realistic assessment of performance [150]. In a symmetric two-electrode cell both electrodes are composed of the material under investigation and act as anode and cathode. A separator is placed in between the electrodes to prevent short circuit and the interface and contacts are doused in electrolyte. Finally, the cell is enclosed in a cell holder which is designed to apply even pressure across the supercapacitor electrodes and ensure no external particles, such as dust, interfere with the electrochemical process and degrade the electrolyte.

Khomenko et al. conducted electrochemical anaylsis on multiwall carbon nanotube/polyaniline electrodes using both configurations to determine the variance in measured capacitance between the two approaches [153]. They found that the measured capacitance varied with the test configuration. For the three electrode cell capacitance was found to vary from 250 to

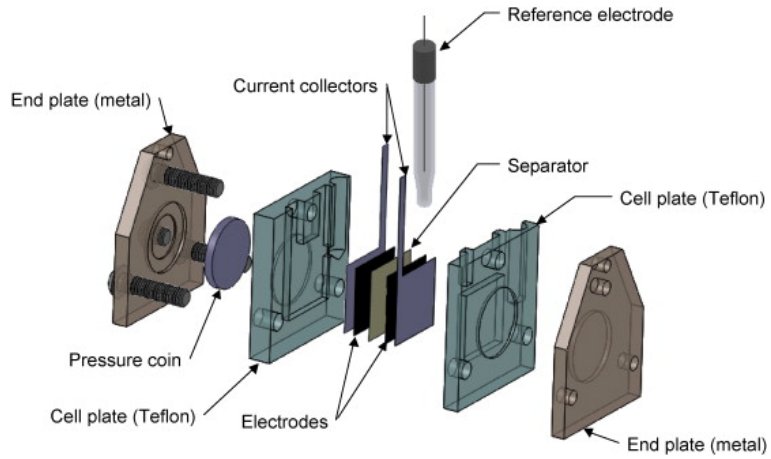

Figure 2.9: Schematic of a two electrode electrochemical cell [152].

1100 F g^{-1}, whereas, for the two electrode cell the capacitance varied from 190 to 360 F g^{-1} using the same material. It is evident that the measured capacitance in the three electrode configuration is significantly larger than that obtained from the two electrode measurements. Stoller and Ruoff [150] argue that the increased capacitance measured in the three electrode configuration originates from processes such as the repolarisation of the working electrode as the potential of zero charge is unknown – i.e., the behaviour of the working electrode changes from anodic to cathodic (or vice-versa) during a voltage sweep which leads to an overestimate of the values of capacitance compared with a practical supercapacitor cell. As the focus of this study is the evaluation of electrode materials produced by scalable techniques which could be suitable for commercial application a two-electrode configuration was therefore considered to be the most appropriate.

2.4.1 Cyclic Voltammetry

Cyclic Voltammetry (CV) is a powerful electrochemical technique employed to understand the processes which can occur at the surface of an electrode as the result of an applied potential. These can be redox reactions involving electron transfer to/from the electrode (Faradaic processes) or physical processes such as the formation of an electric double layer. The relative simplicity and versatility of this technique means that it can be employed to study chemical reactions, determine the concentration of electrochemically active species in a solution and, as here, characterise electrochemical energy storage systems.

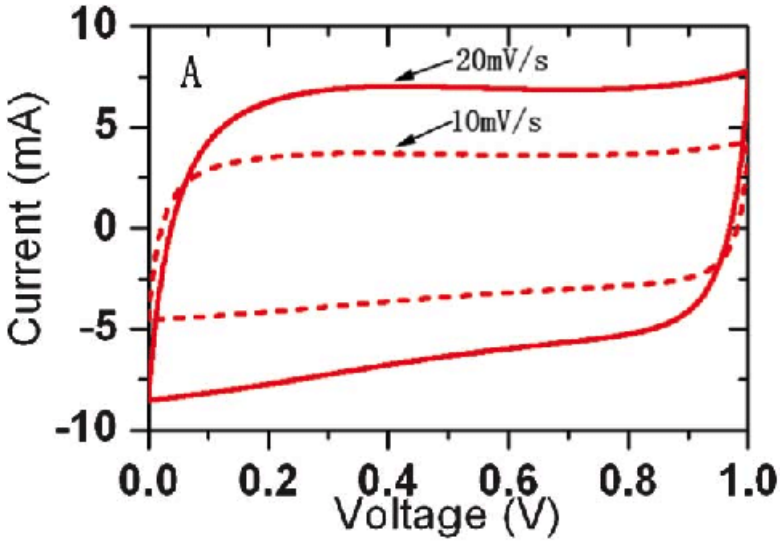

Figure 2.10: An example of a Cyclic Voltammogram and the importance of scan rate [154].

In a cyclic voltammetry (CV) experiment the voltage between the cell electrodes is varied cyclically between two bounds at a predetermined rate and the cell current measured as a function of this applied potential, Figure 2.10 shows a typical cyclic voltammagram. It should be noted that, although the term 'voltage' is typically used in the literature even when referring to two-terminal measurements and will be used to label the axes in voltammagrams presented in this thesis, it would be more correct in two-terminal case to describe this as the 'cell voltage' since it is not measured with respect to a well-defined electrochemical reference.

The total capacitance of the cell, C_T can be determined straightforwardly from a cyclic voltammagram, starting from the expression for the charge stored, Q at a cell voltage V,

$$Q = C_T V \tag{2.8}$$

Differentiating equation 2.8 with respect to time yields,

$$\frac{\mathrm{d}Q}{\mathrm{d}t} = C_T \frac{\mathrm{d}V}{\mathrm{d}t} \tag{2.9}$$

or

$$i = C_T \frac{\mathrm{d}V}{\mathrm{d}t} = C_T r \tag{2.10}$$

where r is the rate of change of voltage. When determining the cell capacitance the current is usually measured on the discharge part of the cycle.

If the assumption is made that the charging and discharging processes involve an identical transport of charge, C_T may be extracted from the area contained within a single CV loop by,

$$C_T = \frac{1}{2r\Delta V} \oint i(V)dV \tag{2.11}$$

where $\Delta V = |V(t_1) - V(t_2)|$ is the voltage range of the CV cycle.

The total capacitance, C_T, of a symmetric two-electrode cell can be considered as originating from two capacitors in series, associated with the electric double layers forming on each electrode. Hence, we can write:

$$\frac{1}{C_T} = \frac{1}{C_+} + \frac{1}{C_-} \tag{2.12}$$

where C_T is the total capacitance of the cell, C_+ is the capacitance of the positive electrode and C_- is the capacitance of the negative electrode. Since, in a symmetric configuration the two electrodes are identical $C_+ = C_-$ and,

$$C_{el} = 2C_T \tag{2.13}$$

where C_{el} is the capacitance of an individual electrode. The specific capacitance can therefore be determined from the total electrode mass, m, by the relation,

$$C_{sp} = \frac{2C_T}{m_{el}} = \frac{4C_T}{m} \tag{2.14}$$

where m_{el} is the mass of a single electrode.

2.4.2 Galvanostatic Charge Discharge

Galvanostatic Charge Discharge (GCD), is another electrochemical technique (often used in combination with CV) to assess an energy storage device. GCD is different to CV, and involves the application of a constant positive/negative current to charge/discharge a particular device within a set potential limit, as shown in Figure 2.11. By repeating the cycles the cyclability, or long-term charge storage capacity, can be measured. The experimental setup employed is identical to that used in CV measurements.

Various parameters can be determined from a GCD curve, for example: capacitance, energy, effective series resistance (ESR) etc. In addition, GCD allows one to understand the life cycle of a device and potential presence of irreversible Faradic reactions [156].

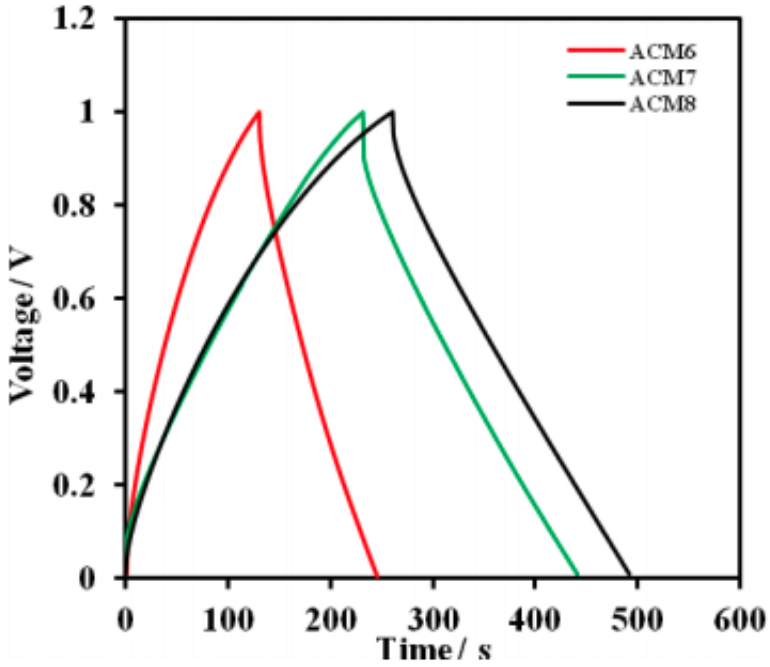

Figure 2.11: An example of a GCD curve [155].

Chapter 3

Experimental Procedure

3.1 Liquid Phase Exfoliation

To produce suspensions of few-layer graphene or MoS_2 by high shear exfoliation a mixture of ultra high purity (UHP) water (resistivity 18.2 MΩ cm), a suitable anionic surfactant (Triton X-100 - t-Octylphenoxypolyethoxyethanol) and flakes of the parent material were subjected to high shear mixing using a Silverson Model L5M-A Laboratory mixer, Figure 3.1. Triton X-100 was chosen as the surfactant because previous work within the group had shown that suspensions of high concentration could be created reproducibly and the use of an non-ionic surfactant was found to avoid significant residual contamination [157].

Quantities of material used in the shear mixing process were selected which had produced high concentrations of material in previous studies [157]. In the case of few layer graphene, 40 g of graphite flakes (Large Flake Natural Graphite, Mesh size +590, minimum 70% flakes larger than 300 μm, >90% carbon, ProGraphiteShop, Germany) were mixed with 1.25 g of Triton X-100 (Sigma-Aldrich) and 500 ml of ultra-pure water (Elga Purelab). For MoS_2 6.25 g of MoS_2 (Sigma-Aldrich) was mixed with 0.625 g Triton X-100 and 250 ml of UHP water.

Mixtures were exfoliated through high shear mixing with a 1 in diameter square hole high-shear screen, Figure 3.1. This attachment enables the shear mixer to generate high shear rates and is ideal for the reduction of solids. The shear rate produced by the mixer is given by the relation [108]:

$$\dot{\gamma} \approx \frac{\pi N D}{\Delta R} \tag{3.1}$$

where $\dot{\gamma}$ is the shear rate, N is the shear mixing speed, D is the rotor diameter (22 mm) and ΔR the gap between rotor and stator (100 μm). Hence, for a shear mixing speed of 3,000 RPM the shear rate is $\sim 1 \times 10^7$ s^{-1} which is greater than the minimum shear rate of $\sim 10^4$ s^{-1} for exfoliation determined by Paton and co-workers [108].

Figure 3.1: Silverson Laboratory Mixer Model L5M-A.

For the production of graphene suspensions shear rates of 3000 RPM to 9000 RPM were used with increments of 2000 rpm and the material exfoliated for a duration of 120 minutes. After the process had been completed, the mixture was decanted into 50 ml centrifuge tubes and then placed in a centrifuge system to remove poorly exfoliated material. These tubes were centrifuged at 2000 RPM for 60 minutes and once the process had finished the top 40 ml from each of the eight centrifuge tubes was decanted into a 250 ml glass bottle. The remaining 10 ml of suspension contained the sediment and heavier (thicker) platelets and so was discarded. For the MoS_2 samples mixing speeds of 3000 RPM to 8000 RPM were chosen with increments of 1000 RPM and the suspensions exfoliated for a duration of 40 minutes. The shear mixer was situated 4.2 cm from the bottom of the container on each occasion in a centred position to ensure reproducibility. As with the graphene, the as-exfoliated material was placed into centrifuge tubes. These tubes were centrifuged first at 1500 RPM and then at 3500 RPM, for 99 minutes at both speeds. Following centrifugation the top 40 ml of the suspension was, once again, extracted.

3.2 UV-Vis spectrometer

A Shimadzu UV-3600 UV-Vis spectrometer, as shown in Figure 3.2, was used to determine the concentration of suspensions of few-layer graphene and MoS_2. 4.5 ml of the centrifuged suspensions was pippetted into a quartz cuvette for measurement. As the centrifuged suspensions of MoS_2 were dilute enough to be measured by the UV-Vis spectrometer, they could be decanted directly into the cuvette. However, for the centrifuged suspensions of graphene the suspension had to be diluted with UHP water as they were opaque. The amount of UHP water used to dilute the suspensions for shear rates of 9000 RPM, 7000 RPM and 5000 RPM was 300 ml, whereas for 3000 RPM the amount used was 100 ml. These amounts were chosen to ensure that sufficient exfoliated material was present within the cuvette to obtain a clear signal whilst maintaining sufficient transparency for characterisation. In each case a reference sample consisting of a mixture of UHP water and Triton X-100, with a concentration matching that of the (diluted) suspensions used was placed in a second cuvette and the difference spectrum measured in order to determine the concentration of the two-dimensional material. For MoS_2, the wavelength range measured was 400 nm to 800 nm in steps of 0.2 nm, whilst for graphene it was 300 nm to 800 nm. The slit width used in all experiments produced a nominal resolution of 1 nm.

(a) UV-Vis spectrometer.

(b) Cuvette housing.

Figure 3.2: (a) The UV-Vis spectrometer used to determine concentration and number of layers of the exfoliated two-dimensional platelets of MoS_2 and graphene; (b) the cuvette housing, with the reference cell holder being furthest to the back.

3.3 Vacuum filtration of Graphene and MoS_2 samples

Vacuum filtration was used to produce binder-free free standing electrodes of graphene and also to isolate few-layer MoS_2 platelets for analysis. The filtration system is shown in Figure 3.3 and suspensions were filtered onto cellulose nitrate membrane filters, sourced from Whatman, with a pore size of 0.1 μm and diameter of 47 mm. The filter membranes were carefully inspected to ensure that they were clean and free of damage before being placed on the glass frit of a funnel mounted on a vacuum pumped side-arm flask and then clamped securely into place. To create the free-standing graphene foils from which electrodes were cut, a quantity of suspension was chosen, based upon the concentration determined from UV-vis spectroscopy to produce a total of $\sim$ 120 mg of few-layer graphene aggregated on the filter membrane. After filtration the resulting material was washed with an amount of UHP water equal to 1.5 times the volume of the initial suspension. The filtered material was then placed on a hot plate overnight at 50°C to dry. Two 15 mm diameter circular electrodes were cut from the resulting few-layer graphene 'paper', which could be peeled from the filter membrane. The remaining material from the film was retained for analysis by Raman spectroscopy and SEM. For MoS_2, 80 ml of suspension produced at a given shear rate was filtered and washed with 200 ml of UHP water and the sparse dispersion of few-layer platelets characterised by SEM.

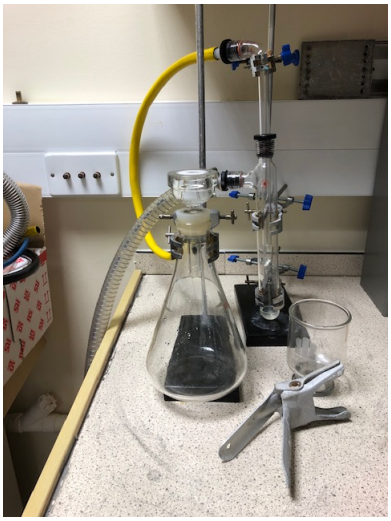

Figure 3.3: Vacuum filtration apparatus.

3.4 FEI Helios Nanolab 600 DualBeam FIB/SEM

Figure 3.4: The FEI Helios Nanolab 600 DualBeam system [158].

The few-layer graphene electrode materials were characterised with a FEI Helios Nanolab 600 DualBeam FIB/SEM. This instrument can be operated in focused ion beam (FIB), electron beam (SEM) or dual modes, Figures 3.4 and 3.5. In the work presented in this thesis the SEM imaging mode was chosen. The microscope has a Schottky-type field emission source which offers beam currents of up to 22 nA and accelerating voltages up to 30 kV, with a nominal resolution of 0.9 nm at a beam energy of 15 keV. To produce the best images of the surface of the electrode samples, various beam energies, accelerating voltages and currents were tested, along with the different imaging modes, both SE and BSE. Eventually, SE imaging with a beam energy of 8 keV and a beam current of 0.34 nA were chosen.

3.5 Zeiss EVO SEM

Unlike the continuous films produced for the few-layer graphene electrodes, the filtration of the MoS_2 suspensions resulted in isolated platelets sparsely dispersed on the cellulose nitrate membrane. Although such a dispersion is ideal for characterisation of the size distribution of the MoS_2 platelets, the non-conductive nature of the membrane filter meant that a conventional high vacuum SEM, such as that described in section 3.4 could not be successfully employed in imaging these samples due to excessive charging. Instead a Zeiss EVO SEM, Figure 3.6, was employed under low vacuum conditions, with the admitted air molecules neutralising the membrane charge and enabling imaging to take place.

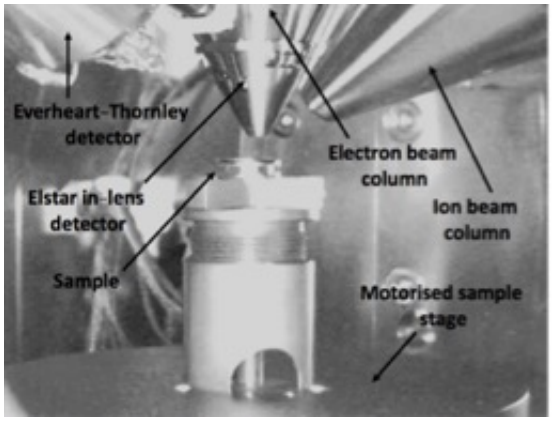

Figure 3.5: Chamber of the FEI Helios Nanolab 600 DualBeam FIB/SEM [158].

The Zeiss EVO microscope has a LaB_6 thermionic electron source and can reach a nominal resolution of 2 nm at 30 kV in SE imaging mode. In addition to operating under high vacuum (HV – 2×10^{-5} mbar), the microscope can operate in an extended pressure (EP) range of 10 to 3000 Pa enabling the imaging of delicate samples and the neutralisation of charge in insulators. Images can be formed using SEs or BSEs in HV mode or BSEs in EP mode. For the sparse MoS_2 platelets images were obtained using BSEs in EP mode at a pressure of ~ 40 Pa and a beam energy of either 15 keV or 20 keV, with the energy chosen in order to produce the clearest possible images.

3.6 ASEQ RM1 Raman Spectrometer

The ASEQ Instruments RM1 Raman spectrometer, Figure 3.7, is a low-cost Raman spectrometer consisting of a low-noise 200 mW laser operating at a wavelength of 532 nm, a 10× objective lens with a 10 mm working distance, a thermoelectrically-cooled charge coupled device (CCD) spectrometer and associated focusing optics. Rayleigh scattered radiation was removed by a Semrock long-pass filter, which blocks wavelengths up to 537 nm, hence only Stokes scattered photons can be observed. The HR1-T CCD spectrometer has 3648 pixels and the overall system resolution is 12 cm^{-1}. Samples are mounted vertically on a home-built motorised stage with stepper motor control in the x, y plane (perpendicular to the axis of the objective lens), and manual control in the z direction (parallel to the axis of the objective lens). Raman spectra were obtained with a laser power of 4 mW at the sample, which corresponds to a laser power of $\sim 1.5 \times 10^4$ mW cm^{-2}. This power

Figure 3.6: Zeiss EVO SEM.

Figure 3.7: The ASEQ RM1 Raman spectrometer

was chosen as it afforded the greatest signal without any danger of sample damage.

The associated application software, ASEQ spectra, was used to produce the Raman spectra. Prior to data acquisition, the thermoelectric cooling system

on the HR1-T spectrometer was operated for at least an hour to ensure stable low-noise operation. Once the temperature of the spectrometer had become stable, a background 'dark' spectrum was obtained under the same conditions as the acquired spectra and subtracted, to remove the effect of 'hot' pixels in the spectrometer.

3.7 Potentiostat/galvanostat

A USB-controlled potentiostat/galvanostat was built following the design of Dobbelaere et al. [159], as shown in Figure 3.8. This relatively simple potentiostat/galvanostat allows numerous electrochemical tests, such as cyclic voltammetry, galvanostatic charge and discharge and rate testing, to be performed on a electrode test configuration. The performance metrics of the device are a sample rate of 90 ms, potential range of ±8 V, current ranges from ±2 μA to ±20 μA and potential and current resolution of 22-bits. The performance is comparable to low-cost commercial instruments such as the Squidstat Solo [159].

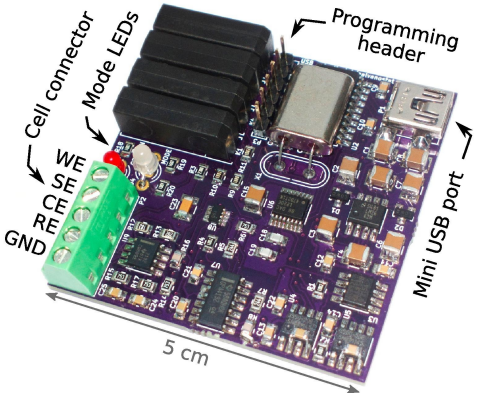

Figure 3.8: Main board of potentiostat/galvanostat, with annotations indicating the ports used to connect electrodes, USB connection to the PC and LEDs to indicate the different operation modes [159].

In measurements performed on a symmetric supercapacitor cell, such as those reported in this thesis, reference and counter electrode connections of the potentiostat are both connected to one electrode whilst the working electrode and voltage sense connections are attached to the other.

A commercial split cell, Figure 3.9, was used for the electrochemical characterisation. Two identical 15 mm diameter FLG electrodes were placed on either side of a porous membrane separator (Celgard 2500, thickness 25 μm,

porosity 55%) and clamped firmly between two synthetic graphite plates (Olmec Advanced Materials) with an electrolyte of 6M KOH.

Cyclic voltammagrams were measured between 0 and 0.9 V, the upper limit to avoid degradation of the electrolyte. A 'one sided' rather than symmetric voltage range was chosen to avoid changing electrode polarisation which, as described above, can produce misleading results for the cell capacitance. CV scans were performed at voltage ramp rates of 5, 10, 25 and 50 mV s^{-1} with 50 cycles performed at each rate.

GCD measurements were performed over the same voltage range as the cyclic voltammetry with charge/discharge currents typically of $\pm 1 \times 10^4$ μA over 10,000 cycles with the number of cycles limited by available laboratory time.

Figure 3.9: The split terminal electrochemical test cell used for CV and GCD measurements.

Chapter 4

Free-Standing Binder-Free FLG Supercapacitor Electrodes

4.1 Introduction

As discussed in Section 1.6, two dimensional materials such as FLG have significant potential for use in supercapacitor electrodes due to their high surface areas, conductivity and desirable chemical properties. In this chapter the production and characterisation of electrodes fabricated from FLG produced by high shear exfoliation is described. The aims of the study are two-fold: (1) to examine the feasibility of producing homogeneous free-standing, binder-free electrodes which can form the basis for the future production of heterogeneous composite electrodes, including MoS_2-graphene heterostructures; (2) to investigate the impact of platelet size and, indirectly, the presence of edge defects on the specific capacitance of FLG electrodes.

4.2 Characterisation of FLG Supercapacitor Electrodes

4.2.1 UV-vis spectroscopy

FLG suspensions were produced at four different shear rates, as outlined in Section 3.1. The absorption spectra of samples produced at each of the shear rates is shown in Figure 4.1. From Figure 4.1 it can be seen that the absorbance of the 3000 RPM batch is the highest, followed by 7000 RPM, 9000 RPM and 5000 RPM. The absorption spectra obtained from the FLG

suspensions all have the same form and are characteristic of pure graphene, showing a monotonic increase in absorption with decreasing wavelength, resulting from a combination of a uniform absorption in the visible range resulting from intraband absorption and the tail of a $\pi \rightarrow \pi^*$ transition in the UV at 270 nm [160].

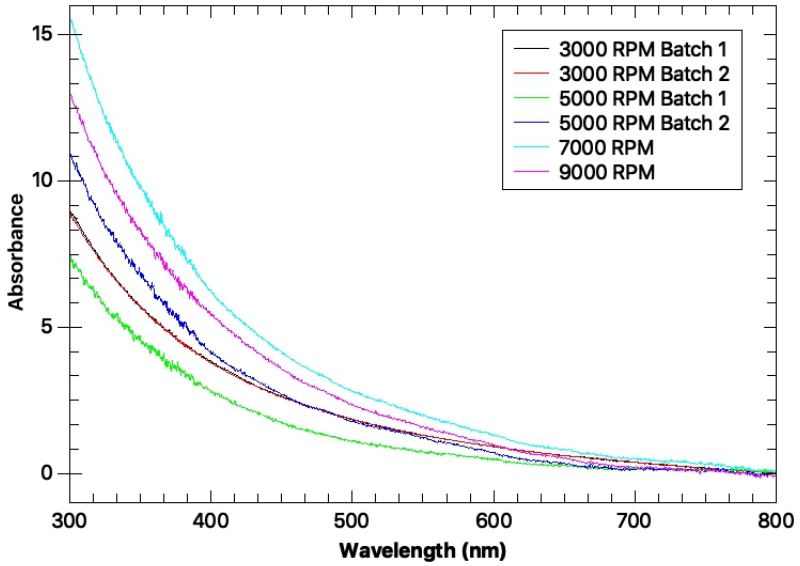

Figure 4.1: UV-Vis spectra obtained from suspensions of FLG produced at differing shear rates.

The concentration of each suspension was evaluated using the Beer-Lambert law, equation 2.1, using the absorption coefficient at a wavelength of 660 nm, which is far from the intraband absorption peak and is presented in Table 4.1. There are a range of values of absorption coefficients reported in the literature [161, 162], due to the fact that the measured 'absorption coefficient' includes the effects of scattering, particularly in concentrated suspensions. The relative opacity of the suspensions indicates the scattering is likely to play a role in the absorption measurements presented here. The value of absorption coefficient reported by Lotya and co-workers [163] of $\alpha = 1390$ ml mg^{-1}, determined from graphene exfoliated into surfactant suspensions, was chosen due to its close agreement with the concentrations determined gravimmetrically through weighing the vacuum filtered FLG films. From the data presented in Table 4.1 there is a general increase in concentration with shear speed, as would be expected from previous work [108]. However, there is a batch to batch variation in concentration of around 50%, the origin of which is not obvious and which may suggest some considerable sensitivity of the measured

concentration to either shear exfoliation conditions or the conditions under which the UV-vis measurements were made.

Once the concentration of the suspensions were ascertained, the quantities required to produce a target mass of 120 mg on the filter membrane by vacuum filtration were determined, with dry masses found to range between 93 ± 2 mg and 130 ± 2 mg.

Shear Rate (RPM)	Concentration (g ml^{-1})
9000	0.00042
7000	0.00074
5000 batch 1	0.0002
5000 batch 2	0.00027
3000 batch 1	0.0002
3000 batch 2	0.0003

Table 4.1: Concentration of the FLG samples produced through shear exfoliation.

4.2.2 Raman Spectroscopy

Figure 4.2 shows typical Raman spectra obtained from the vacuum filtered FLG films produced from material exfoliated at differing shear mixing speeds. The Raman spectra were obtained by Dr. M.R.C. Hunt. All spectra have the same form, with three prominent peaks located at ~ 1350 cm^{-1}, ~ 1580 cm^{-1} and ~ 2700 cm^{-1}. These three bands are known as the D, G and $2D$ (or G') bands, respectively [164], and their relative intensities are able to provide considerable insight into the structure and defect density of the FLG based supercapacitor electrodes.

The G band corresponds to doubly degenerate optical phonons of E_{2g} symmetry situated at the centre of Brillouin zone and represent the in-plane vibrations of the carbon atoms excited by a singly resonant process. The significance of this band is that it is affected by the number of layers of graphene, as the number of layers increase the band intensity increases. This is due to more carbon atoms contributing to the particular vibration mode [165]. Alongside the correlation with number of layers, the intensity, peak position and shape are affected by factors such as charge, impurities or stress.

The $2D$ band originates from doubly resonant scattering processes involving zone boundary phonons with the shape of this band highly sensitive to the

number of graphene layers within a sample and their relative orientation [166, 167]. A graphene monolayer exhibits a single, relatively narrow (full width at half maximum – FWHM – of $\sim$ 25 cm^{-1}) $2D$ line, which contains four components in the bilayer. The shape of the $2D$ peak further evolves with thickness, reaching that of bulk graphite after approximately 5 layers. An exception is observed for so-called 'turbostratic' graphite in which there is no well-defined stacking order between the individual graphene layers, in this case a single $2D$ peak is observed with a FWHM of $\sim$ 50 cm^{-1}. This broad lineshape can be seen for the $2D$ peaks in Figure 4.2, whereas the parent graphite from which the FLG is exfoliated has a peak and a shoulder. The lineshape of the vacuum filtered FLG film indicates that exfoliation of the parent graphene has occurred under shear mixing and that the formation of a vacuum filtered film has led to a random re-stacking of few-layer graphene platelets to form a 'turbostratic' material.

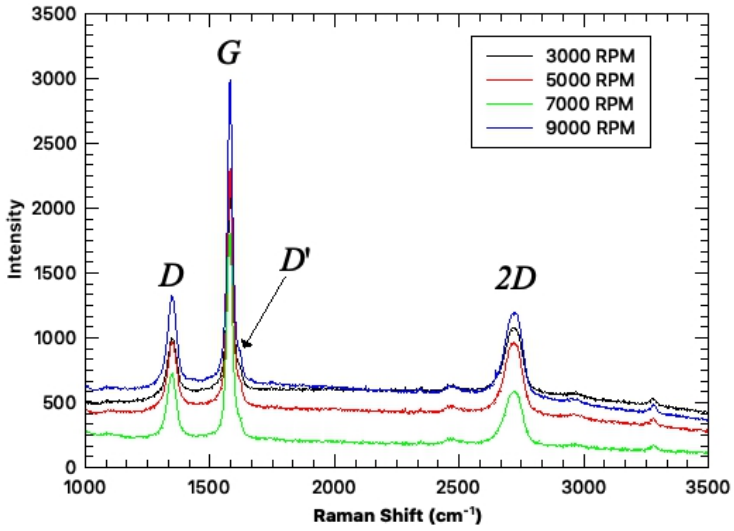

Figure 4.2: Raman spectra of the graphene electrodes produced from FLG exfoliated at shear rates of 3000, 5000, 7000 and 9000 RPM. The D, G, D' and $2D$ modes are labelled.

It was originally suggested that the position of the G peak or the ratio of the intensity of the $2D$ peak to the G peak, $I(2D)/I(G)$ could be used to determine the number of graphene layers within a sample. However, it has been shown by Casiraghi *et al.* that even within a single flake of micromechanically cleaved monolayer graphene there can be a considerable variation in the relative intensity of the $2D$ and G peaks in the absence of defects, which is associated with uncontrolled doping of the sample [167–169]. Like-

wise, Martins-Ferreira and co-workers have shown that these peaks can be influenced by defects (which can introduce self-doping) [170]. Hence, reliance should be placed upon the *shape* of the $2D$ peak, which Paton and co-workers [108] used to derive a 'thickness metric', M which was calibrated by atomic force microscopy (AFM) measurements:

$$M = \frac{I_{Graphene}(\omega_{2DGraphite})/I_{Graphene}(\omega_{2DGraphite} - 30)}{I_{Graphite}(\omega_{2DGraphite})/I_{Graphite}(\omega_{2DGraphite} - 30)} \tag{4.1}$$

where $I_{Graphite}$ and $I_{Graphene}$ are intensities measured on the graphite and graphene Raman spectra respectively and $\omega_{2DGraphite}$ is the position (in cm^{-1}) of the main $2D$ peak in the parent graphite from which the FLG is derived. The average number of layers in the platelets of a vacuum filtered FLG film, N_G is then given by:

$$N_G = 10^{0.84M+0.45M^2} \tag{4.2}$$

with an accuracy of ± 1.5 layers claimed.

Using the metric of Paton *et al.* an average FLG platelet thickness of 4 ± 1.5 layers is determined for all the samples produced here and, once the error suggested by Paton *et al.* is taken into account, there seems to be no variation of thickness with shear speed, Figure 4.3.

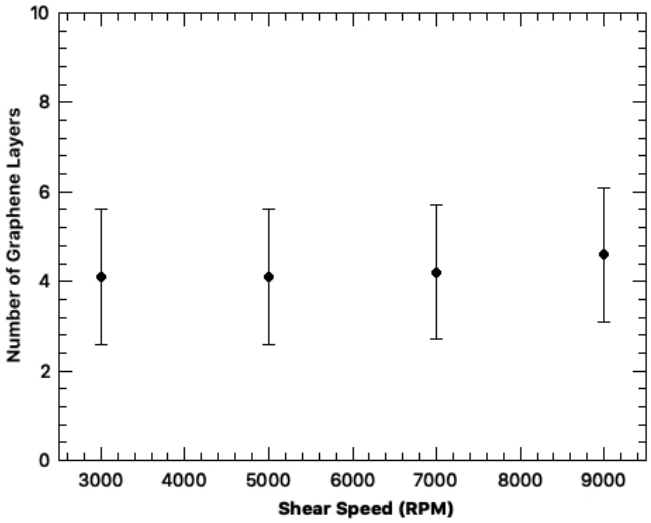

Figure 4.3: Average number of graphene layers in the FLG platelets as a function of shear speed used in their production, derived from Raman spectra using the thickness metric proposed by Paton *et al.* [108].

The presence of a 'defect' in the broadest sense – i.e., where breaking of the two-dimensional translational periodicity of the graphene lattice occurs

– leads to doubly resonant processes involving a single optic phonon: an incident photon is absorbed, creating an electron hole-pair, one of which may undergo scattering with a zone-boundary phonon and subsequently via a defect (the two scattering processes may also occur in the opposite order) followed by de-excitation and the emission of a scattered phonon. If the electron/hole is scattered between Dirac cones (the linear dispersion close to the Dirac points discussed in Section 1.4.1) the result is the D peak in the graphene Raman spectrum associated with the breathing modes of the six-membered graphene rings, whereas scattering within a Dirac cone leads to the D' peak [167]. The defects leading to scattering may be zero-dimensional defects such as vacancies, substitutional impurities and adatoms or two-dimensional defects such as grain boundaries and edges. Eckmann and co-workers have found empirically that the ratio of the amplitudes of the D and D' peaks can be used to deduce the dominant defect type in a defective graphene sample [171]. They found that $I(D)/I(D')$ had a value of ≈ 13 for defects associated with sp^3 hybridisation (arising from impurities covalently bound to the graphene lattice), ≈ 7 for vacancy defects and ≈ 3.5 for 'boundary' defects, such as edges. The result of such an analysis of the data indicates that the edge defects dominate the FLG samples produced in this work.

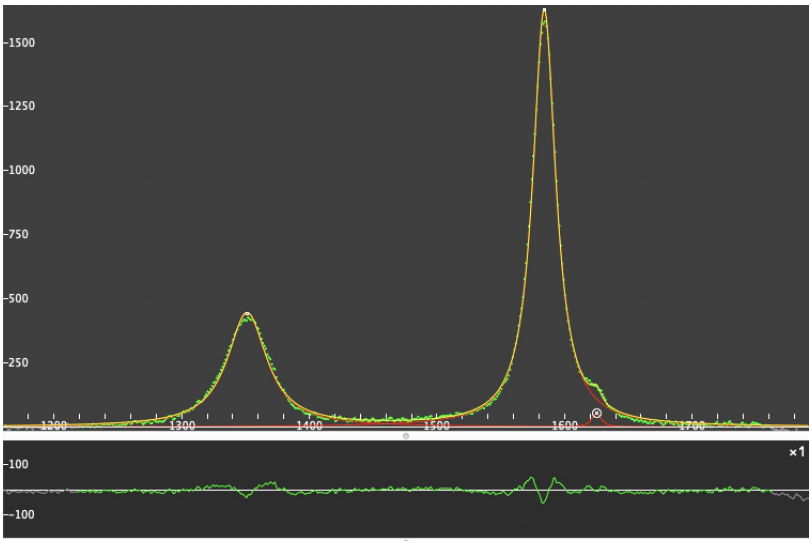

Figure 4.4: Screenshot of a typical Lorentian fit to the D, G and D' bands of a FLG electrode sample produced at a shear speed of 9000 RPM. The upper panel shows the fit, the lower the non-normalised fit residuals.

I_D/I_G was calculated by fitting Lorentzian functions to the respective peaks using the software Fityk, a peak fitting program, as shown in Figure 4.4. Prior to this the linear shift of the Raman spectra had to be corrected for,

this was done by using the Raman spectra obtained from a silicon reference sample at the start of each measurement session, with the silicon Raman peak position being set to 520.5 cm^{-1}. Afterwards, the integrated peak area was derived to determine the respective ratios.

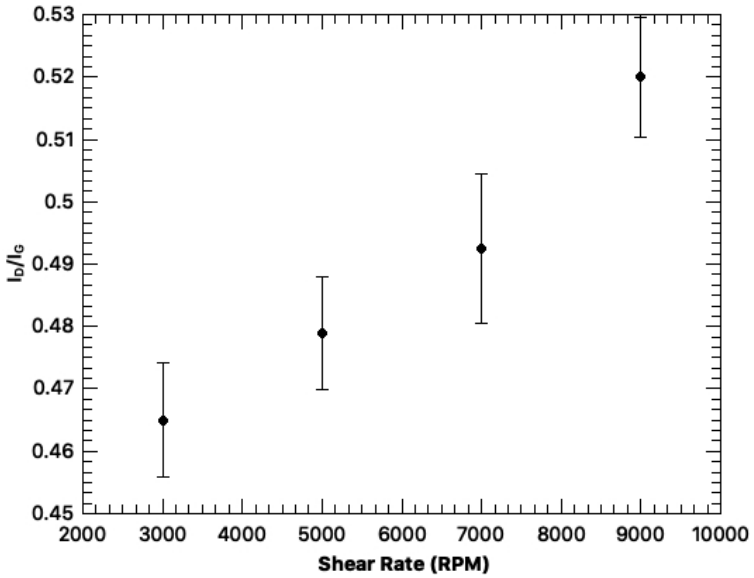

Figure 4.5: The ratio I_D/I_G plotted against shear speed.

The results obtained for the I_D/I_G ratio are shown in Figure 4.5, which indicates that as the shear rate increases the level of disorder associated with the presence of edge defects increases. This is expected as shear exfoliation introduces stress onto the graphite sample in order to break it down into few-layer graphene platelets, with the level of stress applied being proportionate to the shear rate used. However, increasing shear rates reduce the lateral dimensions of the platelets and this introduces an increasing amount of edge defects into the produced sample. Although the trend between disorder and shear rate is established here, it should be noted that the I_D/I_G is still relatively low compared with many 'graphenes' reported in the literature.

Overall, Raman spectroscopy confirms that shear exfoliation is successful in producing few-layer graphene with an average of 4 layers, which can be used as electrodes for energy storage devices and that the dimensions of the FLG platelets decrease with increasing shear speed.

4.2.3 SEM

To provide further insight into the nature of the structure of the FLG electrode samples SEM measurements were made with no further sample preparation. Typical SEM images are shown in Figure 4.6. Although the continuous nature of the films prevents a detailed analysis of the variation of shape and area as developed for few-layer MoS_2 platelets in Chapter 5, some clear trends can be observed. In particular, where edges can be clearly determined there is a decrease in the size of the platelets with increasing shear speed. This is particularly pronounced when comparing films produced at 3000 RPM with those resulting from higher shear speeds. In the former case a number of large, poorly exfoliated platelets can be clearly observed, absent in the other samples. In addition to the apparent decrease in platelet area as the shear speed increases the edges of the platelets increasingly protrude from the surface leading to the bright features in the SEM images. The smaller platelet dimensions and increased roughness (and hence surface area) of the electrode surfaces can be expected to lead to improved supercapacitor performance through an increase in quantum capacitance arising from the edge defects associated with the boundaries of the platelets, as discussed in Section 1.6 and an increase in surface area due to roughness.

It is interesting to note the dark voids which are present in all the electron micrographs, increasing in density with the shear rate. High magnification images (not shown) shows that the interior of the voids also consists of FLG platelets and that there is no evidence of contamination. The smooth and discrete nature of the voids suggests that they do not arise from cracking or damage of the electrodes during the filtration and drying process. One possible origin of these voids is that they originate from micelles of the surfactant, Triton X-100. Although Triton X-100 micelles can best be described as spherical and with maximum diameters < 15 nm at 20 ℃, which is incompatible with the size and shape of the voids in Figure 4.6, at higher temperatures their sizes increase significantly, extending beyond 25 nm at 40 ℃ [172]. Since the suspension was not placed in a temperature-controlled bath during the shear exfoliation process, an increase in temperature of around 10 to 20 ℃ cannot be ruled out. Moreover, Cardiel *et al.* [173] have shown that shearing of other non-ionic surfactants in aqueous environments at shear rates below those used for the production of the FLG suspensions can lead to a transition from spherical micelles with dimensions less than 10 nm to anisotropic 'crystal like structures' with domain sizes up to 20 μm. A similar transition in micelles of Triton X-100 during the shear exfoliation of graphite to FLG might also occur and the resulting large anisotropic surfactant struc-

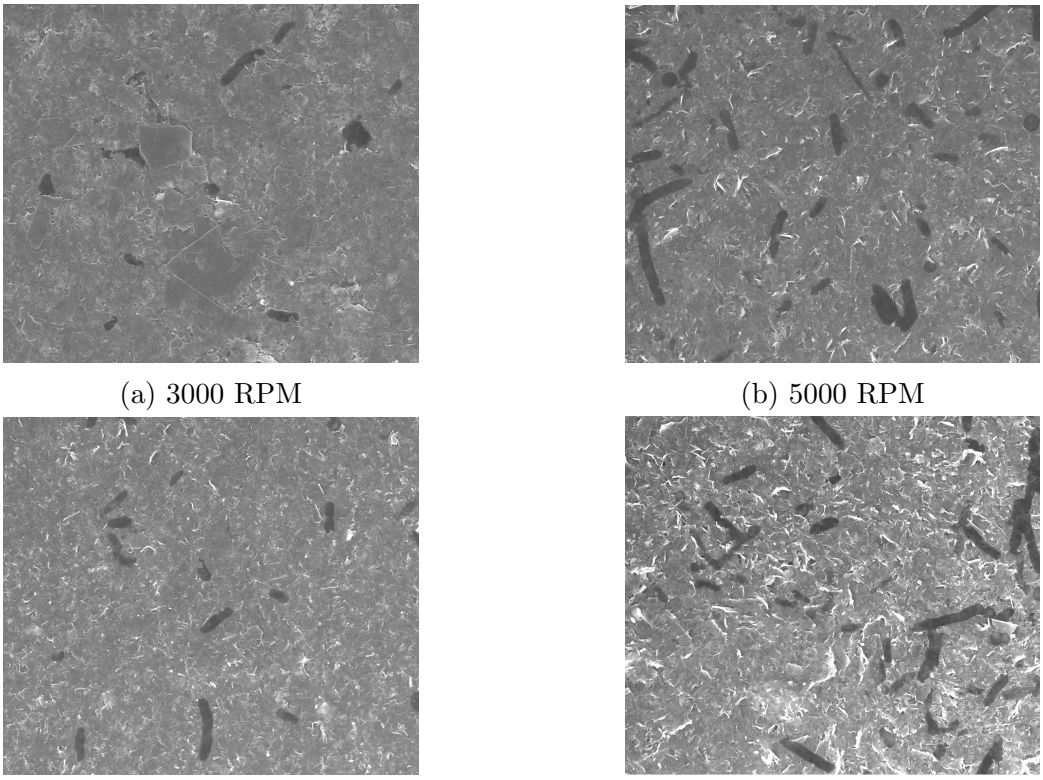

(a) 3000 RPM

(b) 5000 RPM

(c) 7000 RPM

(d) 9000 RPM

Figure 4.6: Example SEM images of FLG electrode samples at various shear rates. The scan area is 10 μm $\times$ 10 μm in all images.

tures may be incorporated into the FLG films in the early stages of vacuum filtration before being removed during the washing stage, leaving behind the voids observed by SEM.

4.2.4 Electrochemical Characterisation

Free standing circular FLG electodes, 15 mm in diameter were cut directly from vacuum filtered films (FLG 'paper') by means of a stainless steel punch. The resulting electrodes were mechanically very robust, despite the absence of any binder, and could be handled with tweezers without any special precautions. Likewise, no additional current collector such as a stainless steel foil or nickel foam was required. The FLG electrodes were weighed with a precision of ± 1 mg before electrochemical characterisation and the results are reported in Table 4.2. The FLG electrodes were then assembled into an electrochemical test cell, without any additional treatment, as described in

Section 3.7. A 25 μm thick polymer membrane (Celgard 2500) was used as a separator and 6M KOH used as the electrolyte. Cyclic voltammetry and choronoamperometry were performed in a two-terminal configuration, chosen as it most accurately reflects the performance of supercapacitor electrodes in a 'real world' application, as discussed in more detail in Section 2.4.

Shear Rate (RPM)	Combined mass (mg)	Electrode 1 (mg)	Electrode 2 (mg)
9000	120	20	20
7000	104	16	18
5000	130	18	20
3000	97	15	16

Table 4.2: Measured mass of the FLG electrodes produced. Masses are accurate to ± 1 mg.

Figures 4.7-4.13 show typical cyclic voltammagrams obtained from the free-standing FLG electrodes at four different scan rates. In each case the 20th (of 50) CV cycle was used to determine the specific capacitance of the samples to ensure that equilibrium charging/discharging conditions had been reached. However, in practice, it was found that the voltammagrams rapidly converged to their final shape and then remained practically unchanged.

The cyclic voltammagrams of all electrode samples are close to ideal, particularly at low scan rates. Additionally, they show no evidence of any redox-related peaks, indicating that energy storage is dominated by the formation of an electric double layer, with no pseudocapacitive or faradiac behaviour present.

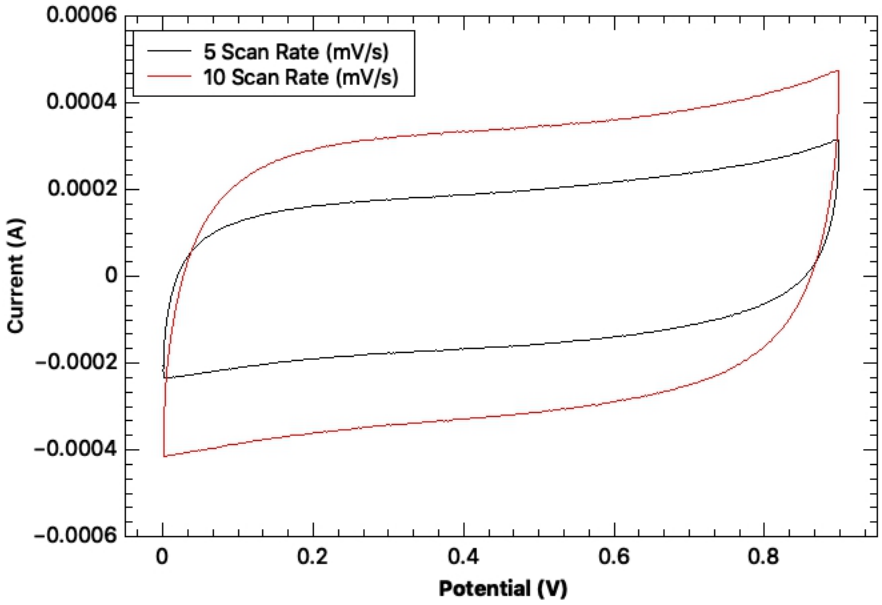

Figure 4.7: CV curves for the electrode produced from FLG shear exfoliated at 3000 RPM at 5 and 10 mV s^{-1} scan rates.

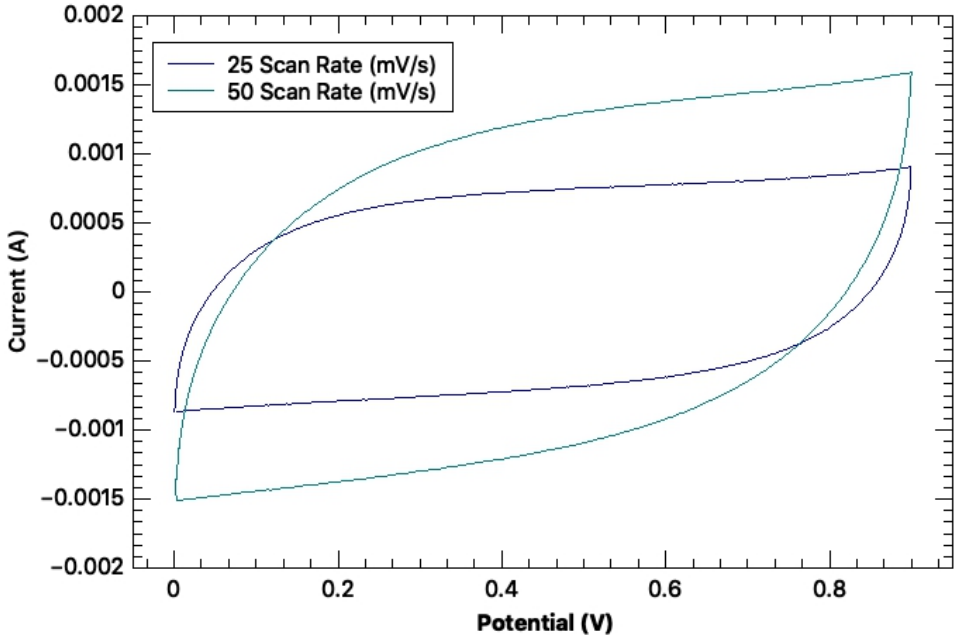

Figure 4.8: CV curves for the electrode produced from FLG shear exfoliated at 3000 RPM at 25 and 50 mV s^{-1} scan rates.

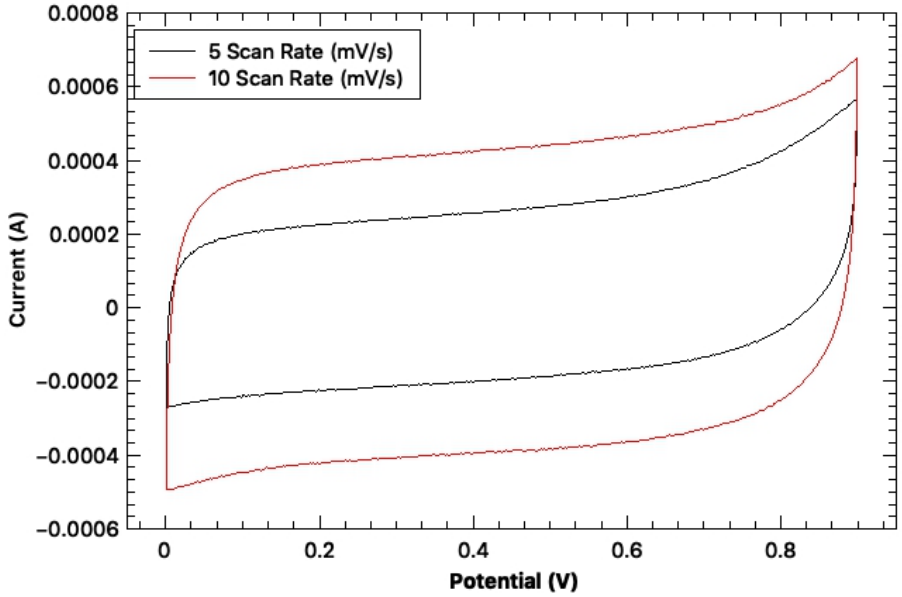

Figure 4.9: CV curves for the electrode produced from FLG shear exfoliated at 5000 RPM at 5 and 10 mV s^{-1} scan rates.

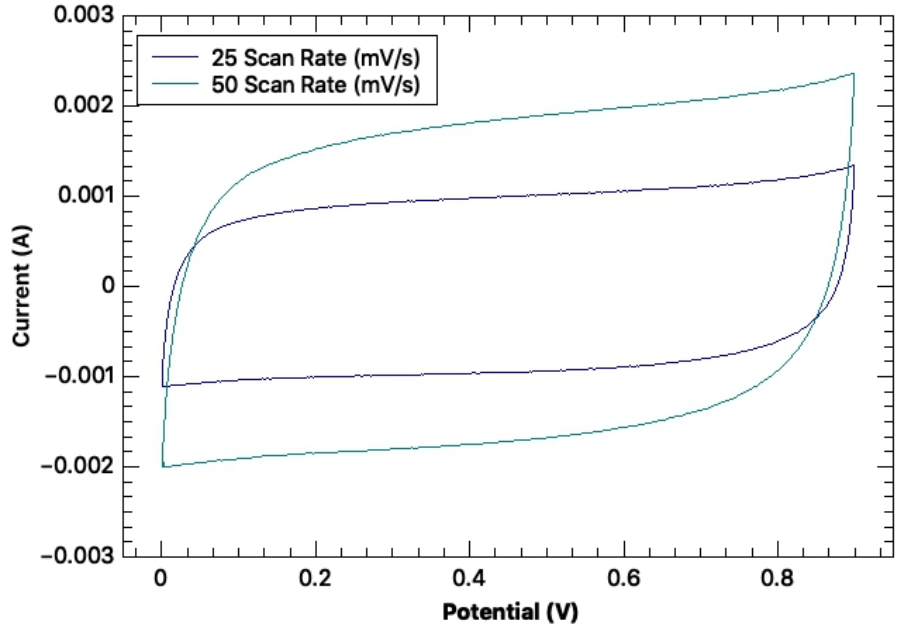

Figure 4.10: CV curves for the electrode produced from FLG shear exfoliated at 5000 RPM at 25 and 50 mV s^{-1} scan rates.

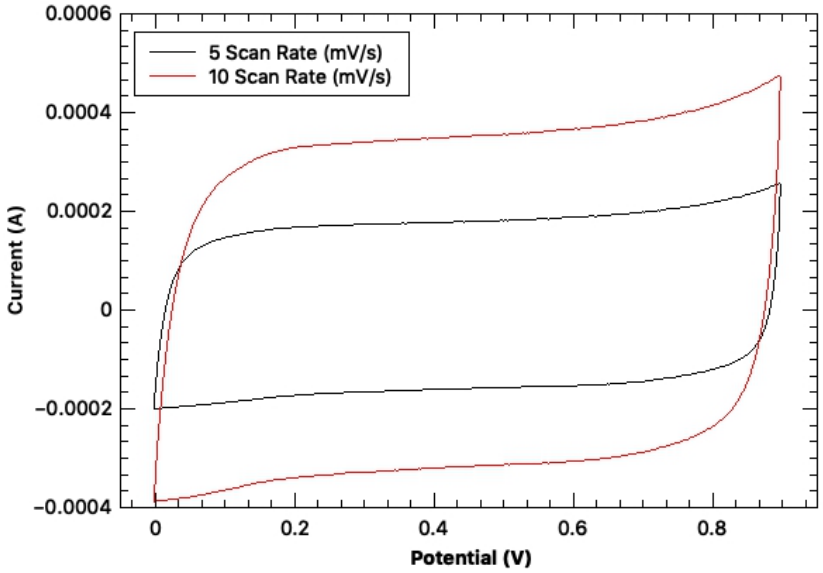

Figure 4.11: CV curves for the electrode produced from the second FLG sample shear exfoliated at 7000 RPM at 5 and 10 mV s^{-1} scan rates.

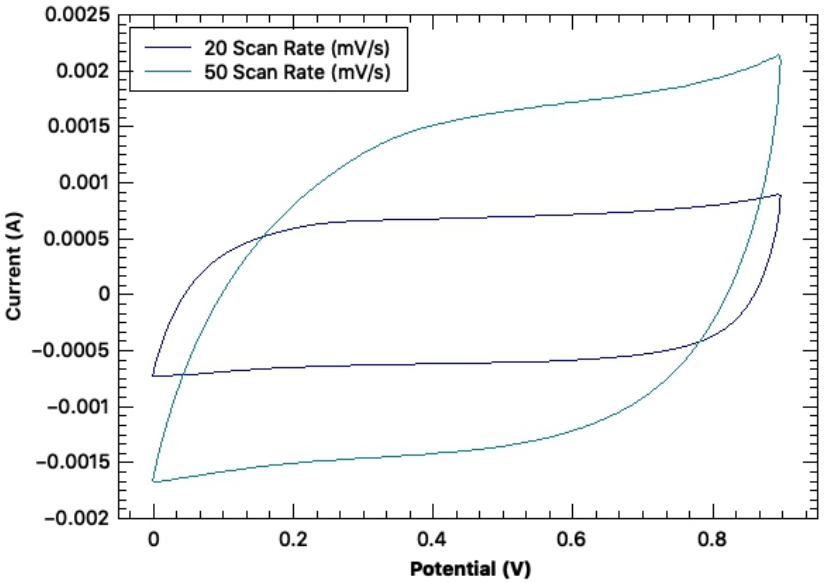

Figure 4.12: CV curves for the electrode produced from the second FLG sample shear exfoliated at 7000 RPM at 20 and 50 mV s^{-1} scan rates.

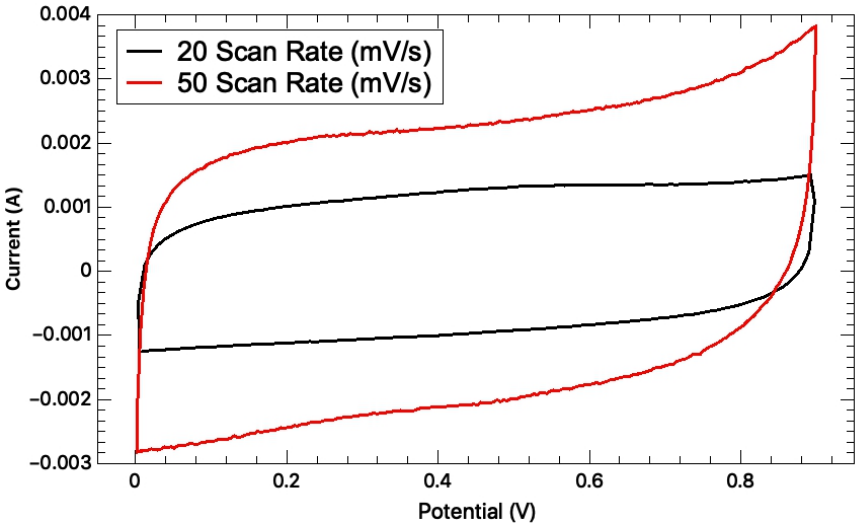

Figure 4.13: CV curves for the electrode produced from FLG shear exfoliated at 9000 RPM at 20 and 50 mV s^{-1} scan rates.

The specific capacitances of the FLG electrodes was calculated from equations 2.11 and 2.14 using a Python script written by Dr. M.R.C. Hunt and are reported in Table 4.3 and, for a voltage sweep rate of 50 mV s^{-1}, Figure 4.14. The data show a clear trend of increasing specific capacitance as a function of increased shear speed for the production of the FLG.

The Raman spectra reported in Section 4.2.2 indicate that there is a decrease in FLG platelet size and hence an increase in edge defects as shear speed increases. Hence, as outlined in Section 1.6 we expect that, according to equation 1.4, an increase in the quantum or intrinsic capacitance, C_Q, of the FLG will occur [124]. Since the quantum capacitance of the individual FLG platelets can be expected to limit the performance of FLG electrodes [119, 124] an increase in C_Q should improve the overall specific capacitance of the electrodes, as is observed.

Although it is tempting to draw the conclusion that the increasing ratio of edge to two-dimensional 'bulk' is the underlying cause of the increase in specific capacitance with the shear speed at which the FLG is produced, some caution is advised. It must be borne in mind that changes to FLG platelet size can also, in principle, lead to a variation in the surface area and porosity of the electrodes and there is some possible evidence for this in Section 4.2.3. A definitive conclusion can only be drawn by future measurements of the specific surface area and pore size distribution within the FLG elecrodes by, for example, nitrogen absorption/desorption isotherms.

Shear Rate (RPM)	Scan Rate 5 mV s^{-1}	Scan Rate 10 mV s^{-1}	Scan Rate 20 mV s^{-1}	Scan Rate 25 mV s^{-1}	Scan Rate 50 mV s^{-1}
9000	–	–	8.33	–	7.18
7000	5.68	5.47	5.02	–	4.06
5000	4.75	4.16	–	3.80	3.37
3000	4.32	3.90	–	3.18	2.54

Table 4.3: Specific Capacitance in F g^{-1} of each electrode sample produced at various shear rates. Cyclic voltammagrams for low scan rates were not measured for the 9000 RPM sample.

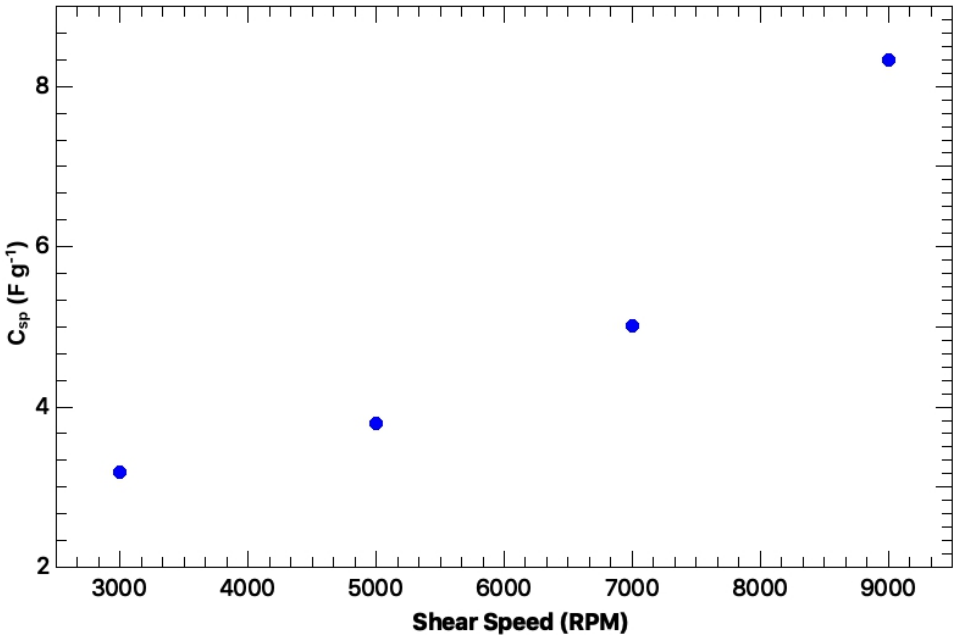

Figure 4.14: Variation of specific capacitance with the shear rate at which FLG electrodes were produced, measured at a sweep rate of 50 mV s^{-1}.

In addition to CV measurements, GCD was also carried out to enable a complimentary analysis. A typical charge/discharge curves is shown in Figure 4.15. GCD curves were measured at 1 mA for the 5000 and 9000 RPM samples 2.3 mA (or 0.1 A g^{-1}) for the 7000 RPM sample and 10 mA for the 3000 RPM sample. In all cases the number of half cycles was set to at least 1000. After the GCD curves had been produced, equations 4.3 and 4.4 were used to calculate the specific capacitance of each electrode sample:

$$C = \frac{Q}{\Delta V} \tag{4.3}$$

$$C_{specific} = \frac{4C}{M} \tag{4.4}$$

where C is total capacitance, Q is stored charge in Coulombs, ΔV is the potential window, identical to the one used in CV analysis and M is the total electrode mass. In order to determine $C_{specific}$ the value for $Q_{discharge}$ at the thousandth cycle was used for each calculation and the results are presented in Table 4.4. The variation in charge/discharge current and electrode masses prevents a quantitative comparison between the GCD data obtained from the various electrodes but the trends observed are in line with those seen in cyclic voltammetry.

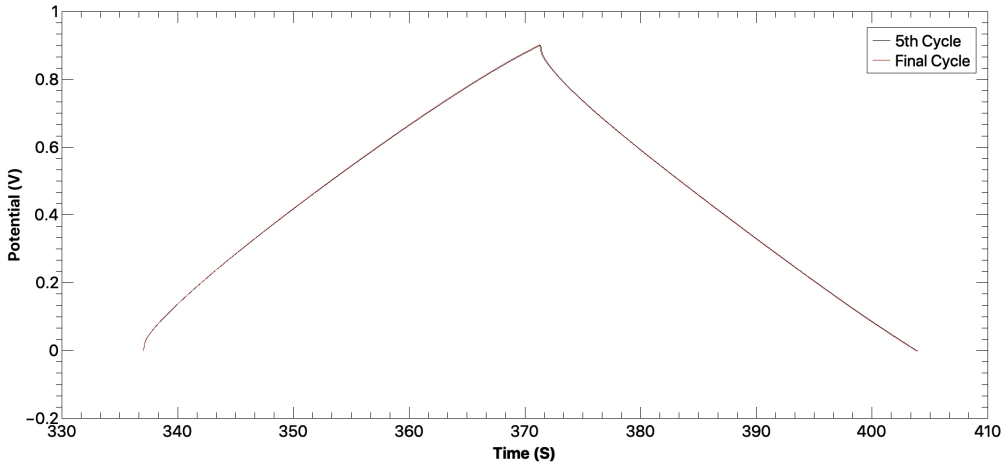

Figure 4.15: GCD curves (5th and final cycles) for a FLG electrode produced from material shear exfoliated at 5000 RPM.

Shear Rate (RPM)	Specific Capacitance (F g^{-1})
9000	9.18
7000	2.16
5000	3.51
3000	0.613

Table 4.4: Specific Capacitance calculated from GCD of each electrode sample produced at various shear rates.

All electrode samples had excellent cycling stability, as illustrated by Figure 4.16 which presents the variation in capacity of the 5000 RPM electrodes at a charge/discharge current of 1 mA (or 0.026 A g^{-1}) over 1200 cycles at which point there is a 99.9% retention of capacity. There is some fluctuation over the measurement, which may be the result of environmental conditions (such as laboratory temperature) over the measurement, with a minimum capacity of 96% observed on the 291st cycle.

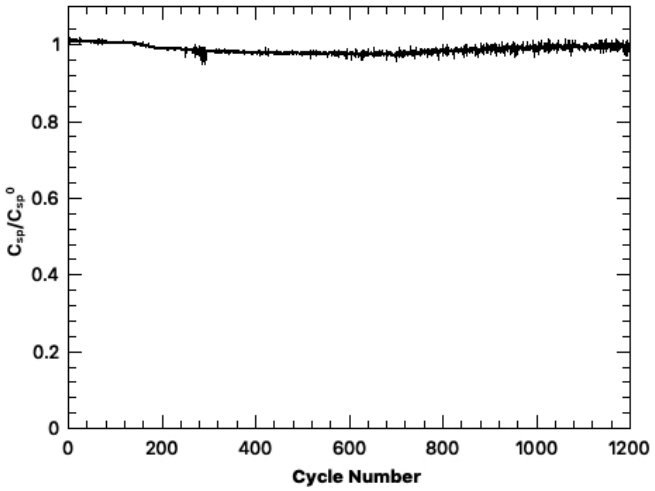

Figure 4.16: Variation of specific capacitance with cycle number measured on the discharge half cycle of FLG electrodes produced at 5000 RPM. The cell was subjected to charging/discharging at 1 mA. The data are normalised to the specific capacitance measured at the first cycle, C_{sp}^{0}.

Two other valuable characterisation parameters which can be extracted from the GCD data are the Coulombic efficiency of the cell (the ratio of the charge accumulated during the charging cycle to the charge released upon discharge) and the effective series resistance (ESR) of the cell. In an ideal EDLC the Coulombic efficiency should be 100% with no charge retained during the discharge half cycle. Coulombic efficiencies significantly below 100% are characteristic of irreversible redox processes within the sample and are associated energy which, after input, cannot be extracted from the cell. Coulombic efficiencies are presented in Table 4.5. In all samples there is an efficiency close to 100% indicating an absence of irreversible redox reactions and almost ideal EDLC behaviour, which is consistent with the close to rectangular cyclic voltammagrams presented above.

The ESR of each electrode, Table 4.5 was calculated from the GCD data on the 5th charge/discharge cycle by taking the voltage drop for a given cycle

and applying equation 4.5.

$$R = \frac{\Delta V}{I} \tag{4.5}$$

where ΔV is the voltage drop at a given cycle and I is the charge/discharge current.

Shear Rate (RPM)	Coloumbic Efficiency (%)	ESR (Ω)
9000	99	5.3
7000	99	15
5000	97	18
3000	98	34

Table 4.5: Coloumbic efficiency and ESR of electrode samples produced at various shear rates.

ESR is an important factor to consider as it directly impacts the (gravimetric) specific power density of a supercapacitor,

$$P = \frac{1}{4}\frac{V^2}{R} \tag{4.6}$$

where V is the voltage across the supercapacitor and R is the ESR. Hence, the lower the ESR the higher the power density.

The ESR of a supercapacitor originates from a combination of factors including: the contact resistance between the electrode layer and the current collector (absent in the case of the FLG electrodes produced in this work), the resistance between the constituent particles making up the electrode matrix, the resistance of the electrolyte and the resistance of the external leads (measured to be 0.6 Ω in the cell used in the experiments reported here). Given that the electrolyte and test fitting remain unchanged in the experiments reported here, the sole origin of the rather significant decrease in ESR between samples must reside in the electrodes themselves. Naively, it might be expected that the decrease in FLG platelet dimensions with increasing shear speed would lead to an *increase* in electrode resistance, due to the greater ratio of edge defect to pristine material and the creation of additional contacts between platelets in a given current path. However, the opposite behaviour is observed and can be explained by the increased carrier density associated

with the presence of edge defects. The increase in carrier density cannot only be expected to lead to an increase in the intrinsic quantum capacitance of the FLG platelets, as discussed in Section 1.6, but will also lead to improved electrode conductivity.

4.3 Conclusions

Aqueous surfactant stabilised suspensions of few layer graphene have been produced at several different shear speeds and it has been shown that these suspensions may be used to successfully produce free-standing, binder-free electrodes which may be used in EDLCs. Raman spectroscopy demonstrates that the defects in the FLG are primarily of edge type, associated with the boundaries of the platelets, and that they increase in concentration with increasing shear speed due to a reduction in platelet dimensions.

SEM characterisation of FLG 'paper' electrodes shows some morphological features which have not been previously reported in the literature, which have been tentatively ascribed to the formation of 'crystal like structures' by the surfactant under high shear/elevated temperature conditions from which the surfactant itself is removed when the electrodes are washed with high purity water.

Electrochemical characterisation shows that the FLG based electrode have a superficially low specific capacitance, with a maximum value of 8.33 F g^{-1} obtained from cyclic voltammetry at a sweep rate of 25 mV s^{-1} for samples produced at shear speeds of 9000 RPM. However, it should be borne in mind that many of the substantially higher values of specific capacitance reported in the literature only consider the mass of the active component and not the binder or current collector. When the electrode is considered as a whole, the values of specific capacitance reported for the FLG electrodes are not poor.

Finally, as the shear mixing speed in sample preparation increases so does the specific capacitance, coupled with a decrease in effective series resistance. It is tempting to ascribe this behaviour to the increased carrier density in the FLG platelets with decreasing size (so increasing the doping level within the material). However, a more detailed structural analysis, for example probing the variation of surface area and pore structure through nitrogen absorption/desorption experiments, is needed before a definitive conclusion can be drawn.

Chapter 5

Shear exfoliated few-layer MoS_2 platelets

5.1 Characterisation of few-layer MoS_2 platelets

5.1.1 Introduction

Graphene is not the only two-dimensional material which may have utility for electrodes in electrochemical energy storage devices such as supercapacitors. In Section 1.6 the use of MoS_2 for this application was also described. In this Chapter the characterisation of shear exfoliated few-layer MoS_2 is reported, as the first step towards future work involving the production of MoS_2-containing nanocomposite electrodes.

5.1.2 UV-Vis spectroscopy

Suspensions of MoS_2 were produced at eight different shear rates, as outlined in Section 3.1, and characterised through SEM and UV-Vis spectroscopy. UV-vis spectra from the suspensions are presented in Figure 5.1. The general forms of the spectra are the same for each suspension, consisting of two optical absorption peaks situated at around 670 nm and 610 nm and a rapidly rising absorption for wavelengths below about 500 nm. The two high wavelength peaks originate from excitonic absorption and are typically designated A and B for the longer and shorter wavelength peaks, respectively [174]. The location of these peaks is in good agreement with the literature [175–177]. The A exciton peak is associated with optical transitions between the highest

valence band and the conduction band at the K-points of the Brillouin zone and the B exciton peak is due to optical transitions between the spin-orbit split valence band and the conduction band. The lower wavelength absorption arises from direct intraband transitions producing free carriers. As with the shear exfoliated FLG suspensions, discussed in Section 4.2.1, the absorption spectrum can be used to determine the concentration of the few-layer MoS_2 in the suspension. Using the value for the MoS_2 absorption coefficient of 1.887 L $g^{-1}m^{-1}$, determined by Pagona and co-workers, the concentrations of the shear exfoliated solutions produced in this work were determined and are presented in Table 5.1. As can be deduced from the Table there is a general trend for increasing concentration with increasing shear speed, as might be expected, with a maximum concentration of 0.006 mg ml^{-1} obtained at a shear speed of 8000 RPM.

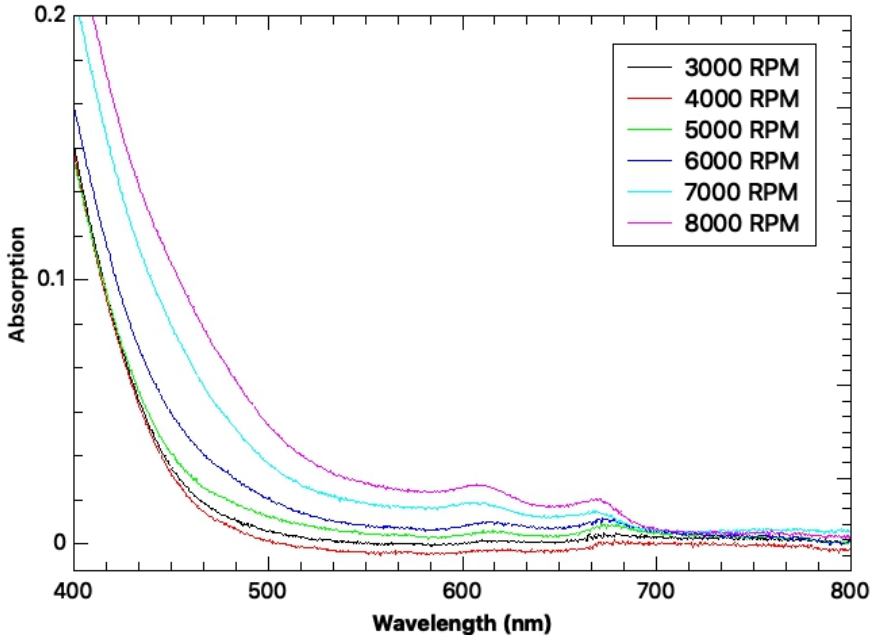

Figure 5.1: UV-Vis spectra of MoS_2 exfoliated at several shear speeds.

In addition to determining the concentration of the MoS_2 suspensions the UV-vis absorption spectra can be used to examine the thickness of the few-layer platelets produced. As outlined in Chapter 2, the band gap of MoS_2 changes with the number of layers in a sample, and the A and B exciton peaks are associated with optical transitions that take place just below the band gap. Thus, by measuring the position of the exciton peaks of the various suspensions, the change in the band gap can be calculated and hence the

Shear Speed (RPM)	Concentration (mg ml^{-1})
3000	0.0017
4000	0.0016
5000	0.002
6000	0.0027
7000	0.0046
8000	0.006

Table 5.1: Concentration of MoS_2 suspensions as a function of shear speed.

Shear Speed (RPM)	Exciton Peak A (nm)	Exciton Peak B (nm)
3000	673	612
4000	673	617
5000	673	617
6000	678	613.
7000	669	611
8000	666	606

Table 5.2: A and B exciton peaks of the various samples produced at different shear speeds.

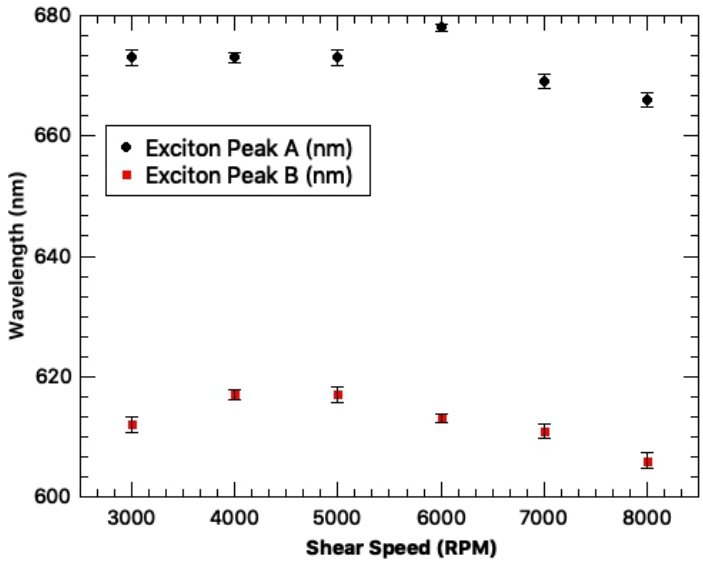

Figure 5.2: MoS_2 exciton peak wavelengths versus shear speed.

number of layers of that particular sample can be ascertained. The positions of the exciton peaks, determined from UV-vis data, are presented in Figure 5.2 and it can be seen that there is a general decrease of the wavelengths of both peaks for shear rates above 5000 RPM, although there is some scatter in the data larger than the measurement error. To evaluate the average number of layers in platelets within each sample, the energy of the exciton peaks was compared with the variation of peak position as a function of MoS_2 sample thickness in the literature [178]. The number of layers determined for each shear rate are as follows: for 3000 to 5000 RPM the number of layers was calculated to be 5 ± 1, for 6000 RPM the number of layers was 6 ± 1, for 7000 RPM the number of layers was 3 ± 1 and finally for 8000 RPM the number of layers was 2 ± 1. The decrease in MoS_2 platelet thickness as a function of shear speed indicates that suspensions of very thin material may be produced and it is worthwhile exploring higher shear speeds in future work to see whether the limit of predominantly single layer material may be achieved.

5.1.3 SEM

Although thickness is a critical metric for the evaluation of few-layer MoS_2 platelets produced by shear exfoliation, their size and overall morphology is also important to their application. In order to understand the influence of shear exfoliation on these latter parameters an automated approach to shape and area evaluation was developed, capable of analysing a large number of platelets and so coping with the variations in morphology produced through the random exfoliation events resulting from high shear mixing. Samples, created as outlined in Section 3.1, were vacuum filtered onto cellulose nitrate filter membranes using a very low concentration of material, leading to relatively isolated platelets rather than the continuous films required for the formation of FLG electrodes in Chapter 4. This approach allows individual platelets to be characterised through SEM. A large number of equally spaced images (typically 100 for each sample) were taken over a large area of the sample, using the automated scanning function of the SEM. The resulting micrographs were batch analysed using ImageJ to extract such characteristics as area, circularity and diameter. The use of ImageJ enabled automation of the analysis of the large number of images obtained.

A typical SEM image and the identification of few-layer MoS_2 platelets using ImageJ is shown in Figure 5.3. A binary image was created from the SEM micrographs, as this allowed the platelets to be differentiated from the filter membrane beneath. This approach ensured that the program only detects

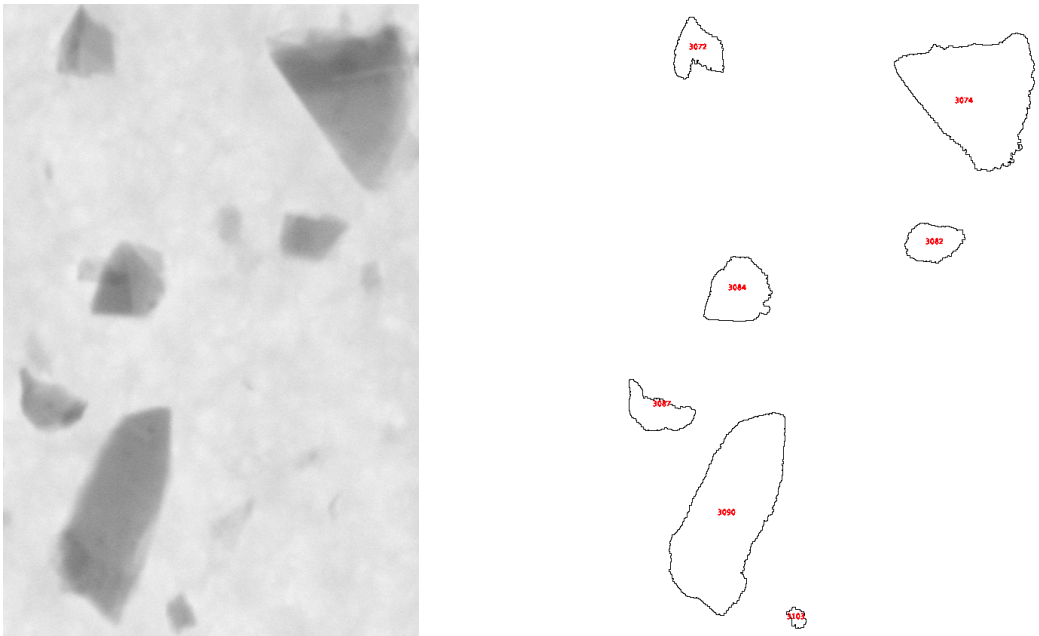

(a) Typical SEM Image of a shear exfoliated MoS_2 sample.

(b) Example from ImageJ showing platelet outlines.

Figure 5.3: An example of image analysis using ImageJ.

the platelets and not the structure of the underlying substrate and other small particles observed in the SEM, such as dust and foreign matter (it was not possible to undertake both sample preparation and imaging in a clean room environment). Once identified, the area, circularity and diameter of the platelets could be measured by creating a macro that applied the same set of parameters to multiple images acquired for the various shear rates. Figures 5.4-5.11 summarise the correlation between shear rates and platelet characteristics.

From 5.4, 5.5, 5.6 we can see that as shear rate increases the average area of the platelets initially decreases, with a greater distribution of platelets lying in the range 0-0.2 μm. It can also be seen that the number of larger platelets decreases rapidly. Note that for Figure 5.6 it would be inappropriate to use the width of the distribution as a measure of the estimated error since this variation is intrinsic rather than a result of random measurement error. In order to determine error bars it would be necessary to repeat sample production and measurement multiple times, which would require timescales beyond those available within this project.

Contrary to expectations [108], the average area of the platelets appears to

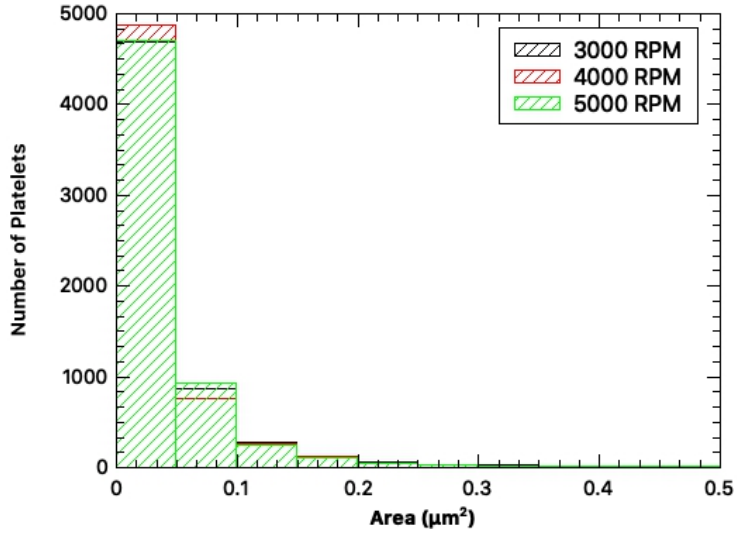

Figure 5.4: Distribution of platelet areas for few-layer MoS_2 samples shear exfoliated at 3000, 4000 and 5000 RPM.

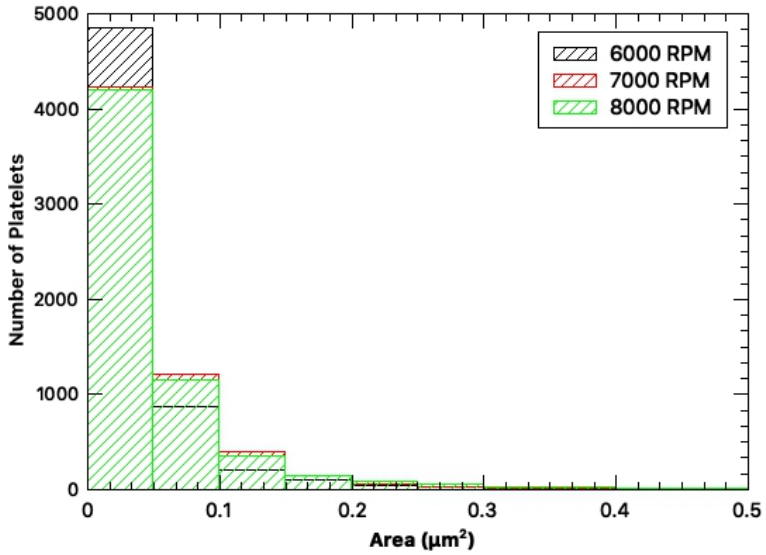

Figure 5.5: Distribution of platelet areas for few-layer MoS_2 samples shear exfoliated at 6000, 7000 and 8000 RPM.

increase at shear speeds of 7000 and 8000 RPM. It should be noted that a limitation of analysis using ImageJ is that it is not able to differentiate between individual platelets that have aggregated during the filtration process.

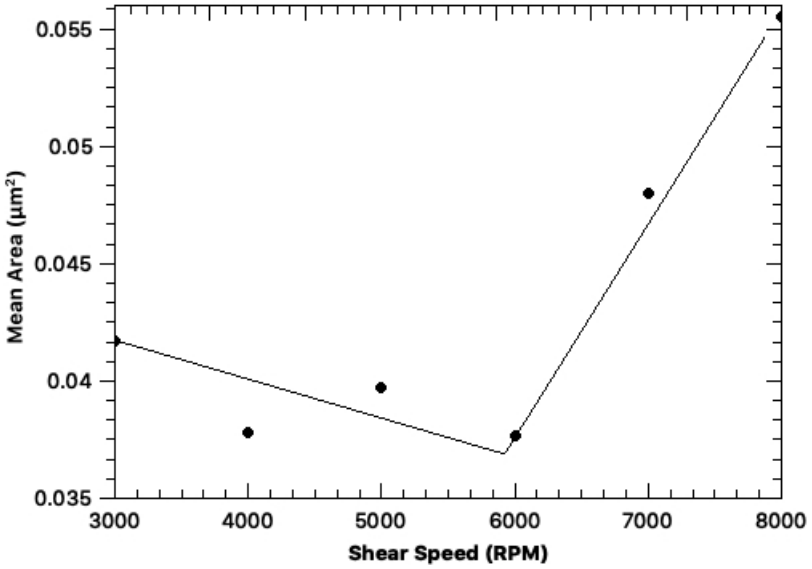

Figure 5.6: Average platelet areas for few-layer MoS_2 as a function of shear speed. The line is a guide to the eye.

Therefore, it registers these clusters of platelets as one enlarged platelet. This may explain the unexpected increase in apparently larger platelets apparent at higher shear speeds, where the concentration of the suspensions is larger. The observed behaviour requires further investigation in future work, for example by developing image analysis approaches capable of differentiating between individual platelets and aggregates or, more straightforwardly, by decreasing the density of the MoS_2 platelets on the filter membranes still further.

The general 'shape' of the few-layer MoS_2 platelets may be determined from their circularity, defined as

$$f_{circ} = \frac{4\pi A}{P^2} \tag{5.1}$$

where A is the area of the object and P is its perimeter. In the limit of a perfect circle $f_{circ} = 1$ and for a one-dimensional line $f_{circ} = 0$.

As the shear speed during the exfoliation process is increased, the circularity of the platelets is found to remain constant with minimal changes in its distribution, as shown in Figures 5.7, 5.8 and 5.9, although once more there is some scatter in the data. The average circularity of the platelets is around 0.2, indicating a high degree of anisotropy. The observed elongation of the exfoliated platelets can be readily explained by the nature of the exfoliation

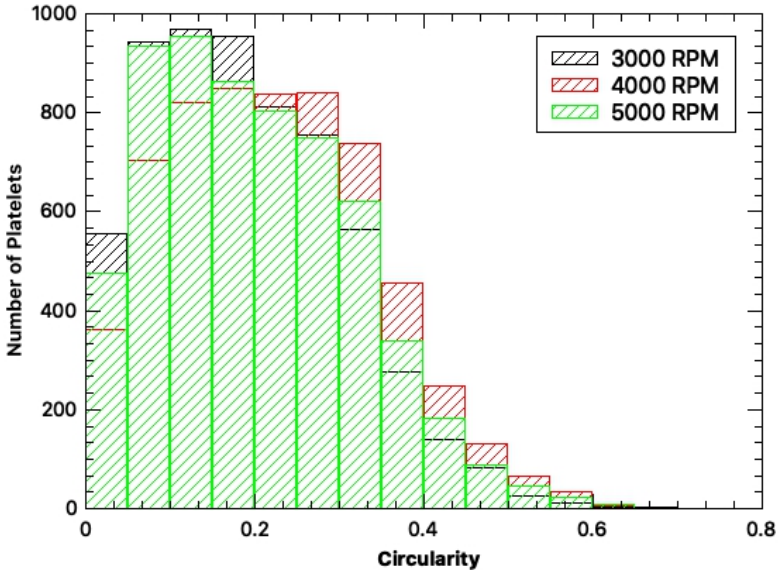

Figure 5.7: Circularity of MoS_2 platelets produced at shear speeds of 3000, 4000 and 5000 RPM.

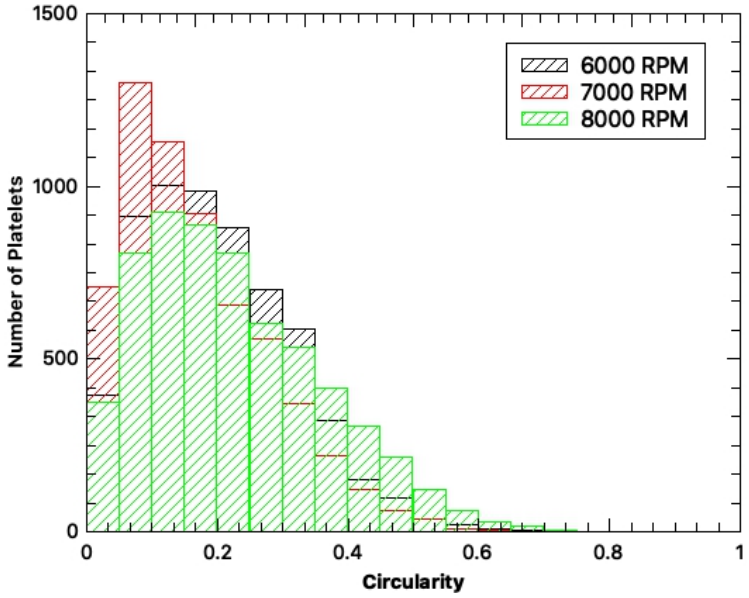

Figure 5.8: Circularity of MoS_2 platelets produced at shear speeds of 6000, 7000 and 8000 RPM.

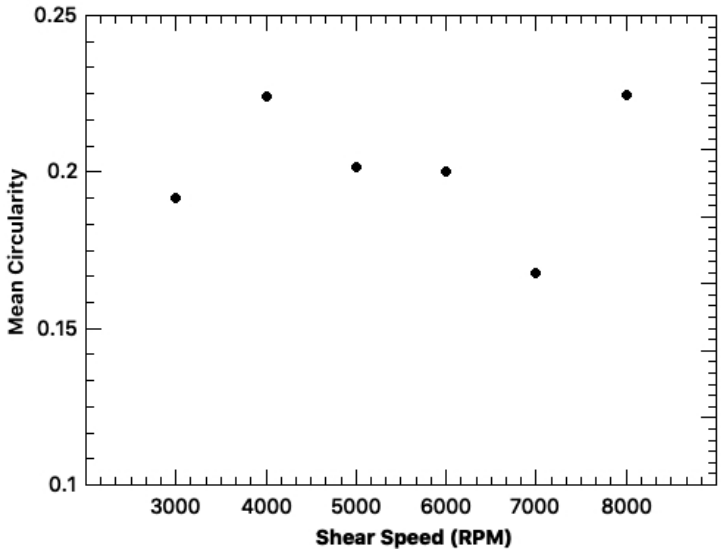

Figure 5.9: Average platelet circularity for few-layer MoS_2 as a function of shear speed.

process – the shear forces generated by the motion of the rotor with respect to the stator in the mixing head are highly directional and the resulting anisotropic strain within the MoS_2 particles will lead to a preferential fracture directions during the exfoliation process.

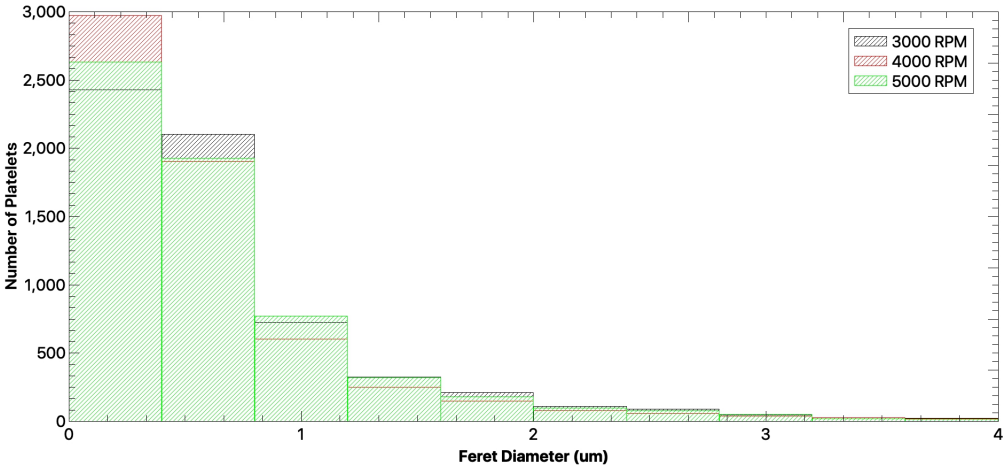

Figure 5.10: Feret diameter of MoS_2 platelets produced at Shear Rates 3000, 4000 and 5000 RPM.

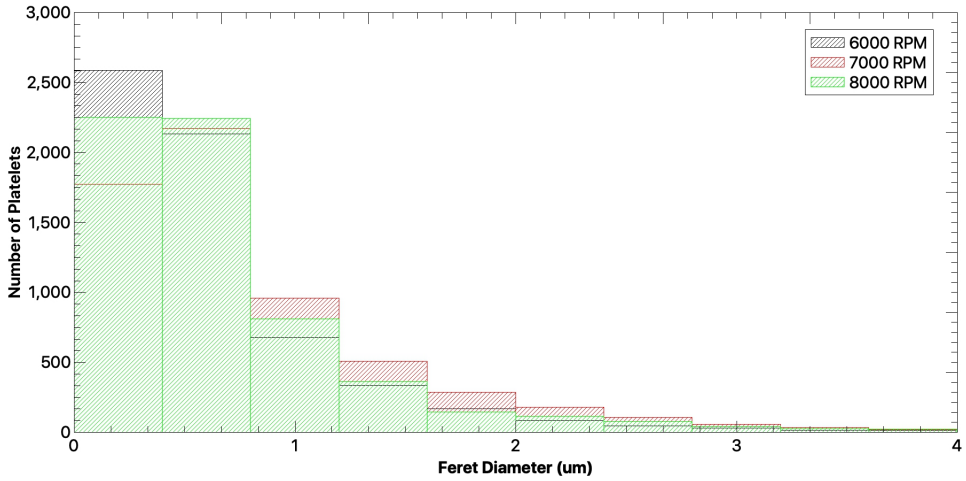

Figure 5.11: Feret diameter of MoS_2 platelets produced at Shear Rates 6000, 7000 and 8000 RPM.

The final characteristic that is of interest for this study is the diameter, particularly the Feret Diameter (also known as maximum caliper). It is defined, by ImageJ, as the maximum distance between any two points in the selection boundary along a specific direction. By analysing the variation of this characteristic with respect to shear rate, the length of platelets and hence their overall size can be further determined. From 5.10 and 5.11 it is observed that the diameter initially appears to decrease with an increase in shear speed, but once again increases at the highest shear speeds in agreement with the measurement of area discussed above.

5.2 Conclusions

An initial investigation into the influence of shear speed on the physical characteristics of surfactant-stabilised aqueous suspensions of few-layer MoS_2 has been undertaken. Morphology analysis was developed with a high degree of automation to enable the characterisation of a large number of platelets and so obtain a statistically valid description, while UV-vis based determination of thickness naturally sampled a large number of platelets.

It was found that increasing the shear speed, while keeping all other conditions (such as initial precursor concentrations, shear time etc.) fixed, led to a decrease in platelet thickness and area with no significant changes in circularity, although aggregation of platelets due to increased concentrations

at higher shear speeds complicate the measurements. A minimum average platelet thickness of 2 ± 1 layers could be achieved and mean circularities of around 0.2, indicating that a considerable degree of anisotropy still remains. The general trends observed indicate that further increases in shear speed may enable an average thickness of a single monolayer to be achieved, although this would be at the expense of a further decrease of platelet dimensions and, moreover, the anisotropic nature of the platelets would remain.

Chapter 6

Summary and Further work

6.1 Summary

This work has explored the use of shear exfoliation in the production of few-layer graphene (FLG) and few-layer MoS_2 and the use of the former to create free-standing, binder-free electrodes for use in supercapacitors. Surfactant stabilised aqueous suspensions of few-layer platelets of both materials have been successfully produced.

Continuous films of FLG platelets were produced by vacuum filtration and characterised by Raman spectroscopy, SEM and electrochemical analysis. As expected, increased shear speed led to a reduction in platelet size and an increase in boundary or edge defects, apparent in the evolution of the Raman spectra. SEM showed some evolution in the morphology in films fabricated from material produced with increasing shear speed. In particular, at low shear speeds a number of large, poorly exfoliated flakes could be observed and at high shear speeds the resultant films appears to be rougher. All films showed a number of voids, the morphology of which precluded fracture as their origin. Moreover, there is no evidence that they are associated with sample contamination. It is suggested that the high shear rates and increase in temperatures during the exfoliation process may lead to the formation of large micellar structures consisting of Triton X-100 the molecules of which are removed during electrode washing.

Free-standing, binder-free electrodes were successfully produced from the FLG films. Cyclic voltammetry and galvanostatic charge/discharge cycles demonstrated an increase in specific capacitance and decrease in effective series resistance in electrodes fabricated from FLG produced at increasing

shear speeds. This behaviour could be explained in terms of an increase in doping of the electrodes with an increasing concentration of edge defects in the FLG platelets. However, characterisation of the surface area and porosity of the samples is required to eliminate these factors. Although the highest reported values of specific capacitance are modest, the lack of binder or the need for a current collector should be taken into account in evaluating the utility of these electrodes.

In the case of graphene Raman spectroscopy was used in conjunction with metrics developed in the literature to characterise the shear exfoliated material. Such metrics cannot, however, be transferred from material to material and there may be questions regarding their robustness against differing production and measurement approaches. In order to address this issue the first steps towards a (semi-)automated process of platelet characterisation have been made. Low densities of MoS_2 platelets were vacuum filtered on to cellulose nitrate filter membranes and SEM micrographs obtained over a macroscopic area of the sample using automated sample positioning and focus. Batch techniques were developed using a readily available image analysis program, ImageJ, in order to rapidly evaluate the large number of micrographs produced for each sample. The principle of this approach was successfully demonstrated. Although issues were discovered with aggregation, it is expected that these would be relatively straightforward to address if appropriate time is available.

6.2 Further work

As discussed above, a key piece of further work would be to obtain a more complete microstructural description of the FLG electrodes beyond that which can be obtained by SEM and (indirect) metrics based on Raman spectroscopy. It is only with a full characterisation of surface area and pore structure that significant changes in these parameters or otherwise can be ascertained and the relative contribution of defects (and through them electronic doping) to the evolution of FLG electrode properties with preparation conditions properly understood.

The characterisation of platelets of few-layer two-dimensional solids is still underdeveloped, and is of key importance if these materials are to find widespread application. Further development of the approach employed for MoS_2 in this thesis is required. This could, for example, involve the development of more sophisticated image analysis approaches, taking into account contrast to estimate platelet thickness and eliminate aggregates.

The combination of two-dimensional materials into composite electrode materials is a highly attractive and logical step beyond the use of FLG alone. There are a number of routes which could be explored to combine TMDCs such as MoS_2 with graphene, including direct mixing and CVD growth of one material on the other. It is expected that there will be rich and unanticipated physical and chemical behaviour in such structures of direct relevance to electrochemical energy storage.

Bibliography

[1] O. Edenhofer, R. Pichs-Madruga, Y. Sokona, K. Seyboth, P. R. Matschoss, S. Kadner, T. Zwickel, P. Eickemeier, G. Hansen, S. Schlömer, C. V. Stechow, *Renewable Energy Sources and Climate Change Mitigation: Special Report of the Intergovernmental Panel on Climate Change.* Cambridge University Press, **2011**.

[2] P. A. Owusu, S. Asumadu-Sarkodie, *Cogent Engineering* **2016**, *3*, 1167990.

[3] A. Tomaszewska, Z. Chu, X. Feng, S. O'Kane, X. Liu, J. Chen, C. Ji, E. E. Endler, R. Li, L. Liu, L. Y, S. Zheng, S. Vetterlein, M. Gao, J. Du, M. A. Parkes, M. Ouyang, M. Marinescu, G. Offer, B. Wu, *eTransportation* **2019**, *1*, 100011.

[4] Z. M. Tehrani, D. J. Thomas, T. V. Korochkina, C. O. Phillips, D. Lupo, S. Lehtimäki, J. O'Mahony, D. T. Gethin, *Energy* **2017**, *118*, 1313–1321.

[5] B. Bolund, H. Bernhoff, M. Leijon, *Renewable and Sustainable Energy Reviews* **2007**, *11*, 235–258.

[6] R. E. Hebner, J. H. Beno, W. A. Walls, *IEEE Spectrum* **2002**, *39*, 46–51.

[7] D. W. Gao in Energy Storage for Sustainable Microgrid. Academic Press, **2015**, pp. 1–34.

[8] M. Siebert, B. Ebihara, R. Jansen, R. Fusaro, W. Morales, A. Kascak, A. Kenny in Proceedings of the Intersociety Energy Conversion Engineering Conference. *Vol. 1*, American Society of Mechanical Engineers, **2001**, pp. 125–132.

[9] P. P. Edwards, V. L. Kuznetsov, W. I. F. David, N. P. Brandon, *Energy Policy* **2008**, *36*, 4356–4362.

[10] S. Vazquez, S. M. Lukic, E. Galvan, L. G. Franquelo, J. M. Carrasco, *IEEE Transactions on Industrial Electronics* **2010**, *57*, 3881–3895.

[11] P. P. Kundu, K. Dutta in Compendium of Hydrogen Energy. *Vol. 4*, Woodhead Publishing, **2016**, pp. 111–131.

[12] R. M. Dell, P. T. Moseley, D. A. J. Rand in Towards Sustainable Road Transport. Academic Press, **2014**, pp. 260–295.
[13] I. Staffell, D. Scamman, A. V. Abad, P. Balcombe, P. E. Dodds, P. Ekins, N. Shah, K. R. Ward, *Energy and Environmental Science* **2019**, *12*, 463–491.
[14] W. Buckles, W. V. Hassenzahl, *IEEE Power Engineering Review* **2000**, *20*, 16–20.
[15] X. D. Xue, K. W. E. Cheng, D. Sutanto in Fourtieth IAS Annual Meeting. Conference Record of the 2005 Industry Applications Conference, 2005. *Vol. 2*, IEEE, **2005**, pp. 1524–1529.
[16] J. D. Boyes, N. H. Clark in 2000 Power Engineering Society Summer Meeting. *Vol. 3*, IEEE, **2000**, pp. 1548–1550.
[17] T. Ise, M. Kita, A. Taguchi, *IEEE Transactions on Applied Superconductivity* **2005**, *15*, 1915–1918.
[18] I. Kougias, S. Szabó, *Energy* **2017**, *140*, 318–329.
[19] C. Yang in Storing Energy. Elsevier, **2016**, pp. 25–38.
[20] S. Raos, Ž. Tomšić, I. Rajšl, *Journal of Energy* **2017**, *66*, 128–149.
[21] S. D. Garvey, A. Pimm in Storing Energy with Special Reference to Renewable Energy Sources. Elsevier, **2016**, pp. 87–111.
[22] P. Breeze in Power System Energy Storage Technologies. Academic Press, **2018**, pp. 23–31.
[23] E. A. Bouman, M. M. Øberg, E. G. Hertwich, *Energy* **2016**, *95*, 91–98.
[24] Z. Salameh in Renewable Energy System Design. Academic Press, **2014**, pp. 201–298.
[25] S. M. Whittingham in *Fundamentals of Materials for Energy and Environmental Sustainability.* Cambridge University Press, **2011**, 608–623.
[26] A. González, E. Goikolea, J. A. Barrena, R. Mysyk, *Renewable Sustainable Energy Reviews* **2016**, *58*, 1189–1206.
[27] M. A. Scibioh, B. Viswanathan in Materials for Supercapacitor Applications. Elsevier, **2020**, pp. 205–314.
[28] G. G. Prasad, N. Shetty, S. Thakur, R. Bommegowda, K. B. Bommegowda, *IOP Conference Series: Materials Science and Engineering* **2019**, *561*, 012105.
[29] M. Khalid, P. Bhardwaj, H. Varela in Science, Technology and Advanced Application of Supercapacitors. IntechOpen, **2019**, pp. 1–18.
[30] M. Elimelech, J. Gregory, X. Jia, R. A. Williams in Particle Deposition Aggregation Measurement, Modelling and Simulation. Elsevier, **1995**, pp. 9–32.

[31] A. Yu, V. Chabot, J. Zhang in Electrochemical Supercapacitors for Energy Storage and Delivery: Fundamentals and Applications. CRC Press, **2013**, pp. 37–53.
[32] C. D. Grahame, *Chemical Reviews* **1947**, *41*, 441–501.
[33] E. Redondo, E. Goikolea, R. Mysyk, *Electrochimica Acta* **2016**, *221*, 177–183.
[34] Z. S. Iro, C. Subramani, S. S. Dash, *International Journal of Electrochemical Science* **2016**, *11*, 10628–10643.
[35] P. R. Bandaru, H. Yamada, R. Narayanan, M. Hoefer, *Materials Science and Engineering: Reports* **2015**, *96*, 1–69.
[36] S. Srinivasan in Fuel Cells. Springer, **2006**, pp. 27–92.
[37] J. Bird in Electrical and Electronic Principles and Technology. Routledge, **2013**, pp. 62–79.
[38] S. Wen, J. Lee, I. Yeo, J. Park, S. Mho, *Electrochimica Acta* **2004**, *50*, 849–855.
[39] V. Augustyn, P. Simon, B. Dunn, *Energy & Environmental Science* **2014**, *7*, 1597–1614.
[40] A. Venkataraman, MA thesis, Portland State University, **2015**.
[41] A. D. Pasquier, I. Plitz, S. Menocal, G. Amatucci, *Journal of Power Sources* **2003**, *115*, 171–178.
[42] J. Libich, J. Máca, J. Vondrák, O. Čech, M. Sedlaříková, *Journal of Energy Storage* **2018**, *17*, 224–227.
[43] K. Khan, A. K. Tareen, M. Aslam, R. Wang, Y. Zhang, A. Mahmood, Z. Ouyang, H. Zhang, Z. Guo, *Journal of Materials Chemistry C* **2020**, *8*, 387–440.
[44] K. S. Novoselov, A. K. Geim, S. V. Morozov, D. Jiang, Y. Zhang, S. V. Dubonos, I. V. Grigorieva, A. A. Firsov, *Science* **2004**, *306*, 666–669.
[45] A. Gupta, T. Sakthivel, S. Seal, *Progress in Materials Science* **2015**, *73*, 44–126.
[46] D. Reddy, L. F. Register, G. D. Carpenter, S. K. Banerjee, *Journal of Physics D: Applied Physics* **2011**, *45*, 019501.
[47] X. Li, Y. Zhu, W. Cai, M. Borysiak, B. Han, D. Chen, R. D. Piner, L. Colombo, R. S. Ruoff, *Nano Letters* **2009**, *9*, 4359–4363.
[48] I. G. Crouch, *Defence Technology* **2019**, *15*, 241–253.
[49] D. G. Papageorgiou, I. A. Kinloch, R. J. Young, *Progress in Material Science* **2017**, *90*, 75–127.
[50] E. R. Mucciolo, C. H. Lewenkopf, *Journal of Physics: Condensed Matter* **2010**, *22*, 273201.
[51] G. Yang, L. Li, W. B. Lee, M. C. Ng, *Science and Technology of Advanced Materials* **2018**, *19*, 613–648.

[52] G. Mukhopadhyay, H. Behera, Emerging Two-Dimensional Materials: graphene and its other structural analogues. **2013**.
[53] M. Sullivan, MA thesis, University of Manchester, **2017**.
[54] L. Zhou, L. Fox, M. Włodek, L. Islas, A. Slastanova, E. Robles, O. Bikondoa, R. Harniman, N. Fox, M. Cattelan, W. H. Briscoe, *Carbon* **2018**, *136*, 255–261.
[55] Y. Cao, V. Fatemi, S. Fang, K. Watanabe, T. Taniguchi, E. Kaxiras, P. Jarillo-Herrero, *Nature* **2018**, *556*, 43–50.
[56] M. F. Craciun, S. Russo, M. Yamamoto, J. B. Oostinga, A. F. Morpurgo, S. Tarucha, *Nature Nanotechnology* **2009**, *4*, 383–388.
[57] A. A. Pirzado, G. Dalmas, L. Nguyen-Dinh, I. Komissarov, F. Le Normand, I. Janowska, *Current Medicinal Chemistry* **2016**, *3*, 139–144.
[58] T. Purkait, G. Singh, M. Singh, D. Kumar, R. S. Dey, *Scientific Reports* **2017**, *7*, 15239.
[59] M. Bhuyan, M. N. Uddin, M. M. Islam, F. A. Bipasha, S. S. Hossain, *International Nano Letters* **2016**, *6*, 65–83.
[60] Y. Wang, Y. Wu, Y. Huang, F. Zhang, X. Yang, Y. Ma, Y. Chen, *The Journal of Physical Chemistry C* **2011**, *115*, 23192–23197.
[61] K. S. Novoselov, D. Jiang, F. Schedin, T. J. Booth, V. V. Khotkevich, S. V. Morozov, A. K. Geim, *Proceedings of the National Academy of Sciences of the United States of America* **2005**, *102*, 10451–10453.
[62] H. Sadeghi, S. M. Mousavi, M. Rahmani, M. T. Ahmadi, R. Ismail in Advanced Nanoelectronics. CRC Press, **2018**, pp. 187–204.
[63] X. Chia, A. Y. S. Eng, A. Ambrosi, S. M. Tan, M. Pumera, *Chemical Reviews* **2015**, *115*, 11941–11966.
[64] X. Li, H. Zhu, *Journal of Materiomics* **2015**, *1*, 33–44.
[65] J. Sun, X. Li, W. Guo, M. Zhao, X. Fan, Y. Dong, C. Xu, J. Deng, Y. Fu, *Crystals* **2017**, *7*, 198.
[66] F. Ghasemi, M. Jalali, A. Abdollahi, S. Mohammadi, Z. Sanaee, S. Mohajerzadeh, *RSC Advances* **2017**, *7*, 52772–52781.
[67] U. Krishnan, M. Kaur, K. Singh, M. Kumar, A. Kumar, *Superlattices and Microstructures* **2019**, *128*, 274–297.
[68] X. Zhang, N. Biekert, S. Choi, C. H. Naylor, C. De-Eknamkul, W. Huang, X. Zhang, X. Zheng, D. Wang, A. T. C. Johnson, E. Cubukcu, *Nano Letters* **2018**, *18*, 957–963.
[69] D. Voiry, M. Salehi, R. Silva, T. Fujita, M. Chen, T. Asefa, V. B. Shenoy, G. Eda, M. Chhowalla, *Nano Letters* **2013**, *13*, 6222–6227.
[70] C. Feng, J. Ma, H. Li, R. Zeng, Z. Guo, H. Liu, *Materials Research Bulletin* **2009**, *44*, 1811–1815.

[71] L. Liu, J. Wu, L. Wu, M. Ye, X. Liu, Q. Wang, S. Hou, P. Lu, L. Sun, J. Zheng, L. Xing, L. Gu, X. Jiang, L. Xie, L. Jiao, *Nature Materials* **2018**, *17*, 1108–1114.
[72] J. T. Ye, Y. J. Zhang, R. Akashi, M. S. Bahramy, R. Arita, Y. Iwasa, *Science* **2012**, *338*, 1193–1196.
[73] D. Lembke, S. Bertolazzi, A. Kis, *Accounts of Chemical Research* **2015**, *48*, 100–110.
[74] Y. Gao, K. Huang, X. Wu, Z. Hou, Y. Liu, *Journal of Alloys and Compounds* **2018**, *741*, 174–181.
[75] P. Pazhamalai, K. Krishnamoorthy, S. Manoharan, S. Kim, *Journal of Alloys and Compounds* **2019**, *771*, 803–809.
[76] X. Zhang, L. Hou, A. Ciesielski, P. Samorì, *Advanced Energy Materials* **2016**, *6*, 1600671.
[77] K. M. McCreary, A. T. Hanbicki, J. T. Robinson, E. Cobas, J. C. Culbertson, A. L. Friedman, G. G. Jernigan, B. T. Jonker, *Advanced Functional Materials* **2014**, *24*, 6449–6454.
[78] R. Raccichini, *Nature Materials* **2015**, *14*, 271–279.
[79] R. S. Sharbidre, S. M. Park, C. J. Lee, B. C. Park, S. Hong, S. Bramhe, G. Y. Yun, J. Ryu, T. N. Kim, *Korean Journal of Materials Research* **2017**, *27*, 705–709.
[80] D. Pandey, R. Reifenberger, R. Piner, *Surface Science* **2008**, *602*, 1607–1613.
[81] S. Pei, H.-M. Cheng, *Carbon* **2012**, *50*, 3210–3228.
[82] X. Chen, L. Zhang, S. Chen, *Synthetic Metals* **2015**, *210*, 95–108.
[83] G. Lim, K. D. Kihm, H. G. Kim, W. Lee, W. Lee, K. R. Pyun, S. Cheon, P. Lee, J. Y. Min, S. H. Ko, *Nanomaterials* **2018**, *8*, 557.
[84] R. Messier, S. Trolier-McKinstry in Encyclopedia of Materials: Science and Technology. Elsevier, **2001**, pp. 9306–9313.
[85] H. Kim, E. Saiz, M. Chhowalla, C. Mattevi, *New Journal of Physics* **2013**, *15*, 053012.
[86] X. Li, W. Cai, L. Colombo, R. S. Ruoff, *Nano Letters* **2009**, *9*, 4268–4272.
[87] H. Şar, A. Özden, B. Yorulmaz, C. Sevik, N. K. Perkgoz, F. Ay, *Journal of Materials Science: Materials in Electronics* **2018**, *29*, 8785–8792.
[88] G. Ruan, Z. Sun, Z. Peng, J. M. Tour, *ACS Nano* **2011**, *5*, 7601–7607.
[89] J.-O. Carlsson, P. M. Martin in Handbook of Deposition Technologies for Films and Coatings. Elsevier, **2010**, pp. 314–363.
[90] J. Yu, J. Li, W. Zhang, H. Chang, *Chemical Science* **2015**, *6*, 6705–6716.

[91] K. S. Kim, Y. Zhao, H. Jang, S. Y. Lee, J. M. Kim, K. S. Kim, J. Ahn, P. Kim, J. Choi, B. Hong, *Nature* **2009**, *457*, 706–710.

[92] Z. Sun, Z. Yan, J. Yao, E. Beitler, Y. Zhu, J. M. Tour, *Nature* **2010**, *468*, 549–552.

[93] Z. Cai, Q. Yao, X. Chen, X. Wang in Novel Nanomaterials for Biomedical, Environmental and Energy Applications. Elsevier, **2019**, pp. 435–464.

[94] J. Cai, P. Ruffieux, R. Jaafar, M. Bieri, T. Braun, S. Blankenburg, M. Muoth, A. P. Seitsonen, M. Saleh, X. Feng, K. Müllen, R. Fasel, *Nature* **2010**, *466*, 470–473.

[95] J. M. Tour, *Chemistry of Materials* **2013**, *26*, 163–171.

[96] V. Nicolosi, M. Chhowalla, M. G. Kanatzidis, M. S. Strano, J. N. Coleman, *Science* **2013**, *340*.

[97] J. Wang, K. K. Manga, Q. Bao, K. P. Loh, *Journal of the American Chemical Society* **2011**, *133*, 8888–8891.

[98] P. Yu, S. E. Lowe, G. P. Simon, Y. L. Zhong, *Current Opinion in Colloid & Interface Science* **2015**, *20*, 329–338.

[99] N. Liu, P. Kim, J. H. Kim, J. H. Ye, S. Kim, C. J. Lee, *ACS Nano* **2014**, *8*, 6902–6910.

[100] C. Shih, A. Vijayaraghavan, R. Krishnan, R. Sharma, J. Han, M. Ham, Z. Jin, S. Lin, G. L. C. Paulus, N. F. Reuel, Q. H. Wang, D. Blankschtein, M. S. Strano, *Nature Nanotechnology* **2011**, *6*, 439–445.

[101] T. C. Achee, W. Sun, J. T. Hope, S. G. Quitzau, C. B. Sweeney, S. A. Shah, T. Habib, M. J. Green, *Scientific Reports* **2018**, *8*, 14525.

[102] F. Liu, C. Wang, M. A. Sui, X. Riaz, M. Xu, L. Wei, Y. Chen, *Carbon Energy* **2019**, *1*, 173–199.

[103] S. E. Lowe, G. Shi, Y. Zhang, J. Qin, L. Jiang, S. Jiang, M. Al-Mamun, P. Liu, Y. L. Zhong, H. Zhao, *Nano Materials Science* **2019**, *1*, 215–223.

[104] J. Kim, S. Kwon, D. Cho, B. Kang, H. Kwon, Y. Kim, S. O. Park, G. Y. Jung, E. Shin, H. Kim, W. ad Lee, G. H. Ryu, M. Choi, T. H. Kim, J. Oh, S. Park, S. K. Kwak, S. W. Yoon, D. Byun, Z. Lee, C. Lee, *Nature Communications* **2015**, *6*, 8294.

[105] P. Turner, M. Hodnett, R. Dorey, J. D. Carey, *Scientific Reports* **2019**, *9*, 8710.

[106] J. N. Coleman, M. Lotya, A. O'Neill, S. D. Bergin, P. J. King, U. Khan, K. Young, A. Gaucher, S. De, R. J. Smith, I. V. Shvets, S. K. Arora, G. Stanton, H. Kim, K. Lee, G. T. Kim, G. S. Duesberg, T. Hallam, J. J. Boland, J. J. Wang, J. F. Donegan, J. C. Grunlan, G. Moriarty, A. Shmeliov, R. J. Nicholls, J. M. Perkins, E. M. Grieveson,

K. Theuwissen, D. W. McComb, P. D. Nellist, V. Nicolosi, *Science* **2011**.

[107] A. Ciesielski, S. P., *Chemical Society Reviews* **2014**, *43*, 381–398.

[108] K. R. Paton, E. Varrla, C. Backes, R. J. Smith, U. Khan, A. O'Neill, C. Boland, M. Lotya, O. M. Istrate, P. King, T. Higgins, S. Barwich, P. May, P. Puczkarski, I. Ahmed, M Mobius, H. Pettersson, E. Long, J. Coelho, S. E. O'Brien, E. K. McGuire, B. M. Sánchez, G. S. Duesberg, N. McEvoy, T. J. Pennycook, C. Downing, A. Crossley, V. Nicolosi, J. N. Coleman, *Nature Materials* **2014**, *13*, 624–630.

[109] S. Biccai, S. Barwich, D. Boland, A. Harvey, D. Hanlon, N. McEvoy, J. N. Coleman, *2D Materials* **2018**, *6*, 015008.

[110] H. Gao, G. Hu, *RSC Advances* **2016**, *6*, 10132–10143.

[111] U. Khan, A. O'Neill, H. Porwal, P. May, K. Nawaz, J. N. Coleman, *Carbon* **2012**, *50*, 470–475.

[112] R. Durge, R. V. Kshirsagar, P. Tambe, *Procedia Engineering* **2014**, *97*, 1457–1465.

[113] Y. Xu, H. Cao, Y. Xue, B. Li, W. Cai, *Nanomaterials* **2018**, *8*, 942.

[114] M. V. Bracamonte, G. I. Lacconi, S. Urreta, L. E. F. Foa Torres, *The Journal of Physical Chemistry C* **2014**, *118*, 15455–15459.

[115] V. Forsberg, R. Zhang, J. Bäckström, C. Dahlström, B. Andres, M. Norgren, M. Andersson, M. Hummelgård, H. Olin, *Plos One* **2016**, *11*, 1–12.

[116] M. D. Stoller, S. Park, Y. Zhu, J. An, R. Ruoff, *Nano Letters* **2008**, *8*, 3498–3502.

[117] M. D. Stoller, Thesis, **2011**.

[118] Y. Dong, Z. Wu, W. Ren, H. Cheng, X. Bao, *Science Bulletin* **2017**, *62*, 724–740.

[119] M. D. Stoller, C. W. Magnuson, Y. Zhu, S. Murali, J. W. Suk, R. Piner, R. S. Ruoff, *Energy & Environmental Science* **2011**, *4*, 4685–4689.

[120] Y. Si, E. T. Samulski, *Chemistry of Materials* **2008**, *20*, 6792–6797.

[121] X. Yang, J. Zhu, L. Qiu, D. Li, *Advanced Materials* **2011**, *23*, 2833–2838.

[122] S. Biswas, L. T. Drzal, *ACS Applied Materials Interfaces* **2010**, *2*, 2293–300.

[123] T. B. S. Institution, *PD ISO/TS 80004-13:2017*.

[124] J. Xia, F. Chen, J. Li, N. Tao, *Nature Nanotechnology* **2009**, *4*, 505–9.

[125] M. A. Pope, I. A. Aksay, *The Journal of Physical Chemistry C* **2015**, *119*, 20369–20378.

[126] J. Chen, W. R. Walker, L. Xu, O. Krysiak, Z. She, M. A. Pope, *ACS Nano* **2020**, *14*, 5636–5648.

[127] M. Acerce, D. Voiry, M. Chhowalla, *Nature Nanotechnology* **2015**, *10*, 313–318.
[128] K. Huang, L. Wang, Y.-J. Liu, Y. Liu, H.-B. Wang, T. Gan, L.-L. Wang, *International Journal of Hydrogen Energy* **2013**, *38*, 14027–14034.
[129] P. J. Worsfold, E. A. G. Zagatto in Encyclopedia of Analytical Science. Elsevier, **2019**, pp. 244–248.
[130] T. Sau, Molecular absorption spectroscopy lab. **Accessed 1/02/20**.
[131] R. Saito, Y. Tatsumi, S. Huang, X. Ling, M. S. Dresselhaus, *Journal of Physics: Condensed Matter* **2016**, *28*, 353002.
[132] T. Owen in Fundamentals of Modern UV-visible Spectroscopy: Primer. Agilent Technologies, **2000**, pp. 2–28.
[133] S. Uran, A. Alhani, C. Silva, *AIP Advances* **2017**, *7*, 035323.
[134] C. Backes, K. R. Paton, D. Hanlon, S. Yuan, M. I. Katsnelson, J. Houston, R. J. Smith, D. McCloskey, J. F. Donegan, J. N. Coleman, *Nanoscale* **2016**, *8*, 4311–4323.
[135] R. R. Jones, D. C. Hooper, L. Zhang, D. Wolverson, V. K. Valev, *Nanoscale Research Letters* **2019**, *14*, 231.
[136] S. Huang, PhD thesis, **2017**.
[137] Z. Dong, H. Xu, F. Liang, C. Luo, C. Wang, Z. Cao, X. Chen, J. Zhang, X. Wu, *Molecules* **2019**, *24*, 88.
[138] X. Cong, X. Liu, M. Lin, P. Tan, *NPJ 2D Materials and Applications* **2020**, *4*, 13.
[139] S. Zhang, N. Zhang, Y. Zhao, T. Cheng, X. Li, R. Feng, H. Xu, Z. Liu, J. Zhang, L. Tong, *Chemical Society Reviews* **2018**, *47*, 3217–3240.
[140] F. Liang, H. Xu, X. Wu, C. Wang, C. Luo, J. Zhang, *Chinese Physics B* **2018**, *27*, 037802.
[141] J. Lee, M. Kim, H. Cheong, *Applied Microscopy* **2015**, *45*, 126–130.
[142] G. Odahara, T. Ishikawa, K. Fukase, S. Otani, O. Chuhei, M. Suzuki, T. Yasue, T. Koshikawa in Graphene - Synthesis, Characterization, Properties and Applications. IntechOpen, **2011**, pp. 1–20.
[143] R. Lewandowska in Encyclopedia of Materials: Science and Technology. Elsevier, **2010**, pp. 1–6.
[144] K. Akhtar, S. A. Khan, S. B. Khan, A. M. Asiri in Handbook of Materials Characterization. Springer, **2018**, pp. 113–145.
[145] E. Pickering, The Scanning Electron Microscope. Available at https://www.eng-atoms.msm.cam.ac.uk/RoyalSocDemos, **2015**.
[146] J. Seyforth, Scanning electron microscopy (SEM): an introduction to the use of SEM for characterising the surface topology and composition of matter with further applications. **2015**.
[147] L. Liang, V. Meunier, *Nanoscale* **2014**, *6*, 5394–5401.

[148] B. Cheney, *Materials Engineering Department San Jose State University* **2007**.
[149] M. J. Baker, C. S. Hughes, K. A. Hollywood in Biophotonics: Vibrational Spectroscopic Diagnostics. Morgan & Claypool, **2016**, pp. 14–27.
[150] D. M. Stoller, S. R. Ruoff, *Energy & Environmental Science* **2010**, *3*, 1294–1301.
[151] E. J. X. Pang, S. J. Pickering, A. Chan, K. H. Wong, P. L. Lau, *Journal of Solid State Chemistry* **2012**, *193*, 147–153.
[152] K. Tsay, L. Zhang, J. Zhang, *Electrochimica Acta* **2012**, *60*, 428–436.
[153] V. Khomenko, E. Frackowiak, F. Béguin, *Electrochimica Acta* **2005**, *50*, 2499–2506.
[154] Y. Li, X. Li, *RSC Advances* **2013**, *3*, 2398–2403.
[155] R. Farma, M. Deraman, A. Awitdrus, I. A. Talib, R. Omar, J. G. Manjunatha, M. Ishak, N. Basri, B. N. M. Dolah, *International Journal of Electrochemical Science* **2013**, *8*, 257–273.
[156] F. Licht, M. A. Davis, H. A. Andreas, *Journal of Power Sources* **2020**, *446*, 227354.
[157] B. Broady, MA thesis, Durham University, **2019**.
[158] A. Talmantaite, MA thesis, Durham University, **2018**.
[159] T. Dobbelaere, P. M. Vereecken, C. Detavernier, *HardwareX* **2017**, *2*.
[160] D. Li, M. B. Muller, S. Gilje, R. B. Kaner, G. G. Wallace, *Nat Nanotechnol* **2008**, *3*, 101–5.
[161] Z. Ismail, K. Yusoh, *AIP Conference Proceedings* **2016**, *1756*, 070002.
[162] U. Khan, A. O'Neill, M. Lotya, S. De, J. N. Coleman, *Small* **2010**, *6*, 864–871.
[163] M. Lotya, Y. Hernandez, P. J. King, R. J. Smith, V. Nicolosi, L. S. Karlsson, F. M. Blighe, S. De, Z. Wang, I. T. McGovern, G. S. Duesberg, J. N. Coleman, *Journal of the American Chemical Society* **2009**, *131*, 3611–3620.
[164] A. Das, B. Chakraborty, A. K. Sood, *Bulletin of Materials Science* **2007**, *31*, 579–584.
[165] Y. Hao, Y. Wang, L. Wang, Z. Ni, Z. Wang, R. Wang, C. K. Koo, Z. Shen, J. T. L. Thong, *Small* **2010**, *6*, 195–200.
[166] A. C. Ferrari, J. C. Meyer, V. Scardaci, C. Casiraghi, M. Lazzeri, F. Mauri, S. Piscanec, D. Jiang, K. S. Novoselov, S. Roth, A. K. Geim, *Physical Review Letters* **2006**, *97*, 187401.
[167] C. Casiraghi, *Physica Status Solidi (b)* **2011**, *248*, 2593–2597.
[168] C. Casiraghi, S. Pisana, K. S. Novoselov, A. K. Geim, A. C. Ferrari, *Applied Physics Letters* **2007**, *91*, 233108.

[169] C. Casiraghi, *Physical Review B* **2009**, *80*, DOI 10.1103/PhysRevB.80.233407.

[170] E. H. Martins Ferreira, M. V. O. Moutinho, F. Stavale, M. M. Lucchese, R. B. Capaz, C. A. Achete, A. Jorio, *Physical Review B* **2010**, *82*, 125429.

[171] A. Eckmann, A. Felten, A. Mishchenko, L. Britnell, R. Krupke, K. S. Novoselov, C. Casiraghi, *Nano Letters* **2012**, *12*, 3925–30.

[172] N. Stubicar, J. Matejas, P. Zipper, R. Wilfing in *Surfactants in Solution*, (Ed.: K. Mittal), Springer, Boston, USA, **1989**, pp. 181–195.

[173] J. J. Cardiel, H. Furusho, U. Skoglund, A. Q. Shen, *Sci Rep* **2015**, *5*, 17941.

[174] R. Kumar, N. Goel, R. Raliya, P. Biswas, M. Kumar, *Nanotechnology* **2018**, *29*, 404001.

[175] C. Yim, M. O'Brien, N. McEvoy, S. Winters, I. Mirza, J. G. Lunney, G. S. Duesberg, *Applied Physics Letters* **2014**, *104*, 103114.

[176] X. Li, Y. Shi, S. Li, W. Shi, W. Han, C. Zhou, X. Zhao, B. Liang, *Optical Materials Express* **2018**, *8*, 3082–3091.

[177] A. Castellanos-Gomez, J. Quereda, H. P. Van Der Meulen, N. Agraït, G. Rubio-Bollinger, *Nanotechnology* **2016**, *27*, 115705.

[178] Y. Niu, S. Gonzalez-Abad, R. Frisenda, P. Marauhn, M. Drüppel, P. Gant, R. Schmidt, N. S. Taghavi, D. Barcons, A. J. Molina-Mendoza, S. M. de Vasconcellos, R. Bratschitsch, D. Pérez De Lara, M. Rohlfing, A. Castellanos-Gomez, *Nanomaterials* **2018**, *8*, 725.